In-situ measurement and monitoring methods for metal powder bed fusion – an updated review

Marco Luigi Giuseppe Grasso, Afaf Remani, Andrew Dickins, B M Colosimo and Richard K Leach

This is a post-peer-review, pre-copyedit version of an article published in Measurement Science and Technology. The final authenticated version is available online at: http://dx.doi.org/10.1088/1361-6501/ac0b6b

Measurement Science and Technology

ACCEPTED MANUSCRIPT

In-situ measurement and monitoring methods for metal powder bed fusion – an updated review

To cite this article before publication: Marco Luigi Giuseppe Grasso *et al* 2021 *Meas. Sci. Technol.* in press https://doi.org/10.1088/1361-6501/ac0b6b

Manuscript version: Accepted Manuscript

Accepted Manuscript is “the version of the article accepted for publication including all changes made as a result of the peer review process, and which may also include the addition to the article by IOP Publishing of a header, an article ID, a cover sheet and/or an ‘Accepted Manuscript’ watermark, but excluding any other editing, typesetting or other changes made by IOP Publishing and/or its licensors”

This Accepted Manuscript is **© 2021 IOP Publishing Ltd**.

During the embargo period (the 12 month period from the publication of the Version of Record of this article), the Accepted Manuscript is fully protected by copyright and cannot be reused or reposted elsewhere.
As the Version of Record of this article is going to be / has been published on a subscription basis, this Accepted Manuscript is available for reuse under a CC BY-NC-ND 3.0 licence after the 12 month embargo period.

After the embargo period, everyone is permitted to use copy and redistribute this article for non-commercial purposes only, provided that they adhere to all the terms of the licence https://creativecommons.org/licences/by-nc-nd/3.0

Although reasonable endeavours have been taken to obtain all necessary permissions from third parties to include their copyrighted content within this article, their full citation and copyright line may not be present in this Accepted Manuscript version. Before using any content from this article, please refer to the Version of Record on IOPscience once published for full citation and copyright details, as permissions will likely be required. All third party content is fully copyright protected, unless specifically stated otherwise in the figure caption in the Version of Record.

View the article online for updates and enhancements.

This content was downloaded from IP address 131.175.12.9 on 25/06/2021 at 09:04

In-situ measurement and monitoring methods for metal powder bed fusion – an updated review

M. Grasso[1*], A. Remani[2], A. Dickins[2], B.M. Colosimo[1], R. K. Leach[2]

[1]Politecnico di Milano, Department of Mechanical Engineering, Via La Masa 1, 20154 Milan, Italy
[2]University of Nottingham, Faculty of Engineering, Nottingham, NG8 1BB, UK
*Corresponding author: marcoluigi.grasso@polimi.it

Abstract. The possibility of using a variety of sensor signals acquired during metal powder bed fusion processes, to support part and process qualification and for the early detection of anomalies and defects, has been continuously attracting an increasing interest. The number of research studies in this field has been characterised by significant growth in the last few years, with several advances and new solutions compared with first seminal works. Moreover, industrial powder bed fusion systems are increasingly equipped with sensors and toolkits for data collection, visualisation and, in some cases, embedded in-process analysis. Many new methods have been proposed and defect detection capabilities have been demonstrated. Nevertheless, several challenges and open issues still need to be tackled to bridge the gap between methods proposed in the literature and actual industrial implementation. This paper presents an updated review of the literature on in-situ sensing, measurement and monitoring for metal powder bed fusion processes, with a classification of methods and a comparison of enabled performances. The study summarises the types and sizes of defects that are practically detectable while the part is being produced and the research areas where additional technological advances are currently needed.

Keywords: in-situ; in-process; sensing; metrology; monitoring; powder bed fusion; additive manufacturing; defects.

1 Introduction

Since early adoptions of metal additive manufacturing (AM) technologies, the opportunity of exploiting the layerwise production paradigm to monitor the process and detect flaws at their onset stage, and possibly implement closed-loop control strategies, has attracted the interest of the research and industrial communities. The seminal studies of Tapia and Elwany (2014) and Mani et al. (2015) clearly pointed out the measurement needs to take advantage of the large amount of in-process information made available equipping AM systems with various kinds of sensors. Other authors reviewed the literature devoted to in-situ sensing and monitoring methods (Spears and Gold, 2016, Everton et al., 2016, Grasso and Colosimo, 2017), summarising and comparing various possible solutions to make sense of large amounts of data measured layer by layer. In the last few years, the number of studies has been characterised by an impressive growth as shown in Fig. 1 (details about the procedure adopted in this study for the literature collection are given in the Appendix). By limiting the field of analysis to powder bed fusion (PBF) processes only, the number of papers published since 2018 is more than twice the overall number published before 2018. Moreover, various commercial tools have been made available by almost all PBF system developers and several novel patents related to in-situ sensing, measurement and monitoring techniques have been released in the last few years. Some methodologies previously explored in seminal papers have been consolidated and validated in most recent works, and a relevant number of new approaches has been presented in the last couple of years, paving the way for new research directions and new industrialisation opportunities. First studies mainly focused on the feasibility analysis of measurement methods to characterise quantities related to the process stability and the properties of the manufactured part, with only a few attempts to develop automated defect detection techniques. In the last couple of years, instead, the number of studies presenting machine learning and data mining solutions for real-time feature extraction and anomaly detection or classification has exponentially grown: about 20% of studies published since 2018 presented a machine learning tool to process and analyse the in-situ gathered data (Wang et al. 2020a, Goh et al. 2021). Such fast and wide evolution of the state of the art has motivated the present study, whose main goal is to provide an up-to-date review of the many new results achieved so far and the research questions that still need to be answered.

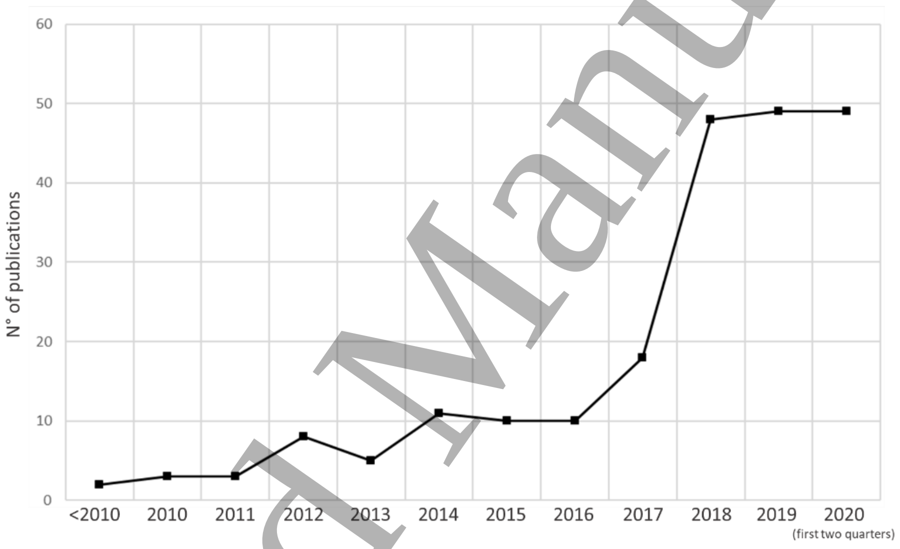

Figure 1. Number of publications presenting methods for in-situ sensing and/or in-situ monitoring of PBF processes (the figure includes all papers devoted to in-situ sensing and monitoring methods in PBF reviewed in the present study and it is based on Scopus and Google Scholar databases)

Special focus is devoted to the classification of the different quantities that can be measured during the process, also known as “process signatures”, and their correlation with detectable defects. The present study attempts to summarise and highlight the kind of defects and anomalies that are currently detectable and the suitable sensing and data analysis techniques for each of them. In-situ measurement methods are reviewed and compared in terms of spatial and temporal resolutions and other measurement performances, with special attention to issues related to their adoption on industrial systems. In-situ monitoring methods are reviewed and compared in terms of final performances (e.g., actual defect detection rate and localisation accuracy, misclassification rates), implemented algorithms, training needs and computational aspects.

This study focuses on laser and electron beam PBF processes (L-PBF and EB-PBF respectively) only (an overview of the PBF process can be found in Gibson et al. 2014, Spears and Gold 2016, Sing et al. 2021, Popov et al. 2021, Körner 2016, King et al. 2015). This choice is motivated by different factors. First, metal PBF processes currently represent the category of AM processes with the highest industrial maturity and spread (Leach and Carmignato 2020). Second, the largest part of the literature devoted to in-situ sensing, measurement and monitoring is concentrated on PBF applications. Third, L-PBF and EB-PBF are also the technologies where the highest maturity of industrial monitoring tools has been achieved so far, since all industrial PBF systems are equipped with various kinds of sensors and data collection, visualisation and storage tools. Several research institutes have also developed PBF prototype systems used to test and demonstrate innovative in-situ sensing, monitoring and control methodologies that are still difficult or impossible to validate on industrial systems. Despite such great variety of research and industrial efforts to make the most efficient and effective use of data gathered during the PBF process, many open issues still have to be addressed and, for some types of defects, there is still a lack of methods that are robust enough to be directly implemented in industry.

This study aims to provide an updated picture of both the potentials and limitations of the methods presented and tested so far. It is conceived as an updated review, with a special focus on more recent research published in the last three – four years, but also as a self-contained paper including a comprehensive picture of the literature since first seminal studies. The present review is therefore meant as a state-of-the-art analysis for experts, who are willing to have an update on most recent results and novel solutions, but also for readers and newcomers in the field, who are willing to have a first and thorough introduction to the research on in-situ measurement and monitoring approaches. A brief overview on process control and in-situ defect correction methods exploiting in-situ measured quantities completes the study, to highlight novel and future research directions towards novel generations of zero-defect AM capabilities.

The paper is organised as follows. Section 2 summarises the terminology and main definitions adopted in following Sections. Section 3 reviews in-situ measurement methods, focusing on the quantities that can be measured in-situ, methods of their measurement and the measurement performance that could be achieved. Section 4 reviews in-situ monitoring methods showing the defects and process anomalies that can be practically detected and classified and the defect detection capabilities that still need to be refined or developed. In Section 5, the overview of feedback and feedforward control methods that can take advantage of in-situ gathered data is briefly discussed. Section 6 concludes the paper and presents a discussion on open issues and future research directions.

2 Definitions and terminology

2.1. Terminology

Several terms referring to measurement and monitoring techniques are used in the literature and reviewed in this document. In some cases, there is inconsistency in the use of such terms, not only in the reviewed literature but also in different scientific fields. This Section provides a glossary of terms to avoid confusion on how different measurement and monitoring methods can be classified. The most relevant terms, for which a definition is provided below, are summarised in Fig. 2. We have adopted the definitions that were developed during a recent roadmap exercise in the UK (Leach 2020).

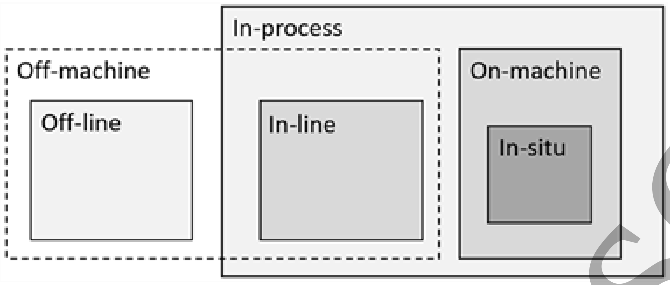

Figure 2. Graphical representation of different terms associated with measurement and monitoring techniques (from Leach and Carmignato 2020)

The term *"in-process*" refers to any measurement gathered during the process or between successive manufacturing steps within the same production line. In-process measurements are synchronised with the different stages of the manufacturing process so that the process can be monitored. When in-process measurements are performed right before, right after or between manufacturing stations, they are referred to as "in-line" measurements. In-line measurements are taken on separate measurement systems along the standard production line where manufacturing is not occurring. Therefore, they belong to the category of "*off-machine*" measurements, i.e., measurements carried out outside the machine where the manufacturing process occurs. When in-process measurements are performed using sensors that are installed on the machine where the process is occurring, they are referred to as "*on-machine*" measurements. On-machine measurements that primarily record data directly from the location where the process is occurring are referred to as "*in-situ*" measurements. The term "in-situ" is the most widely used in the AM literature to indicate sensing and monitoring techniques aimed at gathering information about the process stability and the product quality while the part is being produced. Finally, when measurements are not performed in-process, they are referred to as "*off-line*". They belong to the category of off-machine measurements as they are commonly performed outside the manufacturing environment, either on a measurement station in the factory that is separate from the production line or in a laboratory.

For the purposes of this review, we focus only on in-situ methods. In this field, it is possible to distinguish between "*in-situ measurement*" and "*in-situ monitoring*" methods. In-situ measurement refers to the ability to measure quantities with in-situ sensors, either to understand and characterise the process or to quantify quality characteristics of the part while it is being produced. "*In-situ monitoring*", instead, refers to the in-process detection of errors, anomalies and out-of-control process states that could lead to defects in the part, hence involves the definition of an alarm rule or a classification algorithm.

The present study first reviews in-situ measurement methods, focusing on which quantities can be measured and how (Section 3). In-situ monitoring methods are reviewed in Section 4, focusing on which defects can be practically detected during the process and how. A different task is "*process control*", i.e., a closed-loop control of process parameters at different temporal scales, e.g., from point to point, from track to track or from layer to layer, based on information gathered in-situ. A brief overview of process control methods is provided in Section 5.

2.2. Classification of measurement levels in PBF

The term "process signature" was first used by Mani et al. (2015) in the framework of in-situ sensing in AM. The term refers to one or more quantities that can be measured during the process to gather relevant information about the process stability, underlying physical phenomena and the onset of possible defects and errors. The process signatures of interest in PBF processes may be classified on the basis of the information they enclose, and the spatial and/or temporal scales involved in their measurement. In this study, we propose a classification of in-situ measurement methods that inherits classifications proposed in previous studies (Grasso and Colosimo 2017) and extends it to include new research directions arisen in the literature. Such classification involves the five levels shown in Fig. 3. With respect to the categorisation proposed in Mani et al. (2015), in this study we refer only to "observable signatures", i.e., measurable quantities, and we leave the discussion of "derived signatures", i.e., quantities estimated via process modelling, to the literature on PBF process simulation.

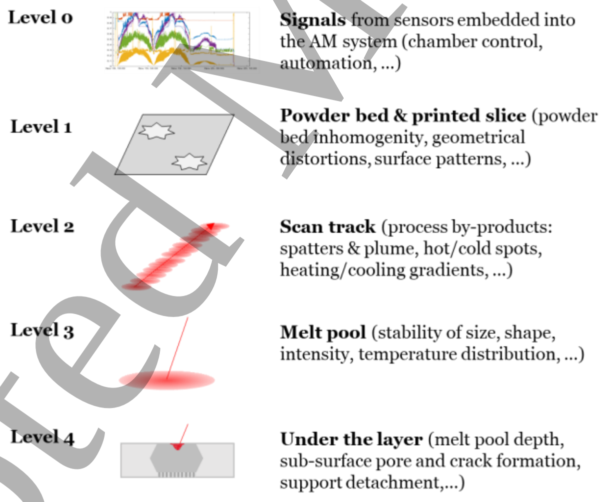

Figure 3. Five in-situ measurement levels applicable to PBF processes

Level 0 involves quantities that can be measured with embedded sensors typically used in PBF systems to keep machine states and environmental conditions under control. Level 0 measurements include chamber pressure, ambient temperature and oxygen content, current and torque signals from linear axis motors, inert gas flow, build plate temperature, status of installed filters, and other parameters. Such quantities are used to guarantee a normal machine functionality and stop the process in case of unproper operating conditions. Level 0 methods mentioned here refer to a different perspective, i.e., to a more advanced use of such signals to automatically detect anomalies and unstable process states that could possibly cause non-conforming part properties without activating machine state alarms.

Level 1 involves measurements gathered once (or more than once) per layer, with a field-of-view that covers the entire build area or a region of interest. Two families of process signatures can be envisaged at this level. The first involves quantities that are representative of the homogeneity of the powder bed and/or related to the presence of powder bed contaminations. The second involves either geometrical and dimensional features of the printed slice or its surface topography.

Level 2 includes quantities that can be measured with temporal resolutions considerably higher than those used in Level 1. Level 2 involves process signatures that can be measured while the laser or the electron beam is displaced within the build area to produce the current layer. This entails the capability to observe the interaction between the beam and the material, the thermal history of the process and its by-products, such as spatters and plume emissions.

Level 3 involves measurements of process signatures representative of the highest level of detail at which the PBF process can be observed in the current layer, i.e., the melt pool. The melt pool is known to be a primary feature of interest in any process that involves a beam-material interaction aimed at achieving a local fusion of the material.

Level 4 finally regards the capability of gathering information about phenomena occurring under the currently processed layer. It includes measurements that can be obtained with ad-hoc prototype machine configurations that enable transverse X-ray imaging, but also ultrasound and acoustic emissions caused by the release of elastic energy and plastic deformations in the solidified material.

Figure 4 shows how the literature devoted to in-situ measurement and monitoring for PBF processes is divided into these five measurement levels and more recent contributions (2018 – 2020) divided by monitoring level.

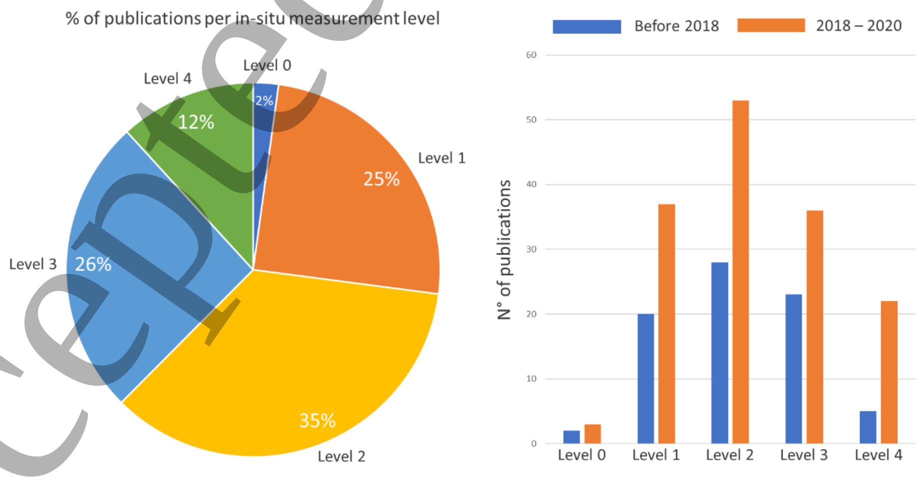

Figure 4. Overall percentage of publications per in-situ measurement level (left) and number of publications per in-situ measurement level and publication period (right) (the figure includes all papers reviewed in the present study)

Figure 4 shows that the largest portion of the literature is devoted to level 1, 2 and 3 methods. Level 4 methods have attracted increasing interest in the recent years due to the potentials of acoustic emission measurements and the development of novel L-PBF system prototypes with integrated X-ray video imaging.

In addition to the above mentioned levels, it is possible to divide in-situ measurements into two further categories based on the location of the sensor. "*Co-axial measurement*" refers to the use of sensors that are integrated directly into the laser's optical path (a configuration that is enabled only in L-PBF), whereas "*off-axis measurement*" refers to the use of sensors that are placed outside the optical path of the beam, which is suitable in both L- and EB-PBF.

3 In-situ sensing and measurement methods

3.1 Level 0 methods – Use of embedded sensors

Both L-PBF and EB-PBF systems require several embedded sensors to keep the build chamber environment under control and to guarantee the proper performance of the various process operations. However, publications proposed a more advanced in-process use of signals from such sensors only in EB-PBF applications as a possible source of information for in-situ anomaly detection (Grasso et al. 2018, Steed et al. 2017, Chandrasekar et al. 2020). Embedded sensor signals in EB-PBF are also known as "log signals". They include column and chamber temperature and pressure signals, filament current and voltage, grid current and voltage, pulse signals representative of powder dosing, duration of each process phases, and many more. Steed et al. (2017) pointed out that many of these EB-PBF log signals are correlated with process errors and variations in process conditions. However, due to the large number of signals and their complex dependencies, both data visualisation and automated detection of out-of-control patterns need the development of novel solutions. Steed et al. (2017) introduced "Falcon", a tool for visualisation and analysis of large multivariate time series data generated by embedded sensors in EB-PBF (Figure 5). The tool was used in studies to investigate correlations between log signals and actual defects in parts produced via EB-PBF (Yoder et al. 2017). Chandrasekar et al. (2020) showed that in situ analysis of rake position and rake sensor pulse signals could provide in-depth information about the powder spreadability.

The use of rake pulse sensor signals was also investigated by Grasso et al. (2018b), but with a different goal, i.e., the development of a statistical process monitoring tool for the automated detection of defects related to incorrect powder spreading conditions. Grasso et al. (2018b) showed that in-process monitoring of the rake sensor pulse signals allowed the anticipated detection of geometrical errors caused by anomalies in the powder recoating operation. These seminal studies open up either to further possible solutions in the framework of in-situ process monitoring that require no additional sensors, or to new data fusion methods to take advantage of multiple signals coming from both embedded and external sensors (Colosimo and Grasso 2020).

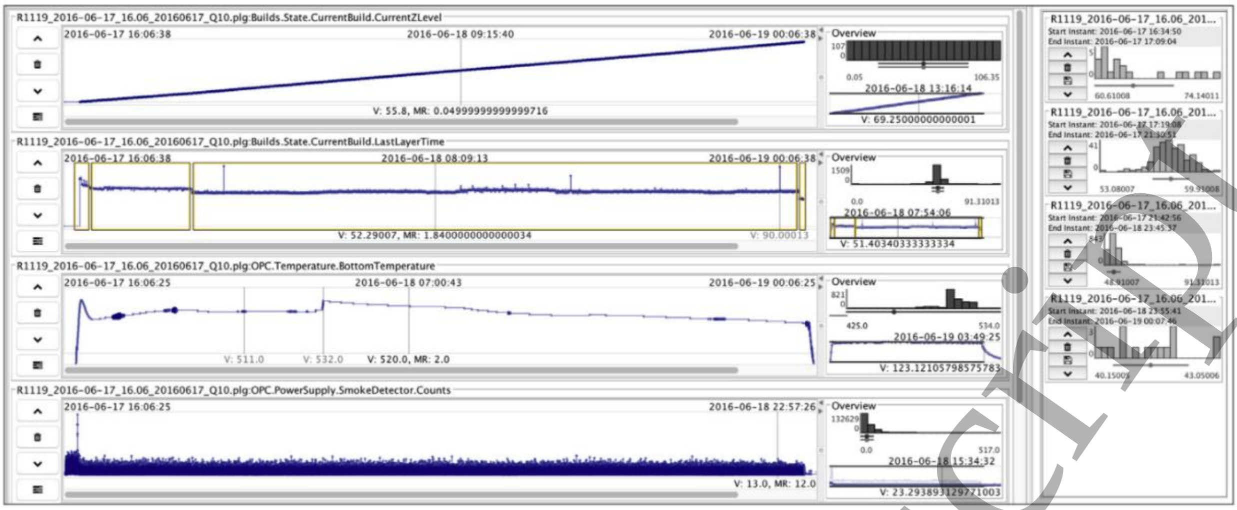

Figure 5. An example of the Falcon data visualisation interface, from Steed et al. (2017)

3.2 *Level 1 methods – Powder bed and printed slice*

In-situ measurement and characterisation of layer properties (including the printed slice, a.k.a, the solidified layer, observed at the end of the melting phase, and the loose powder bed observed after the recoating operation) represent the primary way in which the layerwise production paradigm can be exploited for in-process qualification. By observing each layer, a large amount of information about process stability and part quality can be gathered. Measurements performed before laser or electron beam scanning inform about the presence of raw powder inhomogeneities, defects produced by the recoating system (rippling, bouncing effects, etc.) and the presence of so-called super-elevated edges, i.e., areas of the previously printed slice that could not be fully covered by the new powder layer. Measurements performed after scanning, instead, enable the characterisation of the printed slice as well as the powder bed contamination caused by the beam-material interaction and process by-products.

As far as the analysis of the printed slice is concerned, two major streams of research can be identified. One regards the characterisation and detection of out-of-plane irregularities in the printed area and its surface topography. Irregular surface patterns may produce undesired variability in the local powder thickness, with a resultant undesired variation of the actual energy density provided to the material. Surface irregularities may also interfere with the recoating operation, generating a propagation of defects within the build area. Another stream of research regards the reconstruction of the contours of the printed area to identify geometrical and dimensional deviations from the nominal shape. Table 1 summarises and classifies the literature devoted to level 1 methods depeding on the measured signatures of interest and the sensing equipment in L-PBF and EB-PBF.

Table 1 – Literature devoted to level 1 in-situ sensing and measurement methods

Signatures of interest	Sensing method	References (L-PBF)	References (EB-PBF)
Surface pattern or height map of the powder bed	Off-axis imaging in visible range	Scime et al., 2020; Angelone et al., 2020; Zur Jacobsmuhlen et al., 2015; Scime and Beuth, 2018a,b; Foster et al., 2015	Grasso et al., 2020;
	Fringe projection (with single or multiple off-axis cameras)	Land et al., 2015; Zhang et al., 2016a,b	Liu et al. 2020a; Liu et al. 2019;
	Blade-mounted sensor	Phuc and Seita, 2019; Barrett et al., 2018b	
Surface pattern or height map of the printed slice	Off-axis imaging in visible range	Scime et al., 2020; Lu et al., 2020; Scime and Beuth, 2018a,b; Aminzadeh & Kurfess, 2019; Angelone et al., 2020; Imani et al., 2019a,b; Lu et al., 2019; Gobert et al., 2018; Abdelrahman et al., 2017; Kleszczynski et al., 2014; Zur Jacobsmuhlen et al., 2015; Kleszczynski et al., 2012	
	Off-axis NIR/IR imaging	Mahmoudi et al., 2019; Bamberg et al., 2016	Yoder et al., 2019; Yoder et al., 2018; Nandwana et al., 2018; Mireles et al., 2015; Schilp et al., 2014; Ridwan et al., 2014; Schwerdtfeger et al., 2012; Rodriguez et al., 2012
	Fringe projection (with single or multiple off-axis cameras)	Zhang et al., 2016a, b; Land et al., 2015; Zhang et al., 2015; Kalms et al., 2019	Liu et al. 2020a; Liu et al. 2019
	Blade-mounted sensor	Erler et al., 2014; Barrett et al., 2018b	
	Inline coherent imaging	Fleming et al., 2020; Depond et al. 2018; Neef et al., 2014	
	Electronic imaging		Wong et al., 2020; Wong et al., 2019a,b, 2018; Pobel et al, 2019; Arnold et al., 2019; Arnold et al., 2018
Geometry of the printed slice	Off-axis imaging in visible range	Pagani et al., 2020; Zur Jacobsmuhlen et al., 2019; Gobert et al., 2018; Caltanissetta et al., 2018; Gaikwad et al., 2019; He et al., 2019; Foster et al., 2015	Wong, 2020
	Blade-mounted sensor	Barrett et al., 2018b	

As shown in Table 1, level 1 methods include a variety of sensing techniques, which produce different data formats and lead to different measurement performances and capabilities (Table 2). It is worth noting that in most reviewed studies, the term "spatial resolution" is commonly used in place of "instantaneous field of view" (iFoV), whereas the true spatial resolution depends on the inherent optical blur (Lane et al. 2016b). In this Section and in following ones, the term "spatial resolution" will be used to indicate the width of an individual pixel on the measurement surface.

Sections 3.2.1 to 3.2.5 review the in-situ sensing and measurement methods shown in Table 1 and Table 2.

Table 2 – In-situ measurement performances for level 1 methods (includes only references where resolution values were specified)

Sensing method	Process	Spatial (lateral) resolution /µm/pixel	Vertical resolution /µm/pixel	References
Off-axis imaging in visible range	L-PBF	7	na	Aminzadeh and Kurfess, 2018
		10 – 13 µm/pixel		Lu et al., 2020
		20		Caltanissetta et al., 2018
		24		Kleszcsynski et al., 2012, Zur Jacobsmulhen et al., 2015, 2013
		20 - 30		Zur Jacobsmulhen, 2019
		15 - 50		Foster et al., 2015
		50		Gobert et al., 2018
		45 – 88		Abdelrahman et al., 2017
		125		Pagani et al., 2020
		20 – 290		Scime et al., 2020
		290		Scime and Beuth, 2018a,b
Off-axis NIR/IR imaging	L-PBF	25	na	Mahmoudi et al., 2019
		100		Bamberg et al., 2016
		830		Schwerdtfeger et al., 2012
	EB-PBF	100		Yoder et al., 2019, 2018, Nandwana et al., 2018
		170		Ridwan et al., 2014
		350		Rodriguez et al., 2012
Fringe projection (with single or multiple off-axis cameras)	L-PBF	6.8	-	Zhang et al., 2016a,b, Land et al., 2015
		60	-	Zhang et al., 2015
		72 – 76	-	Dickins et al., 2020
		100	<10	Kalms et al., 2019
	EB-PBF		<20	Liu et al. 2020a, 2019
Blade-mounted sensor	L-PBF	5.3	na	Phuc and Seita, 2019
		20	-	Barrett et al., 2018
Inline coherent imaging	L-PBF	30	7	Fleming et al., 2020
		100	25	Depond et al., 2018
Electronic imaging	EB-PBF	33.33	na	Wong et al., 2020
		320 - 358		Wong et al., 2019a,b
		60		Arnold et al., 2020, 2018
		50 - 100		Pobel et al., 2019

3.2.1. *Off-axis imaging in the visible range*

Powder bed cameras are already available in most L-PBF systems, hence the development of in-situ measurement and monitoring methods, based on such sensing setups, has the advantage of being easily implementable in industry. Seminal works demonstrated the feasibility of layerwise imaging techniques for the detection of powder bed irregularities (Kleszczynski et al. 2014, Zur Jacobsmuhlen et al. 2015, Kleszczynski et al. 2012, Foster et al. 2015) and powder bed monitoring algorithms have already been implemented by L-PBF system developers (a summary of commercial monitoring toolkits is reported in Colosimo and Grasso 2020).

The capability to detect local inhomogeneity in the powder bed and/or irregular surface patterns requires a machine vision setup involving a sufficient spatial resolution and appropriate lighting conditions. The importance of lighting conditions was pointed out by different authors (Kleszczynski et al. 2012, zur Jacobsmulhen et al. 2015, Foster et al. 2015, Abdelrahman et al. 2017). Caltanissetta et al. (2018) and Gobert et al. (2018) investigated and compared different illumination sources, showing that significantly different layerwise image processing performances could be achieved by varying the lighting conditions. Fig. 6 shows examples of layerwise images with different lighting conditions Gobert et al. (2018) .

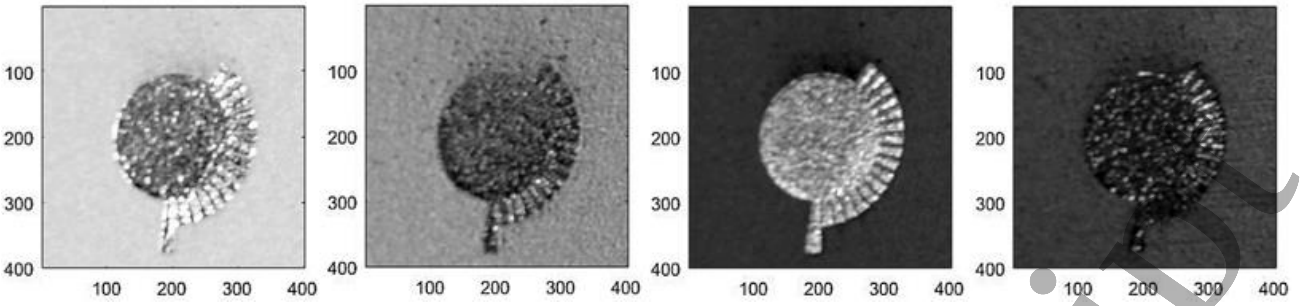

Figure 6. In-situ powder bed images using different single lighting conditions, adapted from Gobert et al. (2018)

In most studies, high spatial resolution cameras where installed on L-PBF machines exploiting available viewports, but in a few cases, powder bed cameras and illumination conditions already available in industrial systems were used, without any modification of the original setup (Scime et al. 2020, Pagani et al. 2020). Recent studies focused on the automated extraction of features from powder bed images for the classification of irregularities within both loose powder regions and previously melted areas (Scime and Beuth 2018a,b, Aminzadeh and Kurfess 2018, Lu et al. 2020, Gobert et al. 2018). Despite being a relatively mature solution in L-PBF, powder bed homogeneity monitoring via off-axis optical imaging has been investigated in only one study in EB-PBF (Grasso et al. 2020). Indeed, the high temperature differences within the powder bed in EB-PBF after powder recoating, and the difficulty to install additional sensors on EB-PBF machines, makes this kind of in-situ monitoring more challenging than in L-PBF.

Layerwise optical imaging allows also the reconstruction of slice geometry. After the seminal work of Foster et al. (2015), various authors studied and tested layerwise image segmentation techniques in L-PBF to this aim. Caltanissetta et al. (2018) showed that, by combining appropriate image pre-processing and segmentation algorithms with suitable lighting configurations, sufficient measurement accuracy and repeatability to detect major geometric deviations could be achieved. Pagani et al. (2020) extended the study of Caltanissetta et al. (2018) by presenting a tuned image segmentation approach that is robust to non-optimal illumination conditions. Other methods for in-situ slice contour detection have been proposed by Aminzadeh and Kurfess (2016), Gaikwad et al. (2019), He et al. (2019) and zur Jacobsmuhlen et al. (2019). It is worth noting in-situ geometry reconstruction is not suitable for comparison against final tolerances carried out in situ. Indeed, tight tolerances commonly foree post-processing and finising steps and some deviations (e.g., shrinkage and thermal stress-induced distortions) may not be captured on a layer-by-layer basis. Nevertheless, in-situ geometrical inspection could be suitable to anticipate the detection of anomalies that could be difficult or impossible to recover in post-processing (Pagani et al. 2020).

3.2.2. *Off-axis imaging in the NIR/IR range*

In L-PBF, some authors used NIR layerwise imaging for surface pattern analysis. Bamberg et al. (2016) presented a method called “optical tomography”, currently implemented by EOS in the EOSTATE monitoring toolkit. The surface pattern of the printed area was reconstructed by translating off-axis NIR video frames, acquired during the the melting phase, into a layerwise image. Fig. 7 shows an example of layerwise patterns reconstructured via the optical tomography method discussed by Bamberg et al. (2016). Mahmoudi et al. (2019) generated layerwise images by combining thermal images of the melt pool acquired via an off-axis two-wavelength thermal camera.

Layerwise NIR and IR imaging have been more commonly used in E-PBF, due to the hot nature of the process. In the seminal works of Schwerdtfeger et al. (2012), Rodriguez et al. (2012), Ridwan et al. (2014) and Mireles et al. (2015), layerwise IR vision was used to characterise the surface pattern of printed areas to detect flaws and surface anomalies. More recently, Yoder et al. (2018, 2019) and Nandwana et al. (2018) used a layerwise imaging system called "LayerQam", developed by Arcam (GE Additive) for integration in its EB-PBF machines. The system consists of a NIR camera that acquires an image of the layer after the melting phase. Local pixel intensity variations and the presence of bright spots were used as proxies of possible volumetric flaws and material discontinuities in studies that correlated in-situ and ex-situ inspection results.

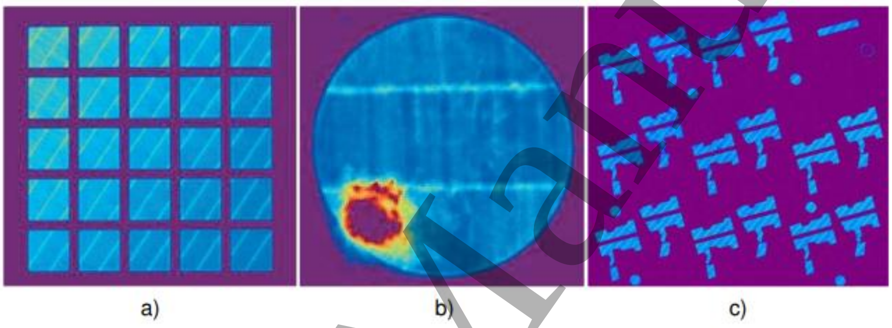

Figure 7. Examples of optical tomography images for cubic samples with variation of energy density (a), a cylinder produced under shielding gas flow variation (b) and defect-free complex shapes (Bamberg et al., 2016)

3.2.3. Fringe projection

Off-axis imaging methods discussed in the previous sub-Sections are suitable to provide a 2D reconstruction of the powder bed and the printed slice. Local pixel intensity variations represent the only suitable driver to determine possible surface irregularities. Other methods have been applied in PBF processes to obtain a 3D reconstruction of the height map of the powder bed. One technique proposed by different authors is fringe projection, which enables a combination of layer imaging and topographical analysis. The technique requires one or multiple cameras and a projector: various configurations have been proposed in the literature, mainly for L-PBF.

The simplest configuration exploits a single camera (single-view setup). With this approach, Zhang et al. (2016a) upgraded a method previously presented by the same authors (Zhang et al. 2016b and Land et al. 2015). Land et al. (2015) pointed out that the most important factors in determining the resolution of the height map are the spatial frequency of the projected fringes onto the build plane (that depends on the pixel density of the projector) and the geometric arrangement of the imaging hardware, which, in L-PBF applications, is constrained by the chamber size and the location of available viewports. Other authors proposed and tested multi-view configurations, with two or more cameras, suitable to achieve higher resolution and accuracy (Kalms et al. 2019, Dickins et al. 2020) and an example of surface reconstruction based on these methods is shown in Fig. 8. In terms of defect detectability, the recently published study by Dickins et al. (2020) presented a multi-view fringe projection system comprising four cameras now commercialised via Taraz Metrology, which is suitable to detect defects and anomalies with sizes larger than 100 µm with a horizontal field of view of about 350 mm.

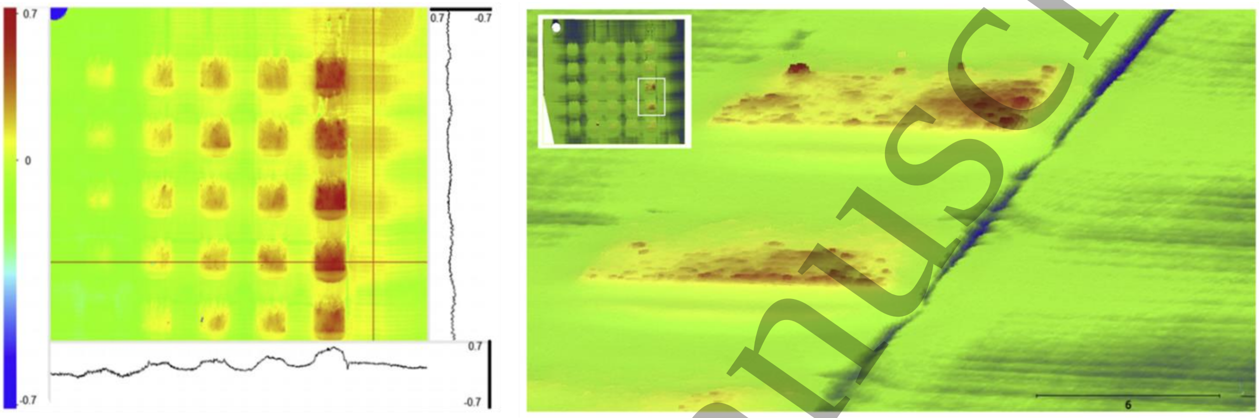

Figure 8. Example of height map and height surface profiles gathered through a multi-view fringe projection approach (values in millimeters, field of view of (150 × 150) mm) (Kalms et al., 2019)

The use of fringe projection in EB-PBF on commercial machines from Weyland Precision was investigated by Liu et al. (2019, 2020a). The fringe projection measurements were taken during the time window between powder recoating and fusion and after EB melting. The proposed system involved a single-view architecture.

3.2.4. Blade mounted sensors

A few authors explored the idea of using sensors mounted on the recoater to gather a full-field and high spatial resolution 2D scan of the powder bed surface, similarly with flatbed document scanners. Tan Phuc and Seita (2019) installed a linear optical sensor on the recoater and equipped the L-PBF system with a microcontroller to synchronise the recoater speed with the image acquisition. With an optical resolution of 4800 dots-per-inch (DPI) over a length of 210 mm, a spatial resolution of 5.3 µm/pixel was achieved. By using the optical video imaging methods discussed in Section 3.2.1, analogous spatial resolutions could be achieved even with a limited field of view. Moreover, the line-scanning approach avoids any perspective distortions and issues related to non-homogeneous illumination conditions within the build area. Tan Phuc and Seita (2019) showed that their proposed approach could be used, not only for 2D surface pattern characterisation of the entire powder bed, but also to detect irregularities along the vertical direction. Due to the small depth-of-field of the linear sensors, super-elevated edges and variations in the powder layer thickness were shown to fall out of the focal plane, resulting in “blurred” areas in the acquired images. Fig. 9 shows an example of a powder bed image obtained with the line-scanning methods presented by Tan Phuc and Seita (2019) and the corresponding estimate of the height map.

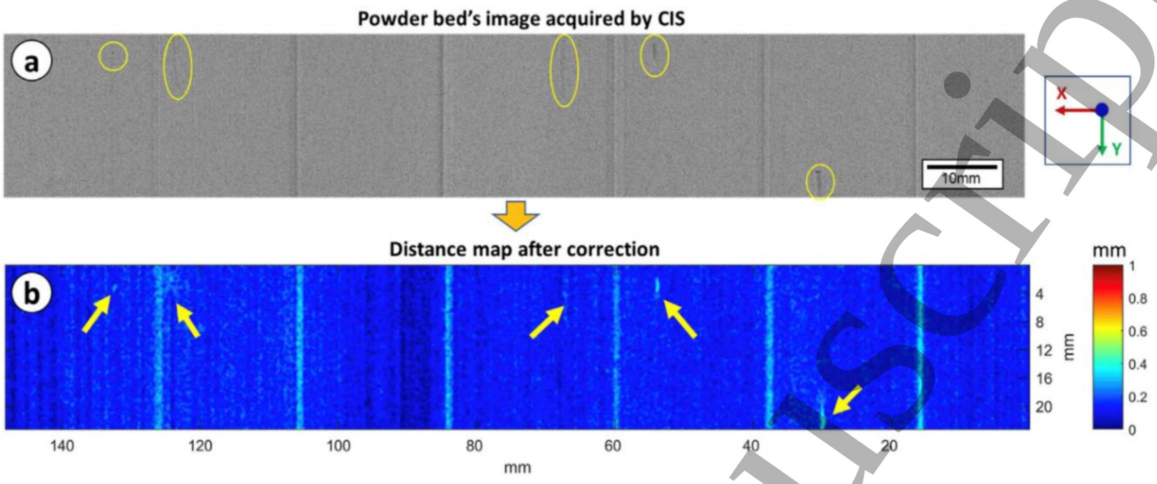

Figure 9. Example of high spatial resolution powder bed line-scan optical imaging (top) and corresponding reconstruction of irregularities based on focus level mapping (b) (Tan Phuc and Seita, 2019)

In a previous work, Barrett et al. (2018b) mounted a high-resolution laser triangulation line-scan system on the recoater arm of an L-PBF machine, to perform surface mapping of the powder bed before and after the melting phase. A similar concept was first proposed by Erler et al. (2014). The advantage of this approach, compared to that presented by Tan Phuc and Seita (2019), is the effective capability of reconstructing the powder bed topography via a height map. However, the obtained lateral resolution was lower than that reported by Tan Phuc and Seita (2019) (the commercial triangulation system used by Barrett et al. (2018b) was characterised by a profile data interval of 20 μm and the laser scanner spans only a small fraction of the powder bed, i.e., a 15 mm scan width).

3.2.5. In-line coherent imaging

Rather than using an optical point or line triangulation instrument, some authors proposed a technique known as low-coherence interferometry or in-line coherent imaging, where the L-PBF laser beam itself is used, at the end of the melting phase, to reconstruct the surface topography of the layer (Fleming et al. 2020, Depond et al. 2018, Neef et al. 2014). This approach exploits a co-axial sensing configuration to collect local height measurements by raster scanning the area with an imaging beam, collecting the backscattered radiation and interfering it with a reference beam. The imaging beam is directed through the same lens used by the processing beam, which prevents the need for perspective corrections (Fleming et al. 2020). The seminal work of Neef et al. (2014) demonstrated the feasibility of the method. The topography to be captured was exposed to the radiation of a broadband light source integrated into the sensor within a (3 × 3) mm area scanned with a grid pattern of 4 μm sampling distance. The region of interest was raster scanned at nearly constant speed, with pulses generated at defined pixel positions to trigger the optical sensor. With such a high lateral resolution, the resulting height map could be used to detect single powder particles and defects of lateral size lower than 50 μm. Two more recent studies further investigated the potential of this approach. Fleming et al. (2020) used a sensing apparatus enabling a vertical resolution of 7 μm and a lateral resolution of 30 μm. Fleming et al. (2020) also proposed a method to combine the in-line coherent imaging measurement with an in-situ surface topography correction method that exploits the same L-PBF laser for ablation of the layer surface. In Depond et al. (2018), the surface topography of a (44 × 44) mm square region was measured with a lateral resolution of 100 μm and a vertical resolution of 25 μm. The vertical resolution is theoretically limited by the coherence length of the light source (with the setup used by Depond et al. (2018), the theoretical limit was about 5 μm). The lateral resolution is limited by the beam diameter and the sampling strategy along the raster scanning direction. This method also requires a raster scan of the area after the melting phase, inflating the overall process duration.

Fig. 10 shows an example of in-situ topography reconstruction via in-line coherence imaging from Neef et al. (2014). A different use of co-axial in-line coherent imaging for melt pool morphology monitoring was presented by Kanko et al. (2016) and is discussed in Section 3.4.

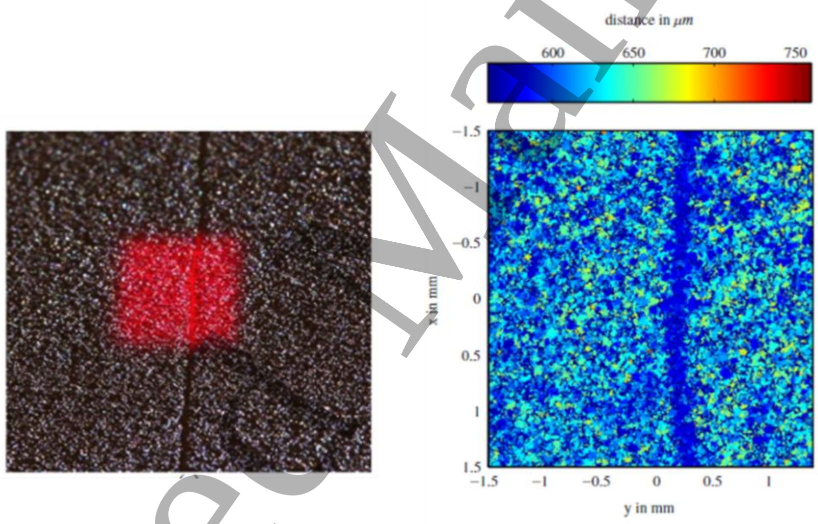

Figure 10. Region of interest covered by the inline coherent imaging (left) and corresponding in-situ topography reconstruction (right) (Neef et al., 2014)

3.2.6. Electronic imaging

In EB-PBF, process by-products include secondary and backscattered electrons and X-rays. Thus, in principle, the electrons produced as by-products of the beam-material interaction could be used, in a scanning electron microscopy mode, to generate an electronic image of the layer. This idea has been explored and tested by various researchers. Wong et al. (2019a) presented a pilot study involving an in-house developed electronic imager. The system was installed on an Arcam A1 machine. The electron beam was used to scan the layers and metal surfaces while the heat shield was used as an electron collector. A raw image was produced, where each pixel value was proportional to the signal strength of backscattered and secondary electrons. In a more recent work, the same authors showed the layerwise generation of bitmap images of the printed areas, for comparison against the nominal shape from the sliced CAD model (Wong 2020) and investigated the possibility of detecing different materials within the build area (Wong et al. 2020).

Arnold et al. (2018) used the same approach, but only using backscattered electrons, and installed a circular backscattered electron detector shortly above the build chamber of an Arcam S12 machine. Arnold et al. (2018) demonstrated that this configuration enabled a much higher spatial resolution (60 μm/pixel). In this study, and in all previously mentioned studies, the electronic image was generated at the end of the melting phase by performing a raster scan of the entire build area with the electron beam. Arnold et al. (2020) demonstrated, instead, that the same image could be generated during the melting phase, leading to an "in-operando" monitoring capability. Along the direction orthogonal to the scan tracks, the resulting image resolution was equivalent to the hatch spacing (between 50 μm/pixel and 100 μm/pixel in the published work). Along the scan direction, the resolution was limited by the scan speed and the sampling rate of the measurement system, and was significantly higher than that in the other direction. In order to get square-shaped pixels, the data was downsampled to the lowest resolution.

Fig. 11 shows some examples of electronic images in EB-PBF from Wong et al. (2019a) and Arnold et al. (2020).

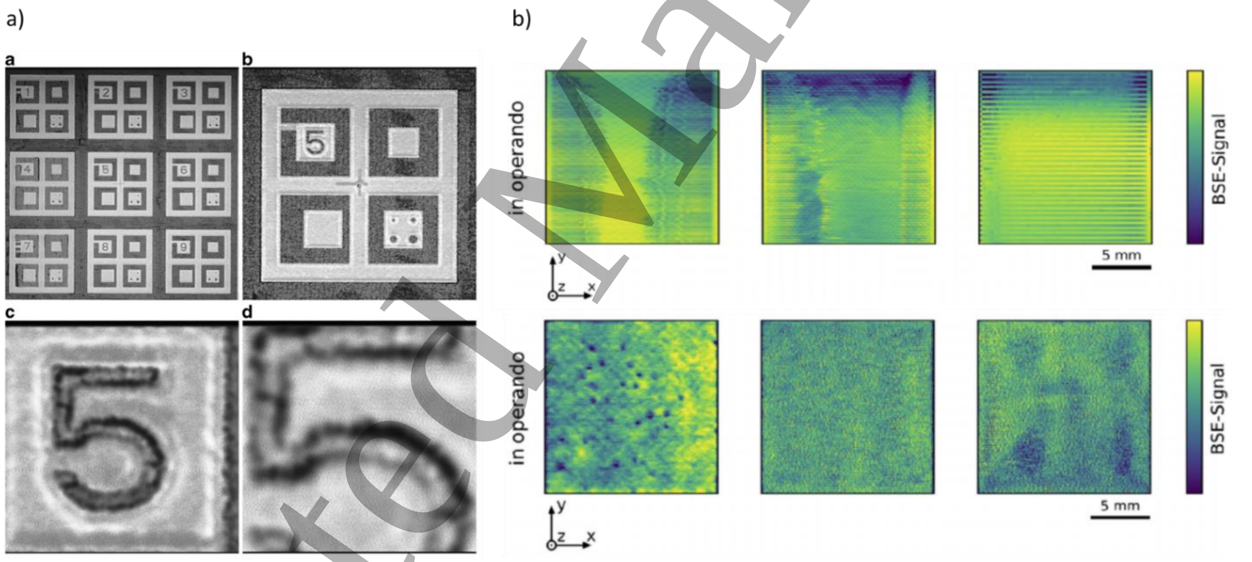

Figure 11. Examples of electronic images in EB-PBF: a) images with different magnification factors from Wong et al. (2019a), b) images of squared printed areas generated via in-operando backscattered signal acquisition from Arnold et al. (2020) for different materials (top panels: X15CrNiSi20-12, bottom panels: Ti6Al4V) with hatch spacing increasing from left to right (50 μm, 100 μm, 200 μm).

3.3 *Level 2 methods – Scan track*

In-situ process monitoring at track level involves in-process measurements of fast transient phenomena and high-speed emissions during laser or electron beam scanning. Studies in the literature can be divided into two major streams of research. The first regards measurements related to the local or global cooling history, either for the characterisation of spatio-temporal thermal gradients in each layer or for the detection of anomalous heat exchanges and cooling patterns. The second research stream involves the in-process measurement of quantities related to the by-products of the L-PBF process, i.e., spatters and plume emissions. The aim is either to understand underlying physical phenomena through the study of process by-products or to detect unstable process conditions and improper energy inputs.

A third field of research in L-PBF is the in-situ measurement of acoustic emissions associated with air density variations caused by plasma formation and plume emissions during the laser scanning of the part. According to the nomenclature commonly used in laser welding (Ali and Farson 2002), these acoustic emissions are called air-borne emissions and can be captured by microphones or other sensors in the vicinity of the melting area. These acoustic emissions are different from the so-called structure-borne emissions, which require the contact sensors discussed in Section 3.5. A classification of the literature devoted to level 2 in-situ sensing and metrology is shown in Table 3.

Table 3 – Classification of the literature devoted to level 2 methods

Signatures of interest	Sensing method	References (L-PBF)	References (EB-PBF)
Heatmap / heating and cooling profiles	Off-axis video-imaging in the visible range	Yan et al., 2020; Colosimo and Grasso, 2018; Grasso et al., 2017	Grasso et al. 2020; Lee et al., 2018
	Off-axis NIR/IR video imaging	Mohr et al., 2020; Heigel et al., 2020a,b; Lough et al., 2020b; Paulson et al., 2020; Baumgartl et al., 2020; Gaikwad et al., 2020; Jalalahmadi et al., 2019; Plotnikov et al., 2019; Elwarfalli et al., 2019; Lough et al., 2019; Williams et al., 2019; Foster et al., 2018; Bartlett et al., 2018; Montazeri and Rao, 2018; Alldredge et al., 2018; Bamberg et al., 2016; Lane et al., 2016b; Schilp et al., 2014; Krauss et al., 2014; Krauss et al, 2012	Boone et al., 2018; Cordero et al., 2017; Raplee et al., 2017; Rodriguez et al., 2015; Price et al., 2014; Gong et al., 2013; Price et al., 2012
	Off-axis multispectral pyrometry	Montazeri et al., 2020; Mitchell et al., 2020; Dunbar and Nassar, 2018	Cordero et al., 2017
Process by-products (spatters and plume)	Off-axis video-imaging in the visible range	Yang et al., 2020a, b; Tan et al., 2020; Yin et al., 2020; Zhang et al., 2019a, b; Nassar et al., 2019; Bidare et al., 2018a,b; Zheng et al., 2018; Zhang et al., 2018; Ye et al., 2019, 2018a; Andani et al., 2018; Ozel et al. 2018; Repossini et al., 2017; Ly et al. 2017; Andani et al., 2017; Liu et al., 2015; Bidare et al., 2017	
	Off-axis stereo vision in the visible range	Eschner et al., 2020a; Eschner et al., 2019; Barrett et al., 2019; Barrett et al., 2018a	
	Off-axis NIR/IR video imaging	Yang et al., 2020b; Grasso and Colosimo, 2019; Grasso et al., 2018a; Ozel et al., 2018	
	Off-axis X-ray video imaging	Young et al. 2020; Leung et al., 2019; Guo et al., 2018; Zhao et al., 2017	
	Off-axis Schlieren video-imaging	Bidare et al., 2018a,b; Bidare et al., 2017	
Air-borne acoustic emissions	Air-borne acoustic emission detector	Shevchik et al., 2019; Wasmer et al., 2019; Ye et al., 2018b; Kouprianoff et al. (2018)	

Level 2 monitoring methods involve off-axis mounted sensors, mainly cameras in the visible range or thermal cameras. Unlike in level 1 methods, high temporal resolution is needed to capture fast and transient phenomena, whereas high spatial resolution is needed to characterise the spatial features of interest.

Section 3.3.1 reviews in-situ sensing and measurement methods devoted to thermal mapping and reconstruction of heating/cooling patterns. Section 3.3.2 reviews in-situ sensing and measurement methods devoted to the analysis of process by-products in L-PBF, i.e., spatters and plume emissions.

3.3.1. Measurement of process heatmap and heating/cooling profiles

The layerwise manufacturing paradigm allows the “seeing” of the thermal history of the process, in time and in space. Almost all major quality characteristics of the final part and its mechanical performance depend on the thermal history (Williams et al. 2019). Local and global variations of heating and cooling patterns may indicate either a lack of fusion or excessive heat accumulation with resultant effects on material solidification at volumetric, microstructural and geometrical levels. Table 4 classifies the literature in this field in terms of measurement methods, wavelengths and associated spatial and temporal resolutions.

Table 4 – Measurement wavelength range and spatial/temporal resolution of methods applied in L-PBF and EB-PBF

Wavelength range	Process	Spatial (lateral) resolution /µm/pixel	Temporal resolution /Hz	References
Visible	L-PBF	150	300	Yan et al., 2020; Colosimo and Grasso, 2018; Grasso et al., 2017
	EB-PBF	100 76	600 12,000	Grasso et al. 2020 Lee et al., 2018
NIR	L-PBF			-
	EB-PBF	66 – 79 46.8 – 66.2 8 – 47	- up to 60 up to 60	Boone et al. 2018 Gong et al., 2013 Price et al., 2012, 2014
Short wave IR	L-PBF	36 34 - 52 130 - 36-53.3	1,800 1,800 2,500 - 1,800	Montazeri and Rao, 2018 Heigel et al. 2020a,b Lough et al., 2020b; 2019 Gaikwad et al., 2020 Lane et al., 2016b
	EB-PBF			-
Medium wave IR	L-PBF	- - 100 -	50 346.7 900 10,000	Baumgartl et al., 2020 Foster et al., 2018 Mohr et al., 2020 Paulson et al., 2020
	EB-PBF	35	10	Raplee et al., 2017; Dehoff et al., 2019
Long wave IR	L-PBF	195 - 260 - 1000 250 - 760	7 30 60 50 1,315 1,300	Bartlett et al., 2018 Plotnikov et al., 2019 Williams et al., 2019 Krauss et al., 2012 - 2014; Schilp et al., 2014; Alldredge et al., 2018 Jalalahmadi et al., 2019
	EB-PBF	175 - 350	-	Cordero et al., 2017; Rodriguez et al., 2015; Mireles et al., 2015
Dual wavelength	L-PBF	Not applicable	100	Montazeri et al., 2020; Dunbar & Nassar, 2018
	EB-PBF	-	-	Cordero et al., 2017

It is possible to distinguish between two major streams of research. One aimed at reconstructing a heatmap of the layer combining information gathered at low speed (up to 50 fps), while another aimed at capturing fast heating and cooling transients, with temporal resolutions from 300 fps to more than 10000 fps. In terms of spatial resolution, it is also possible to identify two major categories of measurement approaches. On the one hand, in-situ measurement setups with a field of view limited to a small portion of the build area enable resolutions in the range 8 µm/pixel to 100 µm/pixel. On the other hand, in-situ measurement setups with a field of view covering the entire build area enabled lower spatial resolutions, typically above 100 µm/pixel.

Thermal cameras have been used in both L-PBF and EB-PBF either in the short wave IR (~0.9 µm to 2.5 µm), medium wave IR (2 µm to 5 µm) or long wave IR range (7.5 µm to 14 µm or more). In L-PBF, Montazeri and Rao (2018), Gaikwad et al. (2020) and Heigel et al., (2020a,b) used short wave IR video imaging to capture thermal signature variations throughout the build of overhang features and bridges. The choice of a narrow short wave IR bandwidth (from 1.35 µm to 1.6 µm) was motivated by Heigel et al., (2020a,b) to filter out the laser wavelength and to minimise possible temperature measurement errors related to wavelength-dependent emissivity values. Short wave IR video imaging was used by Lough et al. (2019, 2020b) differently. They used features extracted from the thermal map to generate a voxel-based representation of the part, to be correlated with its local and global quality characteristics. Lane et al (2016b) used a MWIR camera with a short wavelength filter to reduce the temperature measurement uncertainty due to inaccurate emissivity estimations, since this uncertainty can be reduced at short wavelengths.

Despite their higher sensitivity to emissivity values for absolute temperature estimation, thermal cameras operating in the medium or long wave IR range can be calibrated in a wider temperature interval than that of short wave IR cameras, with high sensitivity even at high temperatures. This makes them the most utilised sensors for in-situ thermal video imaging applications in both L-PBF and EB-PBF.

In some cases, thermal maps of the layer were generated by selecting frames acquired during different phases of the process (Bartlett et al. 2018), Jalalahmadi et al., 2019) or by averaging video frames (Plotnikov et al. 2019). Whereas most studies focused on the analysis of the thermal map of each layer, Williams et al. (2019) focused on the temperature evolution along the build, analyzing the impact of the inter-layer cooling time on the final quality and mechanical properties of the parts. They showed that the number of parts in the build and the way in which they are spatially located have a significant effect on the quality of the manufactured part as a result of its thermal history.

Other authors used high temporal resolution IR video imaging in L-PBF to enhance the capability of reconstructing temperature profiles in space and time, additionally capturing transient and fast phenomena. Foster et al. (2018) used high-speed IR videos to estimate local peak IR intensities within the scanned areas and correlate their maximum value with different processing parameters. Mohr et al. (2020) applied a feature extraction approach to high-speed thermographic data to determine the time that a surface element was at an apparent temperature above a certain threshold, also called “time over threshold”; the same indicator was used by Paulson et al. (2020). An image from the study presented by Paulson et al. (2020) and the local estimation of the time over threshold indicator is shown in Fig. 12. Mohr et al. (2020) also showed that combining synchronous video imaging at high spatial resolution (NIR camera) and high temporal resolution (medium wave IR camera) increased the capability of detecting volumetric defects compared to imaging with a single sensor.

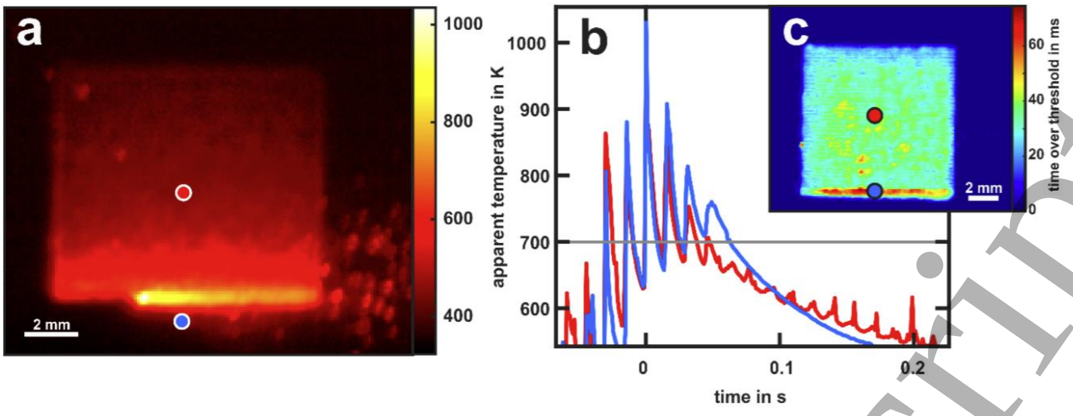

Figure 12. An example of in-situ reconstruction of local cooling profiles via high-speed IR video imaging and the "time over threshold" index computation by Mohr et al. (2020)

In EB-PBF, in-situ video imaging methods need to be adapted to face specific characteristics of the process. Both conventional and thermal cameras need to be protected from X-ray emissions and metallisation. To this aim, available viewports can be equipped with leaded glass and a rolling Kapton film to prevent metal vapour from adhering to the window. The Kapton film has an IR transmission of about 79%, whereas a 10 mm thick leaded glass window has an IR transmission of 1.08% (Dinwiddie et al. 2013). However, due to the high temperatures involved in the process, detailed IR imaging capabilities were shown in the literature, despite such reduced transmission. Other researchers (Rodriguez et al. 2015) used a mechanical shutter to protect the viewport from metallisation, enabling image acquisition within a brief interval only. In-situ thermography in EB-PBF was further used by Cordero et al. (2017), Raplee et al. (2017) and following studies by the same researchers (Dehoff et al. 2019).

Although IR cameras enable accurate measurements of thermal gradients in space and time, the estimation of absolute temperatures is difficult to achieve. PBF processes involve fast phase transitions from powder to liquid then to solidified material, in addition to continuous changes in surface properties and emissions of the vapourised material, which limit the feasibility of accurately estimating the emissivity needed to convert raw signals into temperature values. In several in-situ monitoring applications, the variation of the thermal signature over time is more relevant than the estimation of the absolute temperature. In those cases, data processing and monitoring algorithms can be directly applied on raw signals, i.e., measured radiance values in arbitrary units. When accurate estimates of the true temperature are needed, different methods can be used. A simple but less accurate approach used by some authors (e.g., Price et al. 2014) consists of selecting the emissivity value to set the temperature measured within the melt-pool region at the known liquid–solid transition temperature of the material. Other studies described calibration procedures using heated calibration artefacts, which enable more accurate estimates. These include the methods presented by Williams et. (2019), Dinwiddie et al. (2013) and Rodriguez et al. (2015), involving ad-hoc designed components whose temperature was measured by both thermal cameras and embedded thermo-couples. Fig. 13 shows the calibration components used by Williams et al. (2019) in L-PBF (top panel) and the one used by Rodriguez et al. (2015) in EB-PBF (bottom panel).

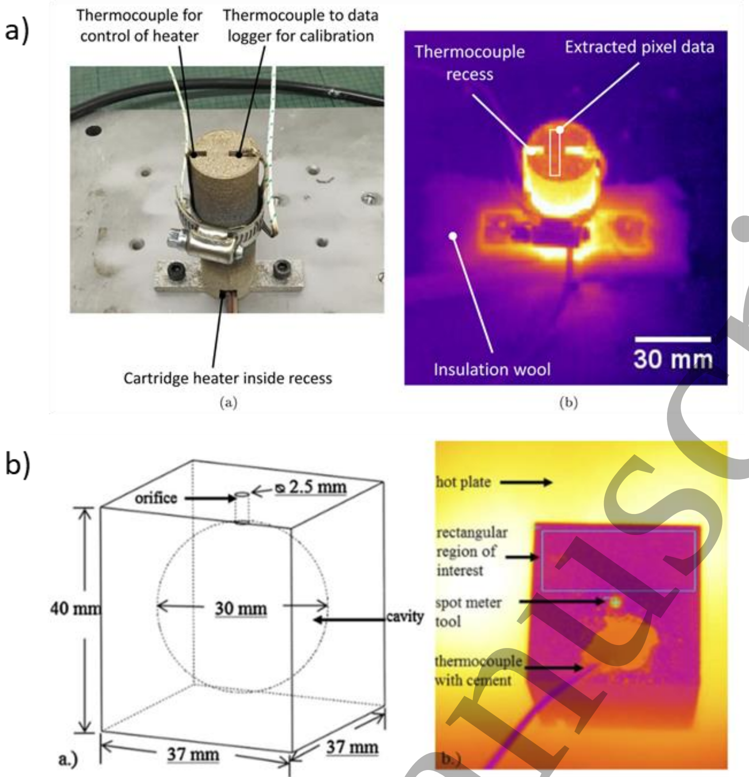

Figure 13. Examples of calibration components used in L-PBF (top panel) (Williams et al., 2019) and in EB-PBF (bottom panel) (Rodriguez et al., 2015) to enable true temperature estimation via in-situ IR video imaging

Thermal cameras are large in size, expensive and typically require a modification of the machine hardware and viewports for installation on industrial systems. Conventional cameras are much cheaper and easier to integrate than thermal cameras, and high temporal resolution can be made available with compact equipment. Although they do not allow actual temperature measurements, pixel intensity gradients in the visible range can be used as proxies for actual thermal gradients to identify anomalies and defects in some applications. In this framework, some studies focused on the detection of local over-heating phenomena known as “hot-spots” via high-speed video imaging in the visible range (Grasso et al. 2016, Colosimo and Grasso 2019, Yan et al. 2020). A hot-spot is a local over-heating of the layer caused by out-of-control heat exchanges with the surrounding material. A region affected by a hot-spot stays hot (bright) for a longer time with a slower cooling drift than in normal conditions. Because of this, a conventional camera with sufficient temporal resolution is suitable to capture the anomaly. High-speed vision in the visible range was also used in EB-PBF for hot-spot detection (Grasso et al. 2020) and to support the development of a novel scan strategy by monitoring the dynamics of the so-called “ghost beam” (Lee et al. 2018).

As a compromise between standard optical systems and thermal cameras, video-imaging in the NIR range (0.7 µm to ~1 µm) has been used by various researchers (Gong et al. 2013, Price et al. 2012, 2014, Boone et al. 2018). The main advantage is to filter out undesired effects at specific wavelengths and to reduce the dynamic range of the measurement with respect to that of optical video imaging. NIR video imaging for level 2 in-situ measurements has been used mainly in EB-PBF. The leaded glass used to shield X-ray emissions has a transmission larger than 90% in the NIR range, much higher than in the IR range (Boone et al. 2018).

3.3.2. Measurement of process by-products

Due to the different beam-material interactions in L-PBF and EB-PBF, different kinds of by-products are generated in the two processes. In L-PBF, spatters are ejected together with partial material vaporisation, also known as plume. Various researchers demonstrated the correlation between the information enclosed by such by-products and process states that can have detrimental effects on part quality (see Section 4). Different by-products are generated in EB-PBF, including secondary and backscattered electrons and X-rays, but, as shown in Section 2, they are more appropriate for level 1 in-situ measurements rather than for capturing fast transient phenomena during the electron beam scanning of the part. Therefore, this Section is devoted to methods applied to L-PBF only.

Intense by-products emissions can partially deflect and absorb the laser beam energy, or even deviate the laser focus position, leading to a modification in the laser beam geometry and the energy input. Spatters deposited on the powder bed may also produce contaminations in the part and discontinuities in the powder bed (Anwar and Pham 2018). Thus, unstable and out-of-control process by-product generation may have a detrimental effect on material properties. Fig. 14 depicts the plume emission and spatter ejection mechanisms in L-PBF, including droplet and hot powder spatters. The schematic example in Fig. 14 shows a forward plume emission, but, as shown by Bidare et al. (2018a), upwards and backwards plume emissions may occur, depending on process parameters.

Various studies in the literature demonstrated the possibility to gather information about spatter and plume salient properties via visible and IR video imaging methods. Table 5 summarises and classifies the literature in terms of sensing equipment and measurement specifications (wavelength range, spatial and temporal resolution).

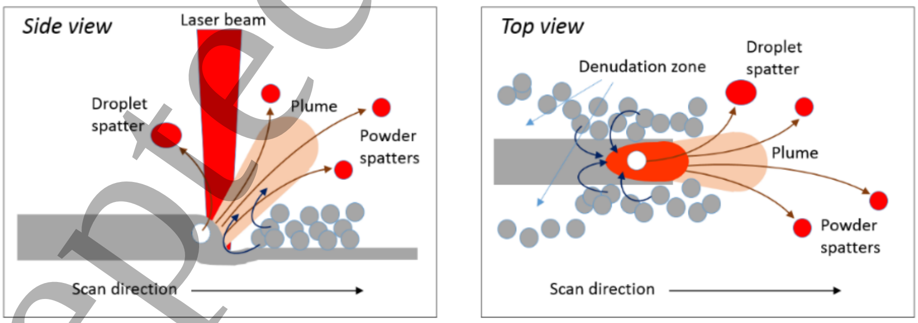

Figure 14. Schematic representation of spatters and plume emissions in L-PBF

Table 5 – Measurement wavelength range and spatial/temporal resolution of in-situ by-product measuring methods in L-PBF

Methods	Wavelength range	Spatial Resolution /μm/pixel	Temporal Resolution /Hz	References
Optical video imaging	Visible	11	3,000	Yang et al., 2020a
		-	2,000 – 24,000	Yang et al., 2020b; Ozel et al., 2018
		-	3,000	Tan et al., 2020
		3.92 – 5.70	100,000	Yin et al. 2020
		11.7	2,000	Zhang et al. 2019a, b
		-	37,500	Nassar et al., 2019
		1.5 – 11	8,000	Bidare et al., 2018a,b, 2017
		-	20,000	Zheng et al., 2018
		-	2,000	Zhang et al., 2018
		-	6,000	Andani et al., 2018, 2017
		250	1,000	Repossini et al., 2017
		5	100,000	Ly et al., 2017
		-	-	Liu et al., 2015
Optical stereo video imaging	Visible	40	60,000	Eschner et al., 2020a, 2019
		250	1,000	Barrett et al. 2019,
		18 – 24	1,000	Barrett et al. 2018a
NIR/IR video imaging	NIR	-	5,000	Ye et al., 2019, 2018a
	Long wave IR	-	50	Grasso and Colosimo, 2019; Grasso et al., 2018a
X-ray video imaging		-	45,259 – 135,776	Young et al. 2020
		6.6	5,100	Leung et al., 2019
		up to 1	54,310	Guo et al., 2018
		-	50,000	Zhao et al., 2017
Schlieren video imaging		-	16,000	Bidare et al., 2018a,b, 2017

Fig. 15 shows some examples from the in-situ measurement of process by-products.

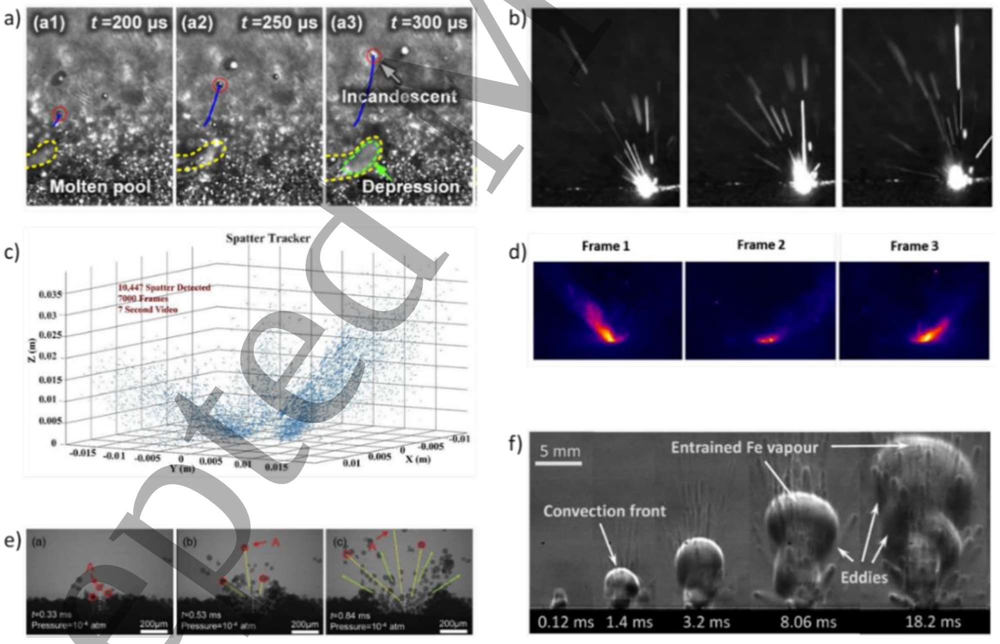

Figure 15. Examples from the in-situ measurement of process by-products in L-PBF: a) ultra high-speed video frames with cameras synchronised to a pulsed high-power diode laser light source (Yin et al., 2020); b) high speed video frames where only hotter objects are visible (Tan et al., 2020); c) 3D spatter localisation via high-speed stereo vision (Barrett er al., 2019); d) plume emissions captured with long wave IR video imaging (Grasso and Colosimo, 2019); e) high-speed X-ray video frames (Guo et al., 2018); f) Schieleren imaging video frames (Bidare et al., 2018a).

In most cases, focus was on the characterisation of the by-product ejection mechanism and the correlation of salient properties measured via high-speed video imaging (e.g, the number of spatters, their size, velocity, spread in space) with different process parameters. Recent studies proposed a high-speed stereo vision setup to identify and track individual spatters in the 3D space above the layer (Eschner et al. 2020a, 2019, Barrett et al. 2019, 2018a). Spatter tracking along its trajectory may improve the characterisation of process by-products and provide additional insights about their origination mechanism and the influence of process parameters (an example is shown in Fig. 15 c)). Eschner et al. (2019) used two ultrahigh-speed cameras combined with a particle detection matching and tracking algorithm, which allowed them to determine the 3D position and velocity of spatters. The same approach was used in a more recent study (Eschner et al. 2020a) to correlate spatter signatures with the penetration depth measured ex-situ and with the transition from heat conduction to evaporation dominating the process regime. Barrett et al. (2018a) demonstrated the use of low-cost, high-speed stereo vision methods on an industrial L-PBF machine (EOS M290).

Some researchers used pulsed high-power diode laser light sources (Yin et al. 2020) or tungsten filament lamps (Bidare et al., 2018a) to enable the visualization of both the weld track and the hot ejections from the melted area (as shown in Fig. 15 e)). High-speed videos, where only hot objects, i.e., spatters, plume and the laser heated zone, are bright enough to be observable, facilitate the image segmentation and feature extraction of process by-products detected as connected components (Fig. 15, b)). This was obtained by many other researchers without any external illumination (Zheng et al. 2020, Zhang et al. 2020, Ye et al. 2019, Repossini et al. 2017). In other cases, similar videos were recorded with external light sources to cope with limited sensor sensitivity or with too short integration times (e.g., Tan et al. 2020, Andani et al. 2018). Some authors (Grasso and Colosimo 2019, Grasso et al. 2018a) used an IR camera to monitor hot plume emissions in L-PBF (Fig. 15, d)).

For the characterisation of the spatter origination mechanism, various researchers used high-speed high-energy X-ray video imaging system (Young et al. 2020, Leung et al. 2019, Guo et al. 2018, Zhao et al. 2017). The laser scan path is typically limited to a single continuous scan perpendicular to the X-ray beam (Fig. 15, e)). The scan occurs on a powder bed held in place by two transparent side walls. Owing to this measurement setup, it is not only possible to observe spatter dynamics, but also the melt pool penetration depth and sub-surface porosity formation (see Section 3.5). Bidare et al. (2018a) combined high-speed video imaging with high-speed Schlieren video imaging, which allowed visualizing the gas flow and its interaction with the plume and ejected spatters (Fig. 15, f)).

3.3.3. Measurement of air-borne acoustic emissions

Air-borne acoustic emission sensors have already been used in laser welding applications (Ali and Farson 2002) and a few studies have tested this approach in L-PBF. The underlying principle consists of capturing air density variations during the laser scanning of the part by placing the sensor in the vicinity of the melted area. Therefore, the measured signature is related to the process by-product in terms of plume emissions and plasma formation.

In Wasmer et al. (2019) and Shevchik et al. (2019), the airborne acoustic emission signal was acquired by means of a fibre Bragg grating (FBG) optoacoustic sensor installed into the build chamber at about 200 mm from the process zone. In both studies, the sensor was installed on an industrial L-PBF machine and the sampling frequency was 1 MHz. The sensor was placed so that the longitudinal axis of the fibre was perpendicular to the acoustic wave to increase its sensitivity. In Ye et al. (2018b), instead, a microphone was installed into the build chamber at an angle of 30° above the build area, with a frequency response in the range 0 to 100 kHz. A similar approach was used in Kouprianoff et al. (2018). The resulting measurements and their information content in the temporal and/or frequency domain can be viewed as signatures of the laser-material interaction during the laser scanning of the part.

3.4 Level 3 methods – Melt-pool

The melt pool represents a fundamental source of information to understand the PBF process dynamics. In-situ measurements of the melt pool properties have been investigated only in L-PBF, although some EB-PBF level 2 methods, reviewed in Section 3.3, attempted to extract features at both track and melt pool level via off-axis video imaging. The significant advantage provided by L-PBF is the possibility of using the laser optical path in co-axial sensing mode. On this basis, the majority of the literature in this field relies on co-axial spatially integrated pyrometry measurements, co-axial spatially resolved video imaging methods or combinations of the two. The novelties presented in most recent studies are mainly related to the analysis of melt pool measurements via machine learning techniques. Nevertheless, a few studies proposed novel sensing solutions such as co-axial dual wavelength video imaging (Mitchell et al. 2020, Williams et al. 2019, Hooper et al. 2018) or co-axial optical emission spectroscopy (Lough et al. 2020a). Table 6 and Table 7 summarise and classify the literature in this field.

Table 6 – Summary and classification of level 3 methods in L-PBF

Signatures of interest	Sensing method	References (L-PBF)
Melt pool radiation intensity	Co-axial single wave pyrometry (spatially integrated)	Forien et al., 2020; Haines et al., 2020; Renken et al., 2019; Yang et al., 2019; Demir et al., 2018; Craeghs et al. 2011, Berumen et al. 2010, Chivel 2013, Clijsters et al. 2014, Doubenskaia et al., 2012, Pavlov et al. 2010, Thombansen et al. 2015
	Co-axial multi wave pyrometry (spatially integrated)	Jayasinghe et al., 2020; Okaro et al., 2019; Alberts et al., 2017
	Off-axis single wave pyrometry (spatially integrated)	Bisht et al., 2018; Nadipalli et al., 2019
Melt pool size and shape	Co-axial video imaging in the visible range	Zhirnov et al., 2020; Yang et al., 2019; Yuan et al., 2019; Demir et al., 2018; Kwon et al., 2018; Yuan et al., 2018; Craeghs et al. 2010, Craeghs et al. 2012, Clijsters et al. 2014, Berumen et al. 2010, Kruth et al. 2007
	Co-axial video imaging in the NIR range	Kolb et al., 2020; Vasileska et al., 2020; Forien et al., 2020; Lane and Yeung, 2019: Demir et al., 2019, 2018; Fisher et al., 2018; Kolb et al., 2018, 2018b; Fox et al., 2017
	Co-axial dual wave video imaging	Williams et al., 2019; Hooper, 2018
	Off-axis video imaging in the visible range	Scime and Beuth, 2019; Bruna-Rosso et al., 2018
	Off-axis NIR/IR video imaging	Lane et al., 2020; Heigel et al., 2020a,b
	Inline coherent imaging	Kanko et al., 2016
Melt pool temperature profile	Co-axial video imaging in the visible range	Doubenskaia et al. 2012; Berumen et al. 2010, Yadroitsev et al. 2014, Chivel 2013
	Off-axis dual wave video imaging	Mitchell et al., 2020
Melt pool emission spectrum	Co-axial optical emission spectroscopy	Lough et al., 2020a
Material cross-contamination	Co-axial single wave pyrometry	Montazeri et al., 2018

Table 7 – Wavelength ranges and spatial/temporal resolutions of in-situ melt pool measurements in L-PBF

Sensing method	Wavelength range /nm	Spatial Resolution /µm/pixel	Temporal Resolution /Hz	References (L-PBF)
Co-axial pyrometry (spatially integrated)	1500 – 1700	na	100,000	Forien et al., 2020
	1580 - 1800		10,000	Haines et al., 2020
	850 – 1000		100,000	Renken et al., 2019
	1000 – 2000		100,000	Yang et al., 2019
	350 – 1100		10,000	Montazeri et al., 2018
	1054 - 1074		100,000	Demir et al., 2018
	-		100,000	Thombansen et al. 2015
	780 – 950		10,000	Clijsters et al. 2014, Craeghs et al. 2011, Berumen et al. 2010
	900 – 1200		20,000	Chivel 2013, Doubenskaia et al., 2012, Pavlov et al. 2010
	700 – 1050, 1080 – 1700		100,000	Jayasinghe et al., 2020
	700 – 1050, 1100 – 1700		100,000	Okaro et al., 2019
	-		100,000	Alberts et al., 2017
Co-axial video imaging	Visible	-	2,500	Yang et al., 2019
		-	1,000	Yuan et al., 2019, 2018
		-	2,500	Kwon et al., 2018
		3.75	68	Demir et al. 2018
		20	20,000	Chivel 2013, Doubenskaia et al. 2012
	700 – 900	6.7	15,000	Kolb et al., 2020, 2018a, 2018b
	850 – 1000	14	1,200	Vasileska et al., 2020, Demir et al., 2019
	830 – 870	12	30,000	Fox et al., 2017
	780 – 820	17	1,000	Forien et al., 2020
	830 – 870	15	50,000	Fisher et al., 2018
	830 – 870	8	2,000	Lane and Yeung, 2019
	700 - 1100	2.2	68	Demir et al. 2018
	780 – 950	-	10,000	Clijsters et al. 2014, Craeghs et al. 2010, Craeghs et al. 2012, Berumen et al. 2010
	700, 950	20	50,000	Williams et al., 2019
	700, 950	-	100,000	Hooper, 2018
Co-axial inline coherent imaging	Centre wavelengths: 843 (setup1), 864 (setup2)		200,000	Kanko et al., 2016
Co-axial optical emission spectroscopy	400 – 700	na	14	Lough et al., 2020a
Off-axis pyrometry (spatially integrated)	1150 – 1800	na	50,000	Bisht et al., 2018
	1200 - 1800		100,000	Nadipalli et al., 2019
Off-axis video imaging	Visible	3.07	20,000	Zhirnov et al., 2020
	Short-wave IR	34 - 52	1,800	Heigel et al., 2020a,b
	Visible	6.2	6,400	Scime and Beuth, 2019
	630 – 650	-	50,000	Bruna-Rosso et al., 2018
	Short-wave IR	36	1,800	Lane et al., 2020
	830 – 870	3.28	10,000	Lane et al., 2020
	700, 900	21	6,000 – 7,000	Mitchell et al., 2020

Section 3.4.1. and Section 3.4.2. review spatially integrated and spatially resolved methods, respectively. The reader is also referred to Liu et al. (2020c) for a review of patents devoted to melt pool temperature monitoring.

3.4.1. Spatially integrated methods

In-situ co-axial measurements of melt pool properties represented the core of research in L-PBF process monitoring in the first published studies (between 2010 and 2015, and in a few cases earlier). The melt pool properties of interest include the melt pool size or geometry, the intensity and spectrum of emitted radiation, etc.

Spatially integrated pyrometry, by means of one or multiple photodiodes, is suitable to measure melt pool radiation intensity with high temporal resolution. Table 7 shows that, in almost all recent studies, a sampling rate of 100 kHz was used. Among the most important factors affecting the quality of the measured data, the measurement wavelength range and the sensor field of view play a central role. In all the studies reported in Table 7, the wavelength range was slightly above or below 1000 nm, whereas some researchers used dual-wavelength measurements in the ranges 700 nm to 1050 nm and 1100 nm to 1700 nm (Jayasinghe et al. 2020, Okaro et al. 2019, Alberts et al. 2017). Measuring melt pool radiation above 1000 nm was prevented, in some cases, by the optical chain (Clijster et al. 2014), but this limit was overcome in other studies (e.g., Forien et al. 2019 and Yang et al. 2019). Co-axial photodiodes are nowadays available in most industrial L-PBF systems, and, in most cases, a 2D map of melt pool intensities is provided by synchronising the photodiode signal with the laser spot coordinates. A different use of a co-axial photodiode was discussed in Montazeri et al. (2018), where the authors showed that the chemical composition of the material can be determined via melt pool radiation measurement, leading to possible material cross-contamination detection. In this case, the detection range of the sensor was 350 nm to 1100 nm, with the aim of measuring the radiation intensity of the plume.

Some researchers proposed in-situ melt pool measurement methods relying on off-axis mounted photodiodes. For example, Nadipalli et al. (2019) and Bisht et al. (2018) used an analogous approach for melt pool intensity measurements during the production of tensile specimens. The field of view of the sensor covered the entire build area, which enabled the collection of not only melt pool radiation signals, but also radiation emitted by surrounding hot areas and by-product emissions. Due to this, the characterisation of melt pool properties is limited and imprecise, compared to co-axial methods. Instead of measuring the integrated radiation intensity emitted by the melt pool, Lough et al. (2020a) used a co-axial optical emission spectroscopy approach to measure the spectral content of the collected radiation and determine the chemistry and relative intensities of the excited species vaporised within the plume. To this aim, the measurement spectral range was 400 nm to 700 nm.

3.4.2. Spatially resolved methods

Richer information about melt pool properties and stability over time can be gathered via co-axial video imaging methods, and several studies proposed this approach. As shown in Table 7, in most cases, a high-speed camera (with sampling rate between 1000 fps and 50,000 fps) equipped with a narrow-band NIR filter was used to enhance the dynamic range and capture predominant melt pool emissions at the melting temperature. It is worth noting that the literature on in-situ monitoring of melt pool properties lack any method based on co-axial IR video imaging.

Some researchers used off-axis video imaging methods for melt pool measurements. This approach was made feasible by using high-magnification optics combined with a limited field of view. Zhirnov et al. (2020) and Lane et al. (2020) used an off-axis high-speed camera combined with a mirror that allowed close-range observation of the melt pool without obstructing the laser, achieving a spatial resolution in the order of 3 μm/pixel. Lane et al.

(2020) also used an off-axis thermal camera for melt pool thermography at lower resolution (36 µm/pixel). Similarly, Heigel et al. (2020a,b) used an off-axis IR camera for melt pool length and cooling rate estimations, whereas Scime and Beuth (2020) and Bruna-Rosso et al. (2018) used off-axis mounted high-speed cameras in the visible range to study the morphology of the melt-pool and its variation along the track.

Only a few researchers reported calibration procedures for melt pool video imaging analysis. Lane et al. (2020) calibrated their off-axial high-speed camera, equipped with a NIR filter, by using a light emitting diode-driven integrating sphere, leading to a non-linear calibration curve between blackbody temperature and camera signal. A different approach was adopted by other researchers who proposed the use of dual wavelength video imaging, i.e., the acquisition of video image streams at two different wavelengths (700 nm and 950 nm) to enable a temperature estimate via two-colour thermography (Williams et al. 2019, Hooper et al. 2018, Mitchell et al. 2020). The method allows the avoidance of the difficulties related to melt pool emissivity estimation by calculating the ratio of the radiances measured at the two separate wavelengths, under the assumption of a constant emissivity at these wavelengths. Fig. 16 shows some examples of melt pool images and melt pool surface temperature estimations.

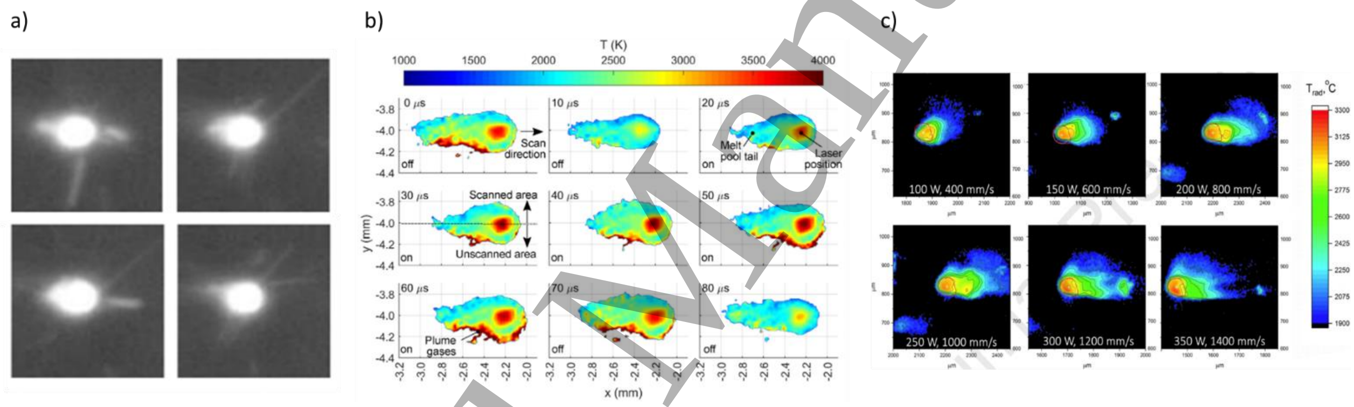

Figure 16. a) Co-axial melt pool images in four sequential video frames in the visible range (Yuan et al., 2019), b) melt pool surface temperature estimation via dual wavelength co-axial video imaging (Hooper et al., 2018), c) melt pool surface temperature estimation via off-axis video imaging for different process parameters (Zhirnov et al., 2020)

A different spatially resolved approach was used by Kanko et al. (2016). They used a co-axial in-line coherent imaging method, analogous to that introduced in Section 3.2, to measure the melt pool and surrounding area morphology changes. The in-line coherent imaging approach enabled a local reconstruction of the height profile within the melt pool and along the track. This approach has been applied to single tracks only, but it could be extended, in principle, to three-dimensional builds.

3.5 *Level 4 methods – under the layer*

All the in-situ sensing and measurement methods presented in the previous Sections, classified from level 0 to level 3, involve a measurement of the patterns and phenomena that occur in the layer in the process of production, either before, during or after the melting phase. However, as the next layer is being printed, the material characteristics underneath are modified as well, due to the partial remelting of top layers and heat exchanges within the build volume. Some in-situ sensing and measurement methods have been proposed to go beyond the layerwise paradigm, aiming at gathering information about what goes on under the current layer. Table 8 and 9 summarise and classify these methods. One stream of research regards the use of high-speed high-energy X-ray imaging systems to observe subsurface melt pool dynamics, the penetration depth and pore formation. Other researchers investigated the use of a similar sensing setup for X-ray diffraction measurement, which allows the characterisation of strain and stress formation and phase transformations (Schmeiser et al. 2020, Uhlmanna et al. 2017, Calta et al. 2018, Zhao et al. 2017). One study also explored the feasibility of in-situ micro-tomography (Lhuissier et al. 2020). A second mainstream of research regards the use of acoustic emissions to gather information about elastic energy releases under the layer, such as cracks and delamination. A few researchers also studied in-situ measurements of the baseplate (Herh et al. 2020, Dunbar et al. 2016). All these methods have been applied only in L-PBF so far.

Table 8 – Classification of the literature devoted to level 4 methods

Signatures of interest	Sensing method	References (L-PBF)
Subsurface melt pool dynamics	X-ray video imaging	Young et al. 2020; Paulson et al., 2020; Calta et al., 2020; Guo et al., 2020; Leung et al., 2019; Martin et al., 2019; Bobel et al., 2019; Guo et al., 2019; Guo et al., 2018; Leung et al., 2018; Calta et al., 2018; Zhao et al., 2017
Volumetric reconstruction	X-ray micro-tomography	Lhuissier et al., 2020
Phase transformation, strain and stress formation	X-ray diffraction	Schmeiser et al. 2020; Uhlmann et al., 2017; Calta et al., 2018; Zhao et al., 2017
Acoustic emissions	Structure-borne acoustic emission detection	Eschner et al. 2020b; Plotnikov et al. 2019; Rieder et al., 2016; Rieder et al., 2014
Baseplate deformation	Strain gauge	Hehr et al., 2020; Dunbar et al., 2016

Table 9 – Measurement performances for level 4 methods in L-PBF

Methods	Frequency band /kHz	Spatial Resolution /µm/pixel	Temporal Resolution /Hz	References (L-PBF)
X-ray video imaging		-	45,259 – 135,776	Young et al. 2020
		1.97	30,000	Paulson et al., 2020
		-	-	Calta et al., 2020
		1.97	140,000	Guo et al., 2020
		6.6	5,100	Leung et al., 2019
		1	500,000	Martin et al., 2019
		1.974	50,000	Bobel et al., 2019
		2	45,000	Guo et al., 2019
		1.1	4,000	Calta et al. 2018
		up to 1	54,310	Guo et al., 2018
		-	50,000	Zhao et al., 2017
X-ray micro-tomography		3.64		Lhuissier et al., 2020
X-ray diffraction		na	10,000	Schmeiser et al. 2020
			-	Uhlmann et al., 2017
			1,000	Calta et al., 2018
			-	Zhao et al., 2017
Structure-borne acoustic emission	0 – 2,000	na	4,000,000	Eschner et al. 2020b
	>100		1,000,000	Plotnikov et al. 2019
	400 – 30,000		250,000,000	Rieder et al., 2016, 2014
Baseplate deformation		na	20	Hehr et al., 2020
			-	Dunbar et al., 2016

X-ray video imaging methods were introduced in Section 3.3. Although they can provide insights about the origination mechanism of process by-products, their main use regards the capability of observing the melt-pool cross-section in a plane perpendicular to the layer. Fig. 17 shows an example of the apparatus used in Guo et al. (2019) and an example of an in-situ X-ray video frame (Paulson et al. 2020). The high-energy X-ray beam penetrates the material along a direction orthogonal to both the scan and build directions. Laser scanning is performed along a narrow powder bed, spread between two transparent walls (usually glassy carbon sheets). A downstream detection system converts the X-ray signal into visible light by means of a scintillator, and the converted signal is finally recorded by a high-speed camera.

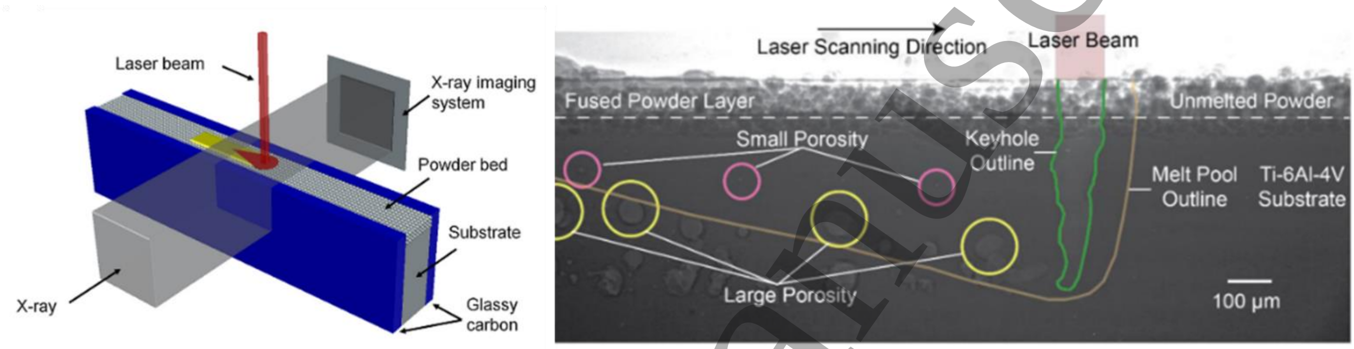

Figure 17. Scheme of the apparatus for in-situ X-ray video imaging in L-PBF (left) (Guo et al., 2019) and an example of an in-situ X-ray video frame (right) (Paulson et al., 2020)

Fig. 17 shows that X-ray imaging for in-situ measurements can be used only at laboratory level using ad-hoc L-PBF prototype systems. Despite not being applicable on production machines for industrial use, this approach turned out to be convenient to reveal complex dynamical changes in the melt pool and depression zones during laser scanning. This is enabled by the capability to look under the layer and by the very high spatial and temporal resolutions that can be achieved with this method. Table 9 shows that a spatial resolution of 1 μm/pixel to 2 μm/pixel can be achieved, with a sampling rate higher than 100,000 fps. Calta et al. (2018) and Zhao et al. (2017) combined in-situ X-ray video imaging with in-situ X-ray diffraction to observe not only subsurface melt pool dynamics but also phase transformations in the material and changes in the strain and stress states. In these studies, two different detectors were used for X-ray imaging and X-ray diffraction. In-situ X-ray diffraction was also studied in Schmeiser et al. (2020) and Uhlmann et al. (2017). A completely different configuration was proposed by Lhuissier et al. (2020), where the aim was to demonstrate the feasibility of in-situ X-ray micro-tomography for the volumetric reconstruction of the part during the process. Fig. 18 (top panel) schematically shows how the apparatus presented by Lhuissier et al. (2020) operates. Fig. 18 (bottom panel) shows the resulting 3D reconstruction of a wall measured at different consecutive layers (the 3D volume reconstruction was post-processed to remove particles of the powder bed and visualise the bulk wall).

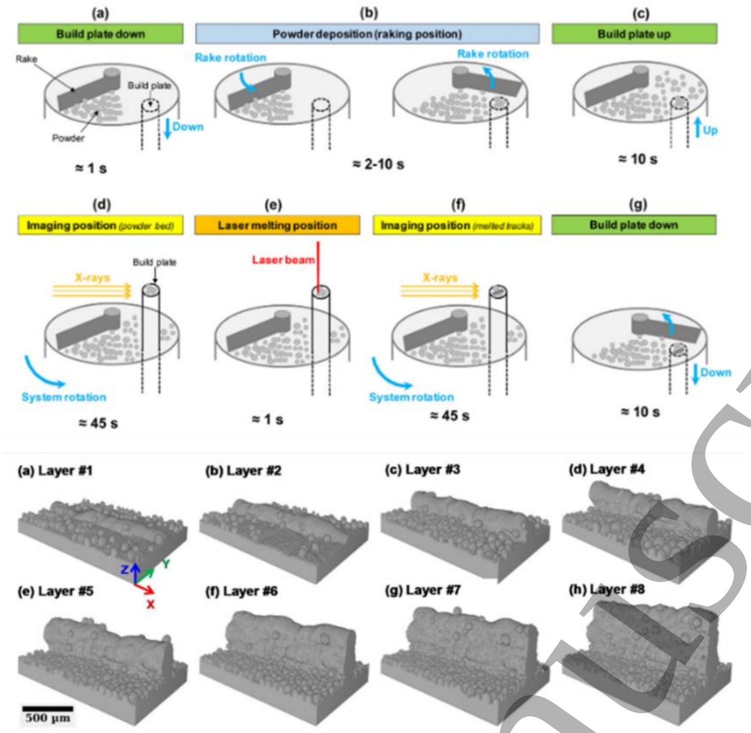

Figure 18- Schematic representation of the working principle of the in-situ X-ray micro-tomography approach presented by Lhuissier et al. (2020) (top panels); in-situ 3D reconstruction of a wall measured at different consecutive layers (powder bed particles were removed in 3D data post-processing to visualise the bulk wall)

In Lhuissier et al. (2020), during the in-situ microtomography scan, 1500 projections were acquired resulting in a scan time of 45 s. The measurements presented in Lhuissier et al. (2020) were gathered with a spatial resolution of 3.64 μm/pixel and a field of view of (8.8 × 6.2) mm.

A different field of research with more direct application potentials in industry regards the in-situ measurements of acoustic emissions. As mentioned in Section 3.3, acoustic emissions can be divided into air-borne and structure-borne emissions. The latter are suitable to detect sudden releases of elastic energy that propagate within the material. This enables the possibility to detect crack formations, detachments of overhang areas from supports or delamination phenomena. The use of multiple sensors placed at different locations could also provide information about the location within the build where the energy release originated. The structure-borne signal is also influenced by other laser-material interactions and hence they can provide additional insights about changes in process conditions. The use of structure-borne acoustic emission sensors has been proposed by various authors since the first seminal works of Rieder et al. (2014 and 2016) and patented by some major L-PBF system developers (Gold and Spears 2018, Northeast et al. 2018, Scott and Sutcliff 2015). Rieder et al. (2014, 2016) proposed an ultrasonic monitoring device in L-PBF mounted on the underside of the baseplate focusing on the bottom plate interface echo and the backwall echo patterns as proxies of discontinuities in the material, while the specimen build-up height increased. More recently, a similar approach was presented in Eschner et al. (2020b) but the spectrogram of the signal was used to characterise the acoustic emission signature of the process rather than the recorder echo. Plotnikov et al. (2019), instead, monitored the RMS of the signal.

Finally, a couple of studies presented methods for baseplate distortion measurements during the process. In Dunbar et al. (2016), a displacement sensor was attached to the underside of the baseplate. A more recent study (Hehr et al. 2020) presented a smart baseplate for L-PBF with an embedded optical fibre strain measurement sensor. Rather than measuring the baseplate deformation, Hehr et al. (2020) demonstrated the feasibility of the proposed approach to detect plastic deformations like a delamination from the baseplate.

4 In-situ monitoring and in-situ defect detectability

Section 3 presented a review of the in-situ methods used to measure the most relevant process signatures while a product is being built. This section is devoted, instead, to in-situ monitoring methods, i.e., to the capability of signalling process anomalies that could indicate the onset of defects in the part or undesired changes in the process. For the design of in-situ monitoring methods, two types of correlation could be investigated. The first regards the influence of input variables and controllable factors on in-situ measured quantities, including powder properties, process parameters, part and build geometry and chamber atmosphere. The second type of correlation regards the correspondence between events and anomalies detected during the process and the final quality and performance of the manufactured part. Studies belonging to this second category can be divided into two main classes, one focused on the quality of single tracks or single layers, and one exploring the final properties of three-dimensional parts, including their microstructure, porosity, geometrical errors, residual stresses, cracks, etc.

Table 10 classifies the studies that linked in-situ measured quantities to input controllable factors (left side) and major output quality characteristics (right side). Studies that investigated other types of defects (residual stresses, cracks and delamination) are reviewed in Section 4.2.5. Table 10 (right side) shows that most authors varied salient process parameters to force the occurrence of flaws in the part. Other studies focused on the effect of geometrical features, whereas only few authors addressed other sources of variability, i.e., the variability of either metal powder properties or chamber atmospheric conditions.

Table 10 (right side) shows that about 30% of studies that investigated the link between in-situ measured quantities and the final quality of manufactured parts involved single track (or single layer) experiments. Although the analysis of individual track properties is not sufficient to demonstrate actual in-situ defect detection capabilities in three-dimensional parts, it provides relevant information about defect onset mechanisms and the suitability of process signatures to identify variations in the process state. The remaining portion of studies showed on the right side of table 10 was devoted mainly to the in-situ detection of local porosities or the distinction between different density levels, whereas various authors investigated also the capability of predicting the final microstructural properties of the part or detecting possible geometrical distortions, and/or the correlation between process signatures and mechanical properties. Section 4.1 briefly summarises major insights about the link between all these input variables and in-situ process signatures. Section 4.2 reviews the literature in this framework.

Table 10 – Mapping of studies that linked in-situ measured quantities to input controllable factors (left side) and to output quality characteristics (right side) in L-PBF and EB-PBF (references of methods in EB-PBF are shown with italic font) – part 1: levels 0, 1 and 2

Input				**In-situ signals**			**Output**				
							Single track/ single layer quality	**3D part quality**			
Powder	**Process parameters**	**Part/build geometry**	**Chamber atmosphere**		**Signatures of interest**	**Sensing method**		**Microstructure**	**Porosity/ density**	**Geometrical distortions**	**Mechanical properties**
Chandrasekar et al., 2020				Level 0						*Grasso et al., 2018*	
	Lu et al., 2020; Aminzadeh and Kurfess, 2019; Imani et al., 2019a; Lu et al., 2019	Scime et al., 2020; Scime and Beuth, 2018a,b		Level 1	Surface pattern or height map of the printed slice	Off-axis imaging in visible range			Lu et al., 2020; Imani et al., 2019a,b; Gobert et al., 2018; Lu et al., 2019; Abdelrahman et al., 2017	Scime et al., 2020; Scime and Beuth, 2018a,b	Lu et al., 2019
Nandwana et al., 2018		*Yoder et al., 2019, 2018;*				Off-axis NIR/IR imaging			Mahmoudi et al., 2019; *Yoder et al., 2019;*		*Yoder et al., 2019*
						Blade-mounted sensor			Barrett et al., 2018b		
	Fleming et al., 2020; Depond et al., 2018	Depond et al., 2018				Inline coherent imaging					
	Pobel et al., 2019; Arnold et al., 2019, 2018					Electronic imaging			*Arnold et al., 2018*		
		Pagani et al., 2020; Zur Jacobsmuhlen et al., 2019; Caltanissetta et al., 2018; Gaikwad et al., 2019;			Geometry of the printed slice	Off-axis imaging in visible range				Pagani et al., 2020; Gaikwad et al., 2019	
		Yan et al., 2020; Colosimo and Grasso, 2018; Grasso et al., 2017		Level 2	Heatmap / heating and cooling profiles	Off-axis video-imaging in the visible range		*Lee et al., 2018*		Yan et al., 2020; Colosimo and Grasso, 2018; Grasso et al., 2017	
	Mohr et al., 2020; Lough et al., 2020b, 2019; Paulson et al. 2020; Jalalahmadi et al., 2019; Plotnikov et al., 2019; Foster et al., 2018; Bartlett et al. 2018; Alldredge et al., 2018; *Cordero et al., 2017; Raplee et al., 2017; Dehoff et al. 2019*	Heigel et al., 2020a,b; Mohr et al., 2020; Gaikwad et al., 2020; Williams et al., 2019; Elwarfalli et al., 2019; Montazeri and Rao, 2018; *Boone et al. 2018*				Off-axis NIR/IR video imaging		Foster et al., 2018; Williams et al., 2019; *Raplee et al., 2017; Dehoff et al., 2019*	Mohr et al., 2020; Lough et al., 2020b, 2019; Paulson et al. 2020; Jalalahmadi et al., 2019; Bartlett et al., 2018; Williams et al., 2019; Foster et al., 2018	*Boone et al. 2018*	Williams et al., 2019; Lough et al., 2020b;
	Montazeri et al., 2020; Dunbar and Nassar, 2018; *Cordero et al., 2017;*					Off-axis multispectral pyrometry			Montazeri et al., 2020		
	Yang et al., 2020a; Tan et al., 2020; Yin et al., 2020; Zhang et al., 2019a, b; Zheng et al., 2018; Zhang et al., 2018; Bidare et al., 2018a; Ye et al., 2019, 2018; Andani et al., 2018, 2017; Repossini et al., 2017; Ly et al. 2017		Bidare et al., 2018b		Process by-products	Off-axis video imaging in the visible range	Yin et al. 2020; Zhang et al., 2019a, b; Zheng et al., 2018; Zhang et al., 2018; Ye et al., 2019, 2018a;		Andani et al., 2018; Repossini et al., 2017		
	Eschner et al., 2020a					Off-axis stereo vision in the visible range					
	Grasso et al., 2018a; Grasso and Colosimo, 2019					Off-axis NIR/IR video imaging				Grasso et al., 2018a; Grasso and Colosimo, 2019	
Leung et al., 2019	Young et al., 2020; Zhao et al., 2017		Young et al., 2020; Guo et al. 2018			Off-axis X-ray video imaging					
	Wasmer et al., 2019; Shevchik et al., 2019; Ye et al. 2018; Kouprianoff et al., 2018				Air-borne acoustic emissions	Air-borne acoustic emission detector	Ye et al., 2018b; Kouprianoff et al., 2018		Wasmer et al., 2019; Shevchik et al., 2019		

Table 10 – Mapping of studies that linked in-situ measured quantities to input controllable factors (left side) and to output quality characteristics (right side) in L-PBF and EB-PBF (references of methods in EB-PBF are shown with italic font) – part 2: levels 3 and 4

Input				**In-situ signals**			**Output**				
								3D part quality			
Powder	**Process parameters**	**Part/build geometry**	**Chamber atmosphere**	**Signatures of interest**		**Sensing method**	**Single track/ single layer quality**	**Microstructure**	**Porosity/ density**	**Geometrical distortions**	**Mechanical properties**
	Forien et al., 2020; Renken et al., 2019; Yang et al., 2019; Demir et al. 2018	Renken et al., 2019	Haines et al., 2020	Level 3	Melt pool radiation intensity	Co-axial single wave pyrometry (spatially integrated)	Forien et al., 2020				
	Jayasinghe et al., 2020; Alberts and al., 2017;					Co-axial multi wave pyrometry (spatially integrated)			Jayasinghe et al., 2020; Alberts and al., 2017;		Okaro et al., 2019
	Nadipalli et al., 2019		Bisht et al., 2018			Off-axis single wave pyrometry (spatially integrated)	Nadipalli et al., 2019				Bisht et al., 2018
	Zhirnov et al., 2020; Kwon et al. 2020; Yuan et al., 2019, 2018; Yang et al., 2019; Demir et al., 2018				Melt pool size and shape	Co-axial video imaging in the visible range	Yuan et al. 2019, 2018		Kwon et al. 2020;		
	Kolb et al., 2020, 2018a, 2018b; Vasileska et al., 2020; Forien et al., 2020; Lane and Yeung, 2019; Demir et al., 2019, 2018; Fisher et al., 2018	Kolb et al., 2018b; Vasileska et al., 2020; Demir et al. 2019	Kolb et al., 2018b			Co-axial video imaging in the NIR range	Kolb et al., 2020; Forien et al., 2020; Fox et al., 2017		Kolb et al., 2018b	Kolb et al., 2018b; Vasileska et al., 2020;	
	Lane et al., 2020					Off-axis NIR/IR video imaging	Lane et al., 2020				
		Hooper, 2018				Co-axial dual wave video-imaging					
	Scime and Beuth, 2019; Bruna-Rosso et al., 2018	Scime and Beuth, 2019				Off-axis video imaging in the visible range					
		Heigel et al., 2020a,b				Off-axis NIR/IR video imaging					
					Melt pool temperature profile	Off-axis dual wavelength video imaging			Mitchell et al., 2020		
	Lough et al., 2020a		Lough et al., 2020a		Melt pool emission spectrum	Co-axial optical emission spectroscopy	Lough et al., 2020a				
Leung et al., 2019	Guo et al., 2020, 2019; Zhao et al., 2017; Calta et al., 2020; Martin et al., 2019; Bobel et al., 2019; Leung et al. 2018		Calta et al., 2020; Guo et al. 2018, Martin et al., 2019	Level 4	Subsurface melt pool dynamics	X-ray video imaging	Calta et al., 2020; Bobel et al. 2019				
					Volumetric reconstruction	X-ray micro-tomography			Lhuissier et al., 2020		
	Eschner et al., 2020b; Plotnikov et al. 2019	Eschner et al., 2020b;			Acoustic emissions	Structure-borne acoustic emission detection			Eschner et al., 2020b		

4.1 *Influence of input variables on in-situ signals*

4.1.1 Influence of process parameters

Varying process parameters and scan strategies represents the most common way adopted by researchers to force a variation of the final quality and functional properties of the part and observe consequent anomaly and defect onset mechanisms through in-situ measurement of process signatures.

Various authors showed that different energy density levels in L-PBF generate different surface topographies of each printed slice (Lu et al. 2020, Aminzadeh and Kurfess 2019, Imani et al. 2019a,b, Lu et al. 2019, Fleming et al. 2020, Depond et al. 2018). Deviations from a uniform and smooth surface were shown both at low energy density (resulting in irregular and porous patterns or even balling effects in more severe cases) and high energy density (resulting in uneven surfaces and superelevated edges). Similar effects have been studied in EB-PBF too (Pobel et al. 2020, Arnold et al. 2019, 2018). An irregular surface topography is more likely to generate defects in the part, but it is not a sufficient condition, because partial remelting in following layers may mitigate or even avoid the onset of defects in the part (see Section 4.2 for more details).

Many authors tested different sets of process parameters both in L-PBF and EB-PBF to investigate variations in the thermal history of the process measured in-situ via NIR or IR video imaging and pyrometry. In L-PBF, a variation of the energy density was shown to cause not only an increase of average and peak IR intensities (Foster et al. 2018), but also the occurrence of local outlying temperatures (Bartlett et al. 2018), a variations of the time a pixel temperature stays above a given threshold (Mohr et al. 2020, Lough et al. 2020b), a modification of cooling profile patterns (Paulson et al. 2020) and a shift in emission spectral characteristics associated to specific chemical elements (Montazeri et al. 2020). In EB-PBF, attention has been devoted to the effect of different process parameters on the temporal evolution of the average temperature of the layer (Cordero et al. 2017), and to temporal and spatial thermal gradients in different locations of the part passing from line to point scan strategies (Raplee et al. 2017; Dehoff et al. 2019).

Various authors showed that an excessive energy input to the material causes large and unstable plume emissions with a large amount of spatters characterized by high speed and spreading at large distances from the melting area (Yang et al. 2020, Zhang et al. 2019b, Zheng et al. 2018, Bidare et al. 2018a, Grasso et al. 2018a, Repossini et al. 2017). In such process state, a more likely generation of large droplet spatters ejected from the melt pool was observed too (Yang et al. 2020, Zhang et al. 2019b). Some authors also reported an increase of the backward ejection angle of spatters as the laser power increases (Yin et al. 2020, Zheng et al. 2018), although the orientation of spatter ejections can range from forward to backward depending on the combination of laser power and scan speed (Bidare et al., 2018a). In the presence of an insufficient energy input causing lack-of-fusion defects or balling irregularities along the tracks, low plume and spatter emissions were observed (Yang et al. 2020, Zhang et al. 2019b, Zheng et al. 2018, Bidare et al. 2018a, Repossini et al. 2017). Moreover, the effect of varying either the laser power or the scan speed may be different even if the energy density is the same (Ye et al. 2019).

In-situ X-ray video imaging confirmed aforementioned results and enabled more in depth insights about the by-product properties and origination mechanisms (Young et al. 2020, Leung et al. 2018, Zhao et al. 2017). Young et al. (2020) also showed the generation mechanism of powder agglomeration spatters (formed through coalescing of multiple powder particles and spatters) and so-called “defect induced spatters”. The latter were observed in correspondence of large pores within previously built layers: the interaction between the melt pool and the depression zone with the localized pore under the surface was shown to cause a sudden eruption out of the melt pool with a consequent liquid material ejection. All the aforementioned studies investigated the spatter generation in single laser L-PBF. Andani et al. (2018) studied process by-products in multi-laser L-PBF, showing that when multiple lasers work simultaneously in the same area a larger number of spatters is produced and their area is larger than the one observed when a single laser beam is used.

A large number of studies has been devoted to the effect of different process parameters on melt pool properties. An increase of the energy input to the material was shown to cause an increase of the melt pool thermal emission, the size and peak radiance of melt pool temperature isotherms, melt pool area, lengths and width (Forien et al. 2020, Zhirnov et al. 2020, Kwon et al. 2020, Kolb et al. 2020, Yuan et al. 2018, Alberts et al. 2017). The amplitude of co-axial pyrometer signals could be used to identify transitions between conduction and key hole mode laser processing conditions (Forien et al. 2020). The analysis of the melt pool shape and size at different energy densities enabled additional insights about stable and unstable process conditions and variations along the scan track, turning point effects and other dynamics related to the complex flow of molten material (Zhao et al. 2017). Other authors investigated the effect of continuous and pulsed modes on melt pool properties (Nadipalli et al. 2019, Vasileska et al. 2020, Demir et al. 2019). Vasileska et al. (2020) showed the melt pool area increase as a consequence of the increase of duty cycle in pulsed mode, whereas Demir et al. (2019) showed the feasibility of assigning different emission types in different regions of the same part to keep the melt pool size stable during the entire process. Demir et al. (2019) also showed that the energy density is not sufficient to describe the melting behaviour, as under the same energy density continuous and pulsed mode emission regimes resulted in different melt pool dimensions. Kolb et al. (2020, 2018a,b) showed that the melt pool properties are affected also by the surface roughness of the consolidated material beneath the current layer. The salient mechanisms of laser-material interactions, convective motions, penetration depth variation, powder consolidation and pore formation for different sets of process parameters were highlighted in depth via in-situ X-ray video imaging (Martin et al. 2019, Bobel et al. 2019, Leung et al. 2018).

Eventually, both air-borne and structure-borne acoustic emissions were shown to be affected by process parameters. Wasmer et al. (2019) and Shevchik et al. (2019) showed that different scan speeds caused different wavelet spectrograms patterns of the air-borne acoustic signal. The influence of process parameters on time and frequency domain features of the air-borne signal were discussed by Ye et al. (2018b) and Kouprianoff et al. (2018), whereas Eschner et al. (2020b) and Plotnikov et al. (2019) showed similar effects on structure-borne acoustic signals too.

4.1.2 Other influences: part and build geometry, powder properties and chamber atmosphere

Various authors used specimens with different geometries and complex parts with layerwise varying shape to study the variability of surface patterns and presence of anomalies within the printed slice (Scime et al. 2020, Scime and Beuth 2018a,b, Depond et al. 2018, Yoder et al. 2019, 2018) and the accuracy and feasibility of in-situ monitoring methods based on layerwise geometry reconstruction (Pagani et al. 2020; Zur Jacobsmuhlen et al. 2019; Caltanissetta et al. 2018, Gaikwad et al. 2019). Complex geometries including critical geometrical features like overhang surfaces, acute corners and thin walls were used as benchmark to force the onset of defects related to anomalous heat exchanges and thermal histories (Mohr et al. 2020, Yan et al. 2020, Colosimo and Grasso 2018, Grasso et al. 2017, Boone et al. 2018) or to investigate the influence on melt pool properties (Vasileska et al. 2020, Kolb et al., 2018b, Demir et al., 2019). Grasso et al. (2017) and following studies from the same authors (Yan et al. 2020, Colosimo and Grasso 2018) used a complex star-shaped part to force the onset of anomalous heat accumulations, i.e., hot-spots, which represent critical events in PBF as potential sources of micro and macro geometrical defects. Other authors used specimens including overhang areas with different angles and aspect ratios to force the occurrence of volumetric defects (Mohr et al. 2020) or geometrical errors (Boone et al. 2018, Kolb et al. 2018b), to investigate the effect on the thermal history of the process (Gaikwad et al. 2020, Montazeri and Rao 2018), the properties of the melt pool (Hooper 2018, Scime and Beuth 2019) and the time-frequency signature of structure-borne acoustic emissions (Eschner et al. 2020b). Rather than varying the shape of individual parts, Williams et al. (2019) investigated the influence of different inter-layer cooling time by varying the number of parts printed at different heights within the build.

Additional factors that have a direct and important effect on the stability of the process and the quality of the product regards the powder properties and the chamber atmosphere conditions. Nevertheless, only few authors investigated their impact on in-situ measured quantities. In EB-PBF, Chandrasekar et al. (2020) used log-signals associated the powder recoating operation to study the effect of powder recycling on its spreadability, showing that log-signals could provide relevant in-situ information about the powder particle behaviour. Nandwana et al. (2018), instead, studied the effect of powders from different suppliers on detected anomalies in layerwise NIR images. In L-PBF, Leung et al. (2019) investigated the effect of powder oxidation on melt pool and spatter dynamics through in-situ X-ray video imaging. The results showed that the oxygen content from the oxidised powder could alter the surface tension of the melt pool and the convection flows, with oxides acting as potential nucleation sites for pore formation. Oxidised powders also caused larger amount of ejected spatters. Leung et al. (2019) showed that partial laser re-melting when the next layers are processed may disrupt the oxide layer within previously melted tracks, enabling gas pores to escape, reducing the size of pre-existing pores or modifying their shape from spherical to irregular when they are partially filled by liquid material.

In L-PBF, Young et al. (2020) and Guo et al. (2018) studied the effects of chamber atmosphere conditions on process by-products, whereas Bisht et al. (2018), Kolb et al. (2018b), Lough et al. (2020a), Calta et al. (2020), Guo et al. (2018) and Martin et al. (2019) studied the effect of atmosphere conditions on melt pool dynamics. Young et al. (2020) and Guo et al. (2018) showed that by reducing the ambient pressure down to vacuum conditions the amount of cold powder spatters was increased whereas the amount of hot powder spatters entrained by the hot metal vaporization was reduced since the entrainment effects requires a sufficient gas flow. Lough et al. (2020a) also showed that increasing the ambient pressure inflates the plume-laser interactions and a consequent attenuation and defocusing of the laser beam, leading to shallower and wider melt pools. Calta et al. (2020) showed that the effect of the ambient pressure on melt pool process by-products dynamics may be different from material to material because of different boiling temperatures at different pressures, affecting the melt pool surface tension. Eventually, Bisht et al. (2018) and Kolb et al. (2018b) showed that the lack of uniformity of the gas flow within the chamber may cause unstable melt pool dynamics leading to defective parts in some locations of the build area.

4.2 In-situ detectability of defects and prediction of final part properties

4.2.1. In-situ estimation of single track quality

Among the studies reported in Table 10 involving single track experiments, various authors proposed machine learning methods suitable to determine the quality of the track based on in-situ measurements.

Ye et al. (2018a) proposed a deep belief network classifier that exploited in-situ video imaging of process by-products. The algorithm was trained in two different modes: i) using in-situ images as direct inputs for the network, which led to a classification accuracy of about 83% and ii) using extracted spatter and plume descriptors (including areas, lengths, widths, orientations, perimeters, etc.), which led to a classification accuracy of about 81.9%. The same authors applied the same type of classifier to air-borne acoustic signals (Ye et al. 2018b). In this case, the raw acoustic signal was pre-filtered and processed via fast Fourier transform before being provided as input to the deep belief network. The results showed a classification accuracy of 93.63%. Zhang et al. (2018) compared different classification algorithms, either applied to plume and spatter descriptors or to raw images, showing that the best classification accuracy, in the order of 92.8%, could be achieved by applying a Convolutional Neural Network (CNN) directly on raw images. Zhang et al. (2020) showed that previously presented results could be further improved by additionally including temporal information within the trained network. The underlying idea is that the relevant information content about spatter and plume behaviour is not only captured by individual video frames, but also by variations in sequential frames. To this end, Zhang et al. (2020) proposed a hybrid CNN scheme consisting of two steps. In the first step, the network learns spatial features from single images. In the second step, the features extracted in step 1 are rearranged according to the video frame sequence and used as inputs to a second network. With this approach, an overall accuracy of 99.6% was achieved.

A semi-supervised classification approach was proposed by Yuan et al. (2019), who used melt pool images acquired by means of a co-axial high-speed camera. The semi-supervised paradigm allows training the classifier using both labelled and unlabeled data. Clearly, labelling individual data samples can be a time-consuming task and defining the correct label for some samples is not always straightforward. Single tracks AISI 316L stainless steel were labelled by measuring their height after the process. The proposed CNN applied to melt pool images combined a supervised and unsupervised model. The classifier was trained using 1000 training data points, by varying the number of labelled ones. Yuan et al. (2019) reported a successful classification rate of 93.8% when 50% of the training data were unlabeled. The classification performance decreased as the amount of unlabeled data increased.

All these methods were applied to single tracks of simple specimens. There is still a need for studies demonstrating the suitability of L-PBF by-product signatures, to identify changes of the process state in the presence of complex shapes, or to detect the onset of local defects.

4.2.2. In-situ prediction of microstructural properties

The in-situ prediction of microstructural properties, such as grain size and orientation, enables different interesting capabilities. First, it allows the detection of the local and global deviations (from an expected microstructure) that occur during the process. Second, it facilitates the support of novel solutions to adapt and tune the microstructure of functionally-graded products. In this framework, consolidated research has been carried out in EB-PBF by the Oak Ridge National Laboratory (Dehoff et al. 2019 and references therein). Raplee et al. (2017) presented a study on the use of in-situ thermography in EB-PBF to estimate the thermal gradient (G) and solid-liquid interface velocity (R) suitable to determine the grain orientation within a part (i.e., columnar against equiaxed grains). They validated the in-process microstructure prediction by testing two different scan strategies, namely point melt and line melt, which led to different microstructural properties in IN718 parts. As another result of the study, Raplee et al (2017) showed that regions with abnormal temperatures with respect to the surrounding area indicated the presence of swelling or pitting defects in the part. Fig. 19 shows an example of an in-situ thermal map, the histogram of the G/R ratio estimated from in-situ data of the line and point scan strategies and the corresponding different microstructural properties obtained from different locations in the part.

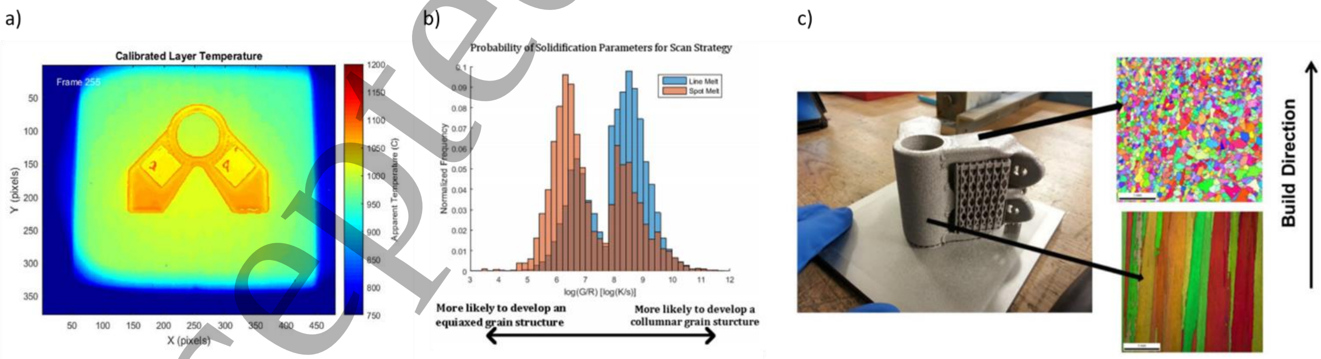

Figure 19. Examples from Raplee et al. (2017) and Dehoff et al. (2019): a) in-situ thermal map of a layer after calibration, b) histogram of the G/R ratios estimated in-situ for the line and point scan strategies, c) resulting columnar and equiaxed microstructures in different locations of the part

Correlations between in-situ thermography measurements have also been investigated in L-PBF. Rather than estimating G and R values, Williams et al. (2019) studied the effects of inter-layer cooling times (ILCT) on temperature profiles measured via off-axis IR video imaging. They showed that a shorter ILCT caused a greater grain growth and preferential orientation, with higher surface temperatures resulting in a lower G. Williams et al. (2019) observed other effects related to the ILCT, such as the increased number of spatters as a result of higher layer temperatures. The ILCT is determined not only by the processing of individual components, but also by the build composition in terms of number, size, shape and location of other parts in the same build. Accordingly, Williams et al. (2019) concluded that the qualification of a component must be carried out considering the overall build composition. If any component in the build changes, or other components are added or removed, the properties of all components in the build will be affected. In this context, in-situ monitoring may provide valuable support to control part-to-part and build-to-build variability.

4.2.3. In-situ porosity detection

Porosity is the defect that attracted the largest interest and highest number of studies in the literature. Nonetheless, the number of researchers who effectively demonstrated practical in-situ porosity detection capabilities, is still limited compared to the wide literature on in-situ process monitoring.

Table 11 provides an overall picture of studies that addressed the in-situ porosity detectability problem. Table 11 makes a distinction between i) voids included into the model of the part, which are also referred to as “artificial” or “intentional” pores in the literature , ii) local porosity (i.e., single pores or local clusters of pores, either spherical or irregular pores caused by lack of fusion – LoF) and iii) part density, i.e., the overall percentage of voids in the volume (or a portion of it). Table 11 shows that the majority of authors investigated the correlation between in-situ signals and the overall part density, but only few of them demonstrated the capability to detect local porosities within the part or even individual pores.

The advantage of inserting artificial pores in the part is that their location and shape is known in advance, hence it is easier to determine the effect of these artificial flaws on in-situ acquired signals. The main drawback is that the pattern of the measured process signatures is not fully representative of the one that can be observed when a real pore originates in the part. In effect, an artificial void implies that a small region of the layer is not scanned, whereas a real pore originates from the beam-material interaction without scan interruptions along the track.

Table 11 – Mapping of the methods for in-situ porosity detection in L-PBF and EB-PBF (references of methods in EB-PBF are shown with italic font)

Signatures of interest		Sensing method	Artificially injected voids	Local porosity / individual pores			Part density
				Spherical pores	LoF pores	Both	
Level 1	Surface pattern or height map of the printed slice	Off-axis imaging in visible range	Imani et al., 2019a,b; Abdelrahman et al., 2017			Gobert et al., 2018	Imani et al., 2019a,b; Lu et al., 2020; Lu et al., 2019;
		Off-axis NIR/IR imaging	Mahmoudi et al., 2019		*Yoder et al., 2019*		
		Blade-mounted sensor	Barrett et al., 2018b				
		Electronic imaging				*Arnold et al. 2018*	*Arnold et al. 2018*
Level 2	Heatmap / heating and cooling profiles	Off-axis NIR/IR video imaging	Mohr et al., 2020	Paulson et al. 2020		Mohr et al., 2020 Lough et al., 2020b; Lough et al., 2019; Bartlett et al., 2018	Lough et al., 2020b; Williams et al., 2019; Jalalahmadi et al., 2019; Foster et al., 2018
		Off-axis multispectral pyrometry					Montazeri et al., 2020
	Process by-products	Off-axis video-imaging in the visible range					Andani et al., 2018; Repossini et al., 2017
	Air-borne acoustic emissions	Air-borne acoustic emission detector					Wasmer et al., 2019; Shevchik et al., 2019
Level 3	Melt pool radiation intensity	Co-axial multi wave pyrometry /spatially integrated)					Jayasinghe et al., 2020; Alberts and al., 2017;
	Melt pool size and shape	Co-axial video imaging in the visible range					Kwon et al. 2020;
		Co-axial video imaging in the NIR range					Kolb et al., 2018b
	Melt pool temperature profile	Off-axis dual wavelength video imaging	Mitchell et al., 2020	Mitchell et al., 2020			
Level 4	Volumetric reconstruction	X-ray micro-tomography				Lhuissier et al., 2020	
	Acoustic emissions	Structure-borne acoustic emission detection					Eschner et al., 2020b

Voids of different shapes and sizes were used in various studies, including cubic voids with sizes in the range 30 μm to 300 μm (Mitchell et al. 2020) or 50 μm to 750 μm (Imani et al. 2019a,b, Abdelrahman et al. 2017), cylindrical voids with diameters in the range 50 μm to 750 μm (Imani et al. 2019a,b, Mahmoudi et al. 2019, Abdelrahman et al. 2017) and spherical voids with diameters in the range 600 μm to 900 μm (Mireles et al. 2015). Imani et al. (2019a,b) and Mahmoudi et al. (2019) used intentionally seeded voids to test the capability of their proposed layerwise surface pattern monitoring methods, to detect surface discontinuities within the printed area. Both the methods presented by Imani et al. (2019a,b) and Mahmoudi et al. (2019) were applied in L-PBF and worked by partitioning the surfaces into regions of interest (ROIs) and classifying them into defective or defect-free regions. In Imani et al. (2019a,b), ROIs were generated from optical layerwise imaging, such that each ROI has the same number of pixels but different shapes, to adapt to layerwise varying part geometry. Imani et al. (2019a) used a deep learning approach to classify the ROIs into defective or defect-free. An accuracy (i.e., the ratio of ROIs that were correctly identified) of 92.5% was reported for artificial voids of different sizes and shapes. In Mahmoudi et al. (2019), a thermal map of the layer was first created by merging melt pool images acquired during the process with an off-axis spatially resolved thermography setup. Then, multiple ROIs were identified as rectangular regions placed where connected components were observed after a binarisation of the layerwise reconstructed thermal map. Mahmoudi et al. (2019) proposed a modelling step, based on a Gaussian process model, that flags pixels with statistically significant deviations, followed by a final classification step to determine whether a ROI includes a defect or not. Tests were carried out in the presence of one single artificially seeded void. Both the methods presented by Imani et al. (2019a) and Mahmoudi et al. (2019) required a training phase involving samples of defective and defect-free image data.

Mitchell et al. (2020) proposed a method, based on off-axis dual wavelength video imaging, that combined the estimation of melt pool properties with a reconstruction of the layerwise thermal map of the part. In the presence of artificially seeded voids, Mitchell et al. (2020) showed that voids as small as 120 μm were identified, however, the in-situ reconstructed void volume was underestimated by up to 28% with respect to the corresponding post-process reconstruction via X-ray CT. Mitchell et al. (2020) additionally investigated the capability of automatically detecting not only artificial voids but also natural porosity generated by the process. The AISI 316L specimens produced via L-PBF mainly included spherical pores with an equivalent spherical diameter (ESD) ranging between 11.4 μm (minimum size detectable by the micro-CT) and 70 μm. A neighborhood searching algorithm was proposed to classify individual melt pool images into normal or outlier, by comparing the similarity of the melt pool in a given location with melt pools observed in its vicinity, within a given radius in terms of melt pool aspect ratio and orientation. Mitchell et al. (2020) showed that the percentage of pores detected by means of melt pool images signaled as outliers was in the range 25% to 55%, but it increased above 70% when considering only pores with ESD larger than 50 μm. Nevertheless, a relatively high false positive rate between 23% and 58% was reported. Examples of results from the study of Mitchell et al. (2020) are shown in Fig. 20. This study is, in effect, the only one (to our knowledge) that attempted to correlate individual melt pool signals with local pores in L-PBF.

The high false alarm rate highlights the need for further research developments to design more effective in-situ monitoring tools for porosity detection. Such high false alarm rates can also be related to the remelting effect as the process continues, which may cause partial pore annihilation in underneath layers.

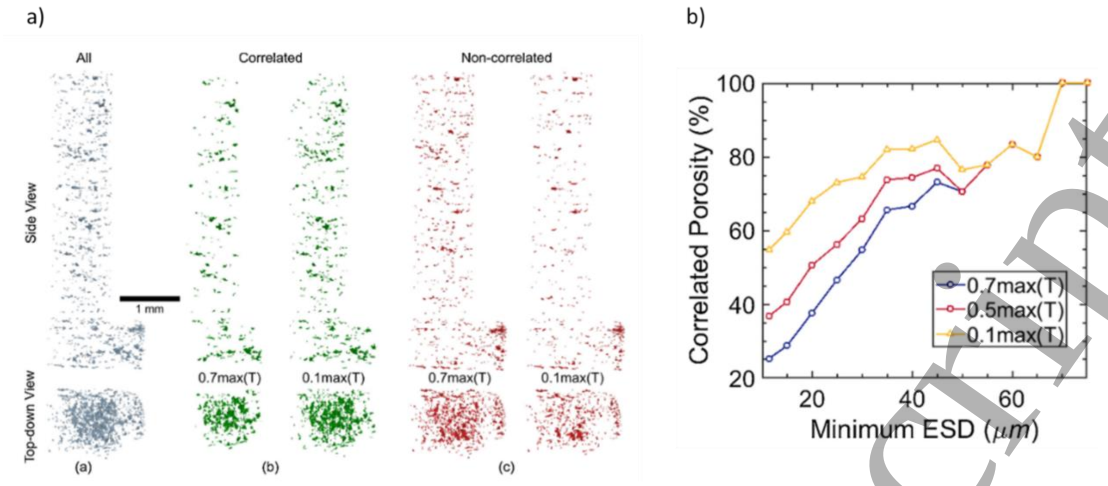

Figure 20. Examples of results from Mitchell et al. (2020): a) three-dimensional reconstructions of all pores identified using micro-CT, pores correlated with in-situ outlying melt pool signals, and pores not correlated; b) percentages of pores spatially coincident/correlated with outlier melt pools at different minimum ESDs and different threshold values

Other studies investigated the capability to detect local pores using different in-situ monitoring approaches. As far as level 1 methods are concerned, Gobert et al. (2018) presented a voxel-wise comparison between a 3D reconstruction of the part, based on in-situ layerwise image pixel intensities and the post-process X-ray CT reconstruction. A landmark-based registration between the in-situ data and the CT data was applied. Then, the support vector machine (SVM) approach was used as a binary classifier to detect flaws in the in-situ reconstruction. Layerwise images were acquired with different illumination conditions, and Gobert et al. (2018), extending the previous work of Morgan et al (2017), showed that the most appropriate pore detection performances were achieved using an ensemble learning system, merging SVM models associated with each condition. The test specimen built with stainless steel powder had pores with ESD in the range 29.5 μm to 50.5 μm (with very few above 50.5 μm). Gobert et al. (2018) reported a detection accuracy of 85%, with a “precision” of 64%, where the precision was defined as the ratio between the number of true positives and the total number of true positives and false positives.

A comparison between in-situ and post-process X-ray CT reconstructions of specimens, produced via L-PBF, was presented by Bamberg et al. (2016), who performed a layerwise mapping of hot and cold areas. This method was later implemented by EOS in the EOSTATE suite and called “Optical Tomography”. Although no information about the pore detection algorithm was provided, the authors showed a probability of detection between 90% and 95% for lack-of-fusion flaws with diameters in the order of 150 μm.

A voxel-wise comparison between thermal signatures generated via in-situ thermography and the X-ray CT of the part was carried out by Mohr et al. (2020), Lough et al. (2020b, 2019) and Bartlett et al. (2018). Lough et al. (2020b) compared different synthetic descriptors to generate layerwise thermal maps from IR video image data. They showed a correlation between the proposed synthetic indexes and the presence of local pores (at least the largest ones). Bartlett et al. (2018) proposed another rule to detect potential anomalies in thermal maps. The rule consists of signaling any pixel whose temperature is K standard deviations above or below the average temperature of the layer. They applied this approach to cylindrical specimens, showing a detection rate of 33% for keyhole porosity and 82% for lack-of-fusion porosity. Pores below approximately 50 μm were only detected with a 50% success rate, whereas all pores larger than 500 μm were correctly detected.

A correlation between subsurface pores and cooling profiles reconstructed via in-situ thermography was presented by Paulson et al. (2020), however, in this case, in-situ X-ray video imaging was used as ground truth instead of post-process X-ray CT inspection. Pores were classified into small (<10 μm) and large (>10 μm), mainly focusing on spherical ones. By testing different sets of thermal history features and different classification algorithms, an accuracy in the range 84% to 100% was reported.

Similar comparisons between in-situ reconstructed porosity maps and X-ray CT inspections have also been carried out in EB-PBF. Yoder et al. (2019) used the LayerQam system developed by Arcam (GE Additive) to acquire layerwise images of the build in the NIR range. Potential pores were identified simply by setting a threshold-to-pixel intensity, as surface cavities were assumed to yield a bright spot in the image. Lack-of-fusion defects were concentrated in banded regions along vertical tensile specimens. Yoder et al. (2019) qualitatively demonstrated the correspondence between pore concentration regions signaled by the in-situ monitoring tool and "ground truth" pore concentration regions from the X-ray CT measurements. Arnold et al. (2018), instead, showed a comparison between in-situ electronic imaging, post-process optical microscopy on a prepared micro-section and X-ray CT, as shown in Fig. 21. Rather than identifying individual pores, Arnold et al. (2018) directly compared the pixel intensities in the images generated with different in-situ and ex-situ methods. A good agreement was highlighted for lack-of-fusion pores larger than 100 μm.

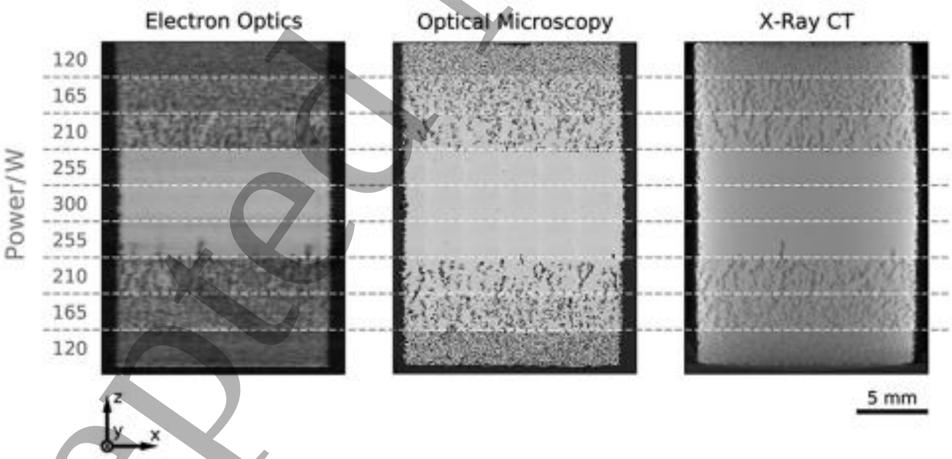

Figure 21. Comparison between a cross-Section from an in-situ electronic image, ex-situ optical microscopy and ex-situ X-ray CT (Arnold et al., 2018)

The possibility of detecting in-situ individual pores was further discussed by Lhuissier et al. (2020) who used the same proposed in-situ X-ray CT approach in L-PBF. However, a comparison between in-situ detected pores and pores observed in ground truth post-process inspection has not been carried out (to our knowledge).

Rather than trying to identify single pores or local clusters of pores, a large number of researchers correlated in-situ signals with the global porosity of the part, commonly measured by means of the Archimede's approach or as a cumulation of pore areas from other inspection techniques. Among them, Lu et al. (2019, 2020) showed the correlation between surface features extracted from layerwise optical images within the printed area after powder recoating and the density of the part. These features correspond to superelevated solidified areas and edges. Aminzadeh and Kurfess (2019), instead, showed the correlation between surface features extracted after the melting phase and the final part density. Aminzadeh and Kurfess (2019) also proposed a Bayesian classifier applied to surface texture features extracted from laywerise images of the printed area. Smooth and irregular surface patterns were generated by varying the laser power and scan speed. Images were binarised and converted into the frequency domain, in order to feed synthetic descriptors of the fast Fourier transform as input variables for the classifier. A classification precision of 83% was reported in an application on simple specimens made of Inconel 625.

Montazeri et al. (2020) proposed a method for the classification of porosity into discrete classes or the prediction of an average porosity index using an off-axis multi-spectral spatially integrated pyrometry measurement in L-PBF. The method involved a transformation of the acquired signal into a graph and the application of a graph Fourier transform to compute the Fourier coefficients used as synthetic features for porosity classification (via K-nearest neighborhood) and prediction (via artificial neural networks). Montazeri et al. (2020) reported a prediction error of approximately 10%. Moreover, by dividing porosity into acceptable and unacceptable depending on the overall pore area observed in different layers, Montazeri et al. (2020) reported a 99% correct detection rate with a percentage of false alarms of about 28%. A similar approach was presented by Montazeri and Rao (2018) to distinguish between overhang and bulk build states.

Okaro et al. (2019) proposed a semi-supervised classification approach applied to co-axial photodiode signals in L-PBF. The proposed method was based on a Gaussian mixture model and was trained to classify acceptable and faulty L-PBF builds of Inconel 718 specimens. A SVD of the training data matrix was applied to extract the features to be used for build classification. Okaro et al. (2019) reported a successful classification rate of 77% with a training dataset consisting of twenty-five labelled specimens and twenty-four unlabeled ones.

Melt pool images were usually provided as direct inputs to the network for automated feature extraction. A different approach was proposed by Scime and Beuth (2019), who applied a multi-step pre-processing phase, consisting of the extraction of the scale-invariant features that characterize the gradient field and surround each pixel in the image. These features were used as inputs for the SVM methodology to classify melt pool images along the single tracks of Inconel 718, on bulk or overhang areas. In Scime and Beuth (2019), melt pool images were divided into acceptable and non-acceptable categories, but the correspondence to actual defects was not discussed.

Repossini et al. (2017) showed that the classification of different density conditions corresponding to undermelting or overmelting process states could be enhanced by combining synthetic descriptors of the laser heated zone with spatter descriptors (number, size and spatial dispersion). A logistic regression method was applied to this aim, showing the suitability of spatter-enclosed information for process monitoring purposes.

Further examples of machine learning methods for the classification of process states leading to different part densities were presented by Eschner et al. (2020b), Shevchik et al. (2019) and Wasmer et al. (2019) using acoustic emission signals. Eschner et al. (2020b) applied a multilayer perceptron network to classify different energy density levels, using the spectrogram of the high-frequency structure-borne acoustic emission signal, in the L-PBF of AISI 316L specimens, with a successful classification rate of about 83%. Eschner et al. (2020b) also investigated the effect of geometrical complexity on classification performance, highlighting a slight worsening as complexity increased. Shevchik et al. (2019) and Wasmer et al. (2019) proposed a deep learning and reinforcement learning approaches applied to the wavelet decomposition of air-borne acoustic emission signals, during the L-PBF of CL20ES stainless steel samples with varying energy density along the build direction. A successful classification in the order of 78% was reported in Wasmer et al. (2019), whereas the successful classification results from different strategies discussed in Shevchik et al. (2019) ranged between 73% and 91%.

4.2.4. In-situ detection of geometrical distortions

Almost all the methods presented in the literature for the in-situ detection of geometrical distortions belong to level 1 and level 2. Regarding level 1 methods, the possibility to directly measure the geometry of the printed slice represents the major driver for in-situ geometrical distortion detection. However, only a few researchers developed automated alarm rules for the detection of deviations from the nominal shape with a validation based on ex-situ inspections of the final part. Gaikwad et al. (2019) presented a CNN for the in-situ prediction of the quality of thin-wall Ti6Al4V parts in L-PBF. Instead of reconstructing the slice contour, de-noised and binarised images of the powder bed were provided as input to the CNN. Gaikwad et al. (2019) showed agreement in the range 80% to 98% between the in-situ predicted quality of the thin walls and their ex-situ measured quality.

More recently, Pagani et al. (2020) presented a statistical process monitoring approach for the in-situ detection of geometrical errors in L-PBF. The method allows modelling the natural variability of geometric errors for complex shapes whose layerwise geometry is changing every layer. This approach enabled the identification of anomalies in one or multiple layers through the estimation of a deviation index capturing local mismatches between the in-situ observed shape and the nominal one from the slice CAD model. The method was tested by producing Ti6Al4V specimens with complex shapes on an industrial L-PBF system, using the already embedded powder bed camera and light source. Pagani et al. (2020) showed that the proposed approach produced a false alarm rate very close to the targeted one and allowed the signaling of various anomalies corresponding to geometrical deformations quantified after the process via X-ray CT inspection. Fig. 22 shows examples of thin-wall quality prediction by Gaikwad et al. (2019) and the statistical process monitoring approach developed by Pagani et al. (2020).

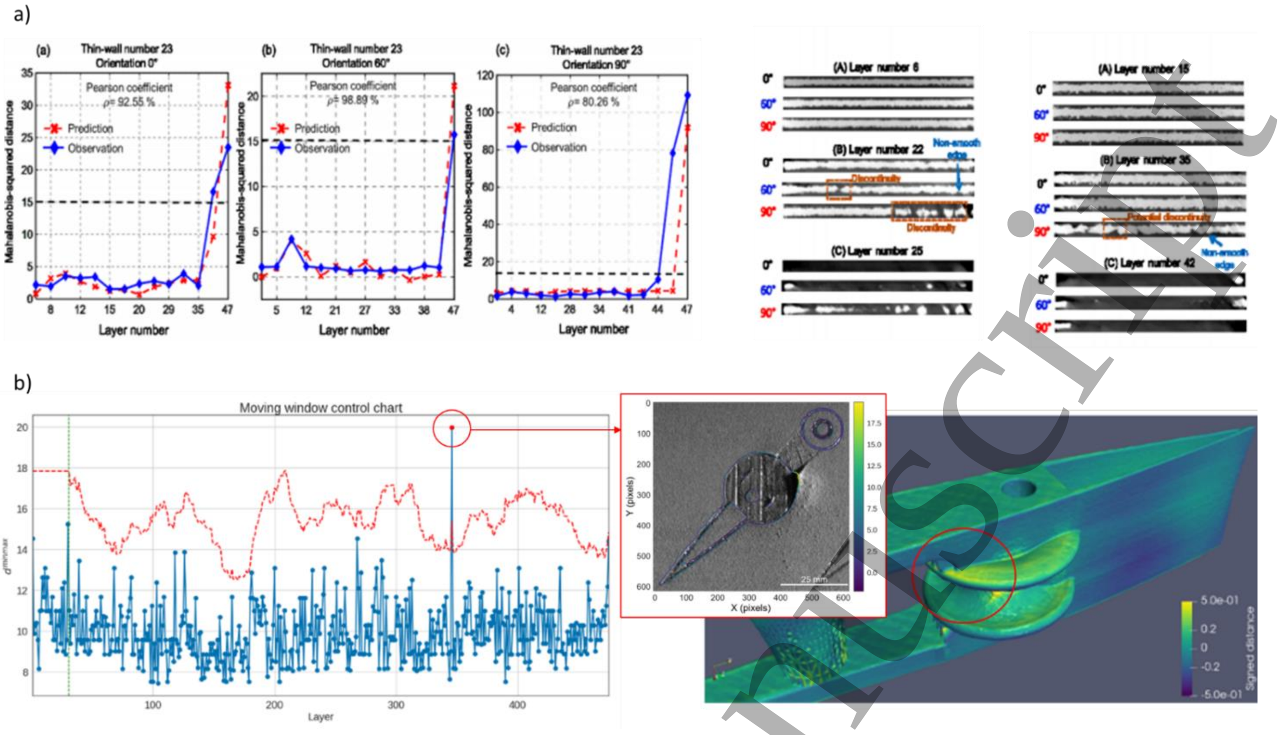

Figure 22. a) Comparison between in-situ and ex-situ estimates of the thin-wall quality in Gaikwad et al. (2019) for different thin wall orientations (the horizontal dashed line indicates the upper limit before the thin wall collapsed) and examples of thin-wall defects; b) moving window control chart for the in-situ detection of geometrical distortions proposed by Pagani et al. (2020) with an example of a detected geometrical distortion caused by warpage of the part.

Level 1 methods, based on the analysis of the surface patterns of the powder bed and the printed slice, could also be suitable to detect geometrical distortions. In this regard, a few researchers demonstrated correlations between in-situ detected and classified anomalies, in one or multiple layers, and the final quality of the part. Scime and Beuth (2018a,b) combined layerwise imaging in the visible range with a multi-scale CNN (MsCNN) in L-PBF, to automatically detect various kinds of anomalies, i.e., recoater hopping and streaking, incomplete powder spreading, presence of debris on the powder bed, super-elevated edges and other part damages. Part damages were successfully classified in 94.2% of test samples with a false alarm rate of 0.7% (anomalies of any kind signaled in defect-free images). The method was validated during the L-PBF of an Inconel 718 heat exchanger, where macroscopic defects were observed and detected by the proposed approach. The training was performed using fifty-one builds produced on industrial systems involving different materials. A human expert manually selected square image patches from powder bed images corresponding to either correct powder spreading or anomalies belonging to different categories. The training set included about 10,000 patches. Although the formation of such a large dataset could be quite demanding, once it has been made available, it could be used to train the classifier implemented on different L-PBF machines during the production of different materials.

Scime et al. (2020) recently extended and tuned the method previously proposed by Scime and Beuth (2018) and tested a transfer learning approach for the implementation of a classification algorithm, not only on different L-PBF machines from different vendors, but also in various metal AM technologies, i.e., EB-PBF and binder jetting, using different sensing setups. Scime et al. (2020) showed that false positive and false negative rates varied within a relatively wide range, depending on the AM system where the algorithm was tested. Best validation performances involved a false alarm rate of 0.4% and a true positive rate of 99.8%. Examples of in-situ detected geometrical distortions with these methods are shown in Fig. 23.

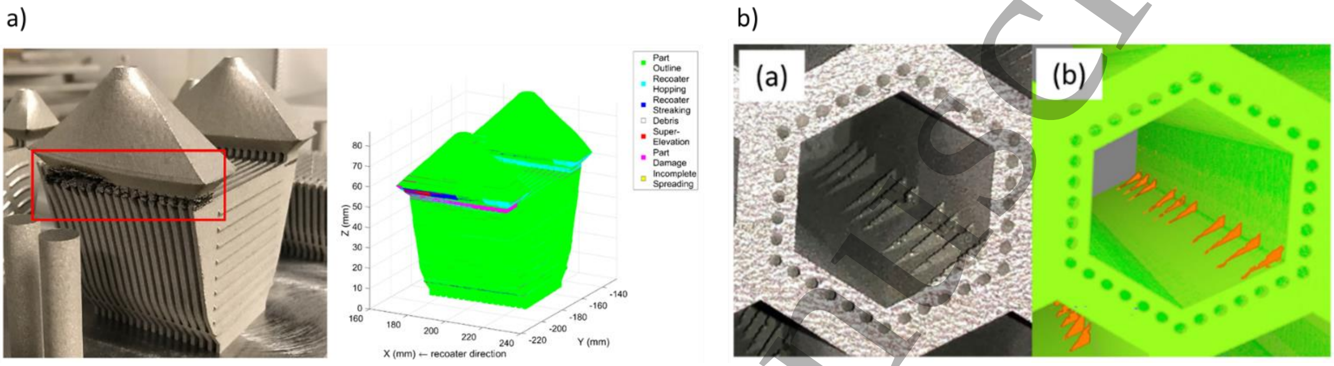

Figure 23. Examples of geometrical distortions and corresponding in-situ anomaly detection in a) Scime and Beuth (2018a) and b) Scime et al. (2020)

A few other solutions suitable to detect anomalies affecting the geometrical accuracy of the part were proposed in the literature using level 2 in-situ monitoring methods. Grasso et al. (2016) and Colosimo and Grasso (2020) proposed a hot-spot detection methodology based on the in-process analysis of the spatio-temporal auto-correlation pattern of pixel intensities in high-speed videos gathered through off-axis machine vision in the visible range. They showed that local anomalous heat accumulations in L-PBF could lead to micro- and macro-scale geometrical deformations in the final part. Grasso et al. (2016) proposed the use of an extension of the principal component analysis (PCA) method for high-speed video-image data. This extension, also known as “T-mode PCA”, is suitable to detect pixels whose intensity patterns over time exhibit anomalous temporal auto-correlations, which is a condition typically associated with pixels that remain hot for a long time with a slow cooling gradient. The spatial mapping of a synthetic PCA-based control statistic combined with a clustering-based alarm rule allowed the automated identification and localisation of local hot-spot events.

Colosimo and Grasso (2020) extended the previous study by presenting a spatio-temporal PCA method, where a spatial weight matrix was included into the PCA decomposition to account for both the temporal and spatial auto-correlations of pixel intensities in the video image. This allowed the detection of hot-spot events to be faster and more reliable. The method was tested during the L-PBF production of a complex geometry where hot-spots originated due to the presence of over-hang acute corners, leading to local geometrical distortions. In-situ video images were acquired by means of a high-speed camera in the visible range, placed outside the front viewport of an industrial L-PBF system. An example of the in-situ hot-spot detection and corresponding part defects is shown in Fig. 24. A more recent study of the same authors (Ye et al., 2020) presented a different approach based on the spatio-temporal modelling of background and foreground patterns of the same high-speed video image data. Ye et al. (2020) showed that the proposed model-based approach was faster and more computationally efficient in detecting hot-spot events, at the expense of a number of parameters that needed to be tuned in the training phase.

A different perspective was adopted in Grasso et al. (2018a) and Grasso and Colosimo (2019) where a statistical monitoring method was proposed to monitor the stability over time of plume emissions during the L-PBF of pure zinc specimens with different process parameters. Off-axis IR video images were processed to isolate the ROI corresponding to the plume and extract salient features, such as the area, average intensity and orientation. A few initial layers were used to estimate the control limits to be applied in all following layers. Results showed that unstable process conditions leading to defective parts could be quickly detected since their onset stage. Such out-of-control states were characterized by anomalous and explosive plume patterns becoming more and more frequent along the build. Results also showed that no violations of the control limits occurred when optimal process parameters were used, leading to fully dense parts.

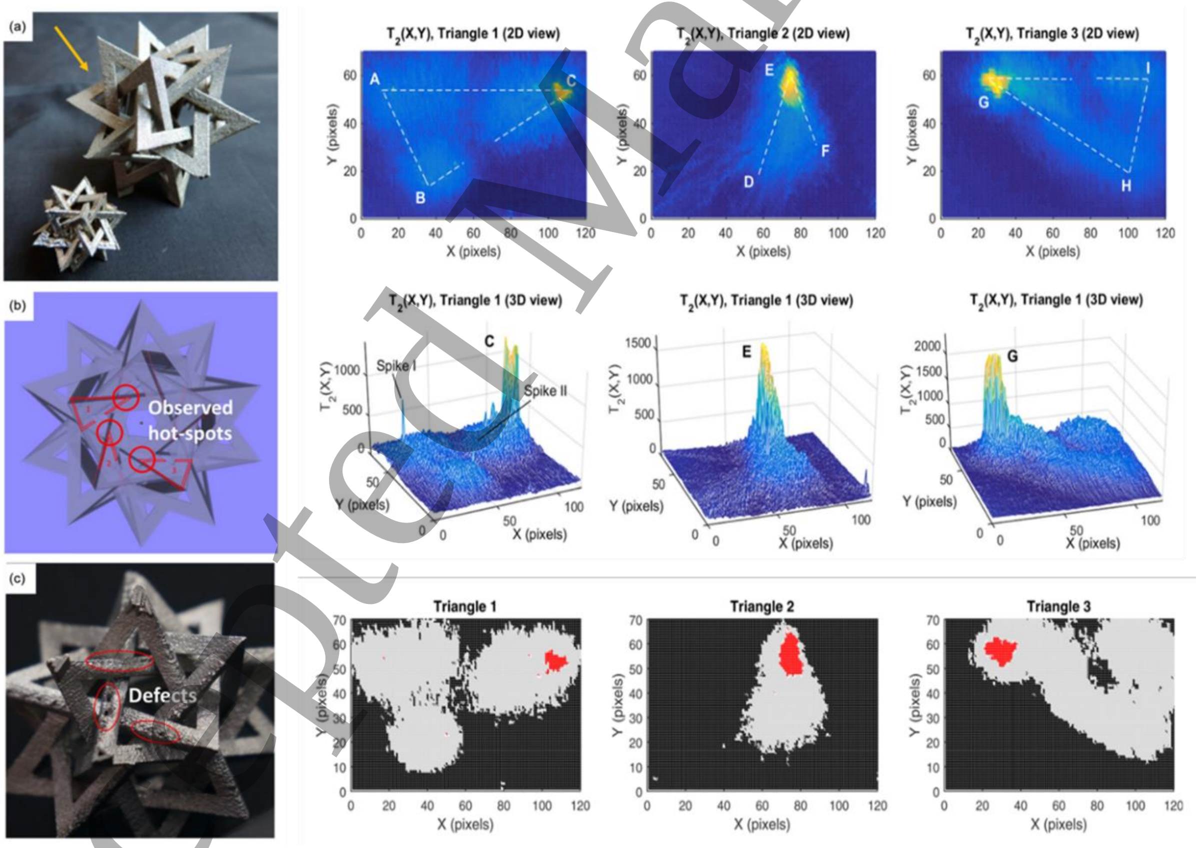

Figure 24. Examples of local geometrical defects in a complex shape produced via L-PBF and the corresponding in-situ detection of hot-spot events that caused those defects (Colosimo and Grasso, 2018)

In EB-PBF, Grasso et al. (2018b) presented a level 0 method for the detection of anomalies in EB-PBF that was applied to detect severe swelling caused by improper powder recoating. A SVM-based methodology was proposed to estimate a multi-variate control region capturing the natural variability of multi-channel log signal data. The method was trained with data gathered during the production of few defect-free replicates of the same part. After the training phase, the method was used for the statistical monitoring of log signal data in following processes. The method is also suitable for series production applications, which represent the most common industrial use of the EB-PBF technology.

4.2.5. Other defects: residual stresses, cracks and delamination

As discussed in Section 3.5, a research question that has attracted increasing interest both in the scientific literature and in industry is the capability to detect anomalies occurring underneath the currently processed layer. In this context, a few researchers demonstrated the capability to either measure the development of stresses in the part while it is being built or detect delamination events caused by excessive residual stress accumulations.

Among the level 4 methods suitable to “look” under the layer using X-ray measurement techniques is X-ray diffraction. This technique was proven suitable to measure strain and stress formations in the part together with phase changes during the process. Calta et al. (2018) and Zhao et al. (2017) used this technique during single track experiments, using custom built L-PBF systems. More recently, Schmeiser et al. (2020) demonstrated the feasibility of stress and strain development measurements, during the production of three-dimensional specimens. The study involved the L-PBF of Inconel 625, and the authors were able to quantify stresses along different directions. They found that in-plane stresses were generally higher than out-of-plane stresses, and were able to characterize directional differences of compressive and tensile stresses, and their development along the build. The method was tested during the production of specimens with dimension $(20 \times 5 \times 2.5)$ mm, where 2.5 mm is the thickness in the direction parallel to the synchrotron radiation beam. Schmeiser et al. (2020) pointed out that the proposed approach could be scaled up to industrial machines, whereas no indication about constraints on in-situ inspectable part dimensions were provided.

A method for the detection of delamination events was presented by Hehr et al. (2020). The authors developed a “smart” build-plate with embedded fibre optic strain sensors and tested it during an L-PBF process of AlSi10Mg parts that delaminated from the baseplate. Part geometries with varying aspect ratios and no preheating step were used to induce delamination. Hehr et al. (2020) showed a qualitative correlation between the spatial map of the measured strains, the directionality of the strain-vectors and the locations where delamination occurred. Additional research is needed to determine, in a quantitative way, the capability to detect damage occurrence and the location and direction of damage progression. This approach aims to detect delamination or cracking that occur near the baseplate surface and may not be visible with powder bed imaging sensors. When the effect of delamination is visible in the currently processed layers, in terms of out-of-plane geometrical distortions of the part, level 1 and level 2 in-situ monitoring methods could also be suitable for defect detection. For example, in L-PBF, Baumgartl et al. (2020) presented a deep learning approach for the automated detection of severe defects that cause large heat accumulations in the layer, such as delamination, via off-axis IR video imaging, but only few experimental details were provided.

In addition to the methods discussed above, structure-borne acoustic emission sensors are, in principle, also suitable to detect delamination and cracking events. This potential capability led to some recent developments in industrial in-situ monitoring toolkits. A recent patent from Renishaw showed the possibility of integrating structure-borne acoustic emission sensors at the four corners of the baseplate, enabling not only the detection of sudden elastic energy releases, e.g., caused by cracks or support detachment, but also the localization of the energy release source within the build area through signal triangulation (Northeast et al. 2018). Despite being an interesting and promising research field, there is still a lack of studies that experimentally demonstrate this defect detection capability.

5 Process control

The large and quickly growing number of studies reviewed in previous sections highlights the importance of in-situ and in-process measurements to improve the quality, repeatability and capability of PBF processes. In-situ measurements can be used to design and develop process control and optimization loops at different level. Fig. 25 shows the framework of control and optimization loops in PBF proposed by Liu et al. (2020b).

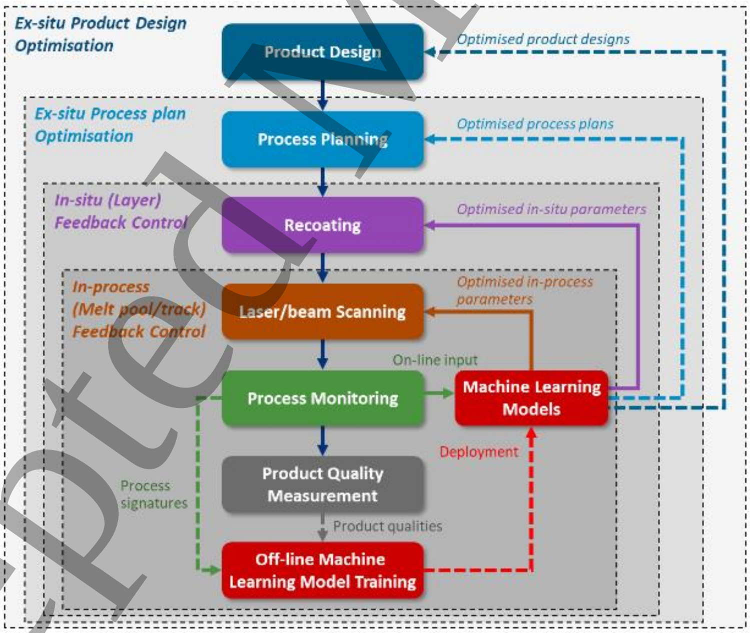

Figure 25. Generic framework for the use of in-situ measured data in the development of process control and optimization loops in PBF (Liu et al. 2020b).

Some defects and undesired variations can be predicted, as they are related to the geometry of the part and the thermo-mechanical interactions occurring during the process. These defects can be at least partially avoided by pre-correcting the geometry model or by setting locally varying process parameters and scan strategies in the build file transferred to the L-PBF system. These two methods represent the two outer loops in Fig. 25 and they rely on process modelling and numerical simulation techniques, taking advantage of in-situ gathered data for model tuning and calibration. Whereas the pre-compensation of geometrical distortions in the CAD file (ex-situ product design optimization) is becoming a common practice with various implementations in industrial software (Druzgalski et al. 2020), model-based adaptation of process parameters (ex-situ process plan optimization, also known as model-based feedforward control), represents an active research field. Some recent results of the feasibility and effectiveness of this approach were presented in Druzgalski et al. (2020). The authors proposed a method that extracts the geometry and scan path features from the build file and maps each scan track to pre-computed simulation results to set locally varying optimal process parameters. The method was applied to overhang features, resulting in a reduction of dross formation with respect to the same part produced without any feedforward control. Variants of the feedforward control approaches were presented by Wang et al. (2020b) and Yeung and Lane (2020).

Unfortunately, not all defects can be predicted due to many sources of stochastic variability, nuisance factors related to the degradation of performances system calibration and the prediction uncertainty of process simulation tools. In this framework, in-situ sensor signals represent the information source to enable additional in-situ and in-process control loops. One way to exploit in-situ data to this aim consists of combining in-situ measurements and real-time closed-loop adaptation of process parameters at melt pool or track level. The famous seminal study of Kruth et al. (2007) demonstrated the feasibility of this approach by using the co-axially measured melt pool intensity as real-time feedback information from the process. Since these seminal findings only few novel solutions have been proposed and validated, due to the several challenges related to real-time adaptation of process parameters at very high speed using noisy and geometry-dependent signals.

A recent study explored the combination of feedback and feedforward control methods (Renken et al. 2019). Model-based feedforward control was used to locally adapt process parameters in the presence of critical geometrical features (e.g., overhang surfaces). The closed-loop control of laser power using as input information the melt pool intensity enabled the additional reduction of fluctuations and deviations from a target set point that could not be avoided with the feedforward control method alone. The continuous variation of the laser power along the scan of each track is a challenging task on state-of-the-art L-PBF systems exploiting very high scan speed and, in most cases, multiple laser beams. An alternative approach involves a process parameter adaptation on a layer-by-layer basis. In these cases, the information gathered in previous layers can be used to adapt the set point for tuning process parameters in the next layer. An example of this approach was presented in Vasileska et al. (2020), where a layer-wise control strategy based on coaxial melt pool monitoring was proposed. Starting from a set point of the melt pool area defined on a simple geometry, the melt pool area was then monitored on more complex shapes, and the melt pool area measured on each scan vector was used to compensate the energy density of the same scan vector in the next layer. The study showed that this approach was effective in reducing swelling defects.

When all previous control strategies are not applicable or not sufficient to guarantee actual defect-free components, one further type of intervention regards the in-situ correction or removal of defects after they have been detected. To this aim, layer re-melting has been investigated as a repairing solution to reduce internal porosity, surface roughness, local stress concentration and to improve microstructure characteristics (Heeling and Wegener 2018, Demir and Previtali, 2017). Numerical and experimental studies for the selection of optimal re-melting process parameters and defect repairing strategies were presented by Jalalahmadi et al. (2019) and Demir et al. (2018), respectively. Re-melting for in-situ defect correction was proposed in EB-PBF too. Mireles et al. (2015b) showed the feasibility of triggering a re-melting process to correct the defect based on anomalies observed via in-situ thermography.

Another defect repairing solution consists of combining additive and subtractive processes in the same machine to “cancel” defective areas or entire defective layers while the part is being produced. Some authors discussed the combination of L-PBF and selective laser erosion to improve the layerwise surface characteristics and, in principle, to remove defective layers before re-starting the process (Yasa et al. 2011). Another concept was implemented and tested on an open-architecture L-PBF system called Penelope (Colosimo et al. 2020). A multi-sensor monitoring architecture was combined with a hybrid apparatus for in-situ defect removal. Such capability was achieved by using a surface grinding wheel mounted on a linear axis, which is activated as soon as an alarm is signalled by the in-situ monitoring system. The surface grinding operation allows getting rid of the last produced layers where the defects were identified. After the layer removal operation, the L-PBF process goes one with modified process parameters to avoid the re-occurrence of the same defect. In-situ defect correction or removal could be combined with previously mentioned control architectures, to integrate different reaction and recovery capabilities suitable to maximize the avoidance of flaws and to enhance the final quality and performances of the product.

6 Open issues and future research directions

Several studies have been devoted to in-situ measurement and monitoring of PBF processes in the recent years, with an average rate of almost eight new publications every month in the first semester of 2020. The majority of these studies can be classified in the following four categories: i) studies that demonstrated the feasibility and/or accuracy of in-situ sensing or measurement methods, ii) studies that showed how the measured signatures were affected by varying process parameters, scan strategies or other controllable factors, iii) studies that used in-situ measurements to understand and clarify underlying process dynamics and beam-material interactions, and iv) studies that presented and demonstrated in-situ anomaly and defect detection capabilities. It is interesting to note that about 80% of papers published in the last two years and reviewed in the present study belong to the latter category. This fact highlights the increasing interest for machine learning and statistical process monitoring methods suitable to make sense of in-situ acquired data and automatically detect anomalous process states.

The most investigated type of defects in the literature is porosity, but there still is a lack of methods suitable to detect local flaws with acceptable false alarm rates. Despite a few researchers showing that pores with equivalent spherical diameters larger than 100 µm can be detected with relatively high success rates, high false alarm rates were reported. Such high false alarm rate has different root causes that deserve additional investigation. One of them is the pore annihilation as a result of partial remelting when following layers are produced.

Another limitation of the current state of the art regards the fact that, in the majority of studies, the proposed methods were tested during single track experiments or during the production of simple specimens. This is often motivated by the need for easing post-process inspections and tests to correlate in-situ measurements with quality and mechanical properties. This leads to at least two main issues. On the one hand, defect onset mechanisms and process signature dynamics in complex shapes can be quite different from those observed in simple specimens. On the other hand, there is a lack of methods to transfer knowledge and models from the simple specimens used during the development phase to the in-situ monitoring of more complex shapes. In all these cases, data from copies of the same simple geometry were used. Transfer learning methods (Colosimo et al. 2018, Tsung et al. 2018) still must be explored and validated to deal with continuously changing part geometries and with the portability of the developed methods from machine to machine. This latter issue is also related to the training of machine learning approaches for defect detection or process state classification. Most studies used supervised training paradigms, where labelled data from both defective and defect-free parts were used to get the desired classification or prediction performances. The acquisition of a sufficient amount of data representative of signal patterns in the presence of defects or faulty states may be difficult to achieve in practise, and data labelling may be a time-consuming and troublesome task. Only in a few cases did authors investigate semi-supervised methods, relying on both labelled and unlabelled training data, or one-class-classification methods, where the classifier (or the process monitoring tool) was trained on data representative of the natural process behaviour only. Additional research efforts are needed to develop in-situ monitoring tools that are not only able to minimize the false alarm rate, but also characterized by training procedures that can be easily and effectively implemented for industrial application. In addition, traditional artificial intelligence-based methods are noticeably effective when input data are characterized by a stable and repeatable process signature, due to the possibility of collecting extensive training datasets. In the presence of “dynamic” process signatures that continuously vary as a consequence of varying part geometry, scan strategy, material, machine, etc., there could be the need for more adaptive and “self-learning” paradigms, which represents a field of considerable interest for future research.

Many other challenges also need to be faced to bridge the gap between research and industrial implementations. Almost all reviewed in-situ data analysis methods were not applied and tested in real-time, and very few authors provided data about computational costs implied by their proposed methods. In-situ data streams from high spatial and/or high temporal resolution sensors, during builds consisting of thousands of layers, impose the need for efficient solutions to handle very big and fast datasets. Typical problems often encountered in industrial applications of statistical quality monitoring and control (also referred to as statistical process control – SPC) characterize the practical implementation of many approaches developed for in-situ monitoring of AM (Colosimo et al. 2018, Colosimo 2018, Colosimo 2020): the need for large training data sets, which implies similar shapes printed along all the layers and repeated production of similar jobs, together with the need of solutions for big data mining (in terms of *volume*, *velocity* and *variety*) are all barriers to the use of the developed approaches in real industrial settings.

Real-time and efficient big data analysis represents a key issue for the development of closed-loop control (Renken et al. 2019, Vasileska et al. 2020, Colosimo et al. 2020) and/or in-situ defect correction and removal techniques. Many authors studied machine learning techniques applied to high-speed data (in the order of 10 – 100 kHz), but basically all reviewed methods were tested off-line, and computational efficiency issues were addressed by few authors. Moreover, in-situ acquired signals during one entire process may lead to several gigabytes of data to be managed and stored. The lack of consolidated real-time implementations still represents one of factors contributing to the existing gap between the wide research in this field and industrially adopted solutions. This is a field where several research efforts and industrial developments are currently required.

Few studies investigated the potentials of combining data from multiple sensors and/or combining different in-situ monitoring levels to enhance the robustness and effectiveness of in-situ defect detection or to extend the range of detectable anomalies. As industrial systems become more and more equipped with multiple sensors, this represents an interesting opportunity to study and develop novel multi-sensor data fusion methodologies. Another challenge related to the implementation of industrial in-situ monitoring solutions is related to the fact that many sensing methods used in research studies are expensive, difficult or even impossible to install on industrial machines. Some recent studies compared different sensing methods to investigate the compromise between measurement performance and economic viability (Montazeri and Rao 2018, Foster et al. 2018). The feasibility of replacing high-fidelity and expensive sensors with low-fidelity and low-cost ones, possibly combining data fusion techniques from multiple sources, has received little to no investigation in the reviewed literature.

Some researchers pointed out the possible combination of real-time data and process simulations to enhance in-situ anomaly detection and to enable more efficient solutions for zero-defect AM. However, such digital twin solutions have only been explored at a preliminarily level and PBF process simulation is another field where additional research development is needed (Montazeri et al. 2020, Alldredge et al. 2018).

The process control framework discussed in Section 5 highlighted that in-situ measured data could be used to design and develop different process control and optimization loops to pre-compensate geometrical errors, prevent the occurrence of defects in critical geometrical features and mitigate or correct defects when they have been signalled by in-situ process monitoring techniques. After a long-lasting temporal gap following first seminal studies in this area, various novel solutions have been proposed very recently. These studies have the great potential to pave the way towards a novel generation of smart PBF systems. Indeed, the fast growth of the research devoted to in-situ measurement, monitoring and control, combined with the large number of research centres and industrial groups committed to the development of novel solutions in this field, is expected to significantly push forward the current technological and knowledge boundaries in the next few years.

Acknowledgements

Prof. B.M. Colosimo and Dr. M. Grasso's research was partially supported by the IAMSPACE Project - Italy for Additive Manufacturing in SPACE, funded by the European Space Agency in the framework of agreement AO10042- "Preparation of Enabling Space Technologies and Building Blocks: AM process Monitoring and Structural Integrity".

References

Abdelrahman, M., Reutzel, E. W., Nassar, A. R., & Starr, T. L. (2017). Flaw detection in powder bed fusion using optical imaging. Additive Manufacturing, 15, 1-11.

Alberts, D., Schwarze, D., & Witt, G. (2017). In Situ Melt Pool Monitoring And The Correlation To Part Density Of Inconel® 718 For Quality Assurance In Selective Laser Melting. In International Solid Freeform Fabrication Symposium, Austin, TX, USA (pp. 1481-1494).

Alldredge, J., Slotwinski, J., Storck, S., Kim, S., Goldberg, A., & Montalbano, T. (2018, April). In-Situ monitoring and modeling of metal additive manufacturing powder bed fusion. In AIP Conference Proceedings (Vol. 1949, No. 1, p. 020007). AIP Publishing LLC.

Aminzadeh, M., & Kurfess, T. R. (2019). Online quality inspection using Bayesian classification in powder-bed additive manufacturing from high-resolution visual camera images. Journal of Intelligent Manufacturing, 30(6), 2505-2523.

Andani, M. T., Dehghani, R., Karamooz-Ravari, M. R., Mirzaeifar, R., & Ni, J. (2017). Spatter formation in selective laser melting process using multi-laser technology. Materials & Design, 131, 460-469.

Andani, M. T., Dehghani, R., Karamooz-Ravari, M. R., Mirzaeifar, R., & Ni, J. (2018). A study on the effect of energy input on spatter particles creation during selective laser melting process. Additive Manufacturing, 20, 33-43.

Angelone, R., Caggiano, A., Teti, R., Spierings, A., Staub, A., & Wegener, K. (2020). Bio-Intelligent Selective Laser Melting System based on Convolutional Neural Networks for In-Process Fault Identification. Procedia CIRP, 88, 612-617.

Anwar, A. B., & Pham, Q. C. (2018). Study of the spatter distribution on the powder bed during selective laser melting. Additive Manufacturing, 22, 86-97.

Arnold, C., Böhm, J., & Körner, C. (2019). In Operando Monitoring by Analysis of Backscattered Electrons during Electron Beam Melting. Advanced Engineering Materials, 1901102.

Bamberg, J., Zenzinger, G., Ladewig, A. (2016). In-process control of selective laser melting by quantitative optical tomography, 19th World Conference on Non-Destructive Testing, 2016

Barrett, C., Carradero, C., Harris, E., McKnight, J., Walker, J., MacDonald, E., & Conner, B. (2018a). Low cost, high speed stereovision for spatter tracking in laser powder bed fusion. In Solid freeform fabrication symposium.

Barrett, C., MacDonald, E., Conner, B., & Persi, F. (2018b). Micron-level layer-wise surface profilometry to detect porosity defects in powder bed fusion of Inconel 718. JOM, 70(9), 1844-1852.

Barrett, C., Carradero, C., Harris, E., Rogers, K., MacDonald, E., & Conner, B. (2019). Statistical analysis of spatter velocity with high-speed stereovision in laser powder bed fusion. Progress in Additive Manufacturing, 4(4), 423-430.

Bartlett, J. L., Heim, F. M., Murty, Y. V., & Li, X. (2018). In situ defect detection in selective laser melting via full-field infrared thermography. Additive Manufacturing, 24, 595-605.

Baumgartl, H., Tomas, J., Buettner, R., & Merkel, M. (2020). A deep learning-based model for defect detection in laser-powder bed fusion using in-situ thermographic monitoring. Progress in Additive Manufacturing, 1-9.

Bayle, F., & Doubenskaia, M. (2008, January). Selective laser melting process monitoring with high speed infra-red camera and pyrometer. In Fundamentals of laser assisted micro-and nanotechnologies (Vol. 6985, p. 698505). International Society for Optics and Photonics.

Berumen, S., Bechmann, F., Lindner, S., Kruth, J. P., & Craeghs, T. (2010). Quality control of laser-and powder bed-based Additive Manufacturing (AM) technologies. Physics procedia, 5, 617-622.

Bidare, P., Bitharas, I., Ward, R. M., Attallah, M. M., & Moore, A. J. (2018a). Fluid and particle dynamics in laser powder bed fusion. Acta Materialia, 142, 107-120.

Bidare, P., Bitharas, I., Ward, R. M., Attallah, M. M., & Moore, A. J. (2018b). Laser powder bed fusion in high-pressure atmospheres. The International Journal of Advanced Manufacturing Technology, 99(1-4), 543-555.

Bidare, P., Maier, R. R. J., Beck, R. J., Shephard, J. D., & Moore, A. J. (2017). An open-architecture metal powder bed fusion system for in-situ process measurements. Additive Manufacturing, 16, 177-185.

Bisht, M., Ray, N., Verbist, F., & Coeck, S. (2018). Correlation of selective laser melting-melt pool events with the tensile properties of Ti-6Al-4V ELI processed by laser powder bed fusion. Additive Manufacturing, 22, 302-306.

Bobel, A., Hector Jr, L. G., Chelladurai, I., Sachdev, A. K., Brown, T., Poling, W. A., ... & Greco, A. (2019). In situ synchrotron X-ray imaging of 4140 steel laser powder bed fusion. Materialia, 6, 100306.

Bond, L. J., Koester, L. W., & Taheri, H. (2019, March). NDE in-process for metal parts fabricated using powder based additive manufacturing. In Smart Structures and NDE for Energy Systems and Industry 4.0 (Vol. 10973, p. 1097302). International Society for Optics and Photonics.

Boone, N., Zhu, C., Smith, C., Todd, I., & Willmott, J. R. (2018). Thermal near infrared monitoring system for electron beam melting with emissivity tracking. Additive Manufacturing, 22, 601-605.

Bornoff, R., & Parry, J. (2015, March). An additive design heatsink geometry topology identification and optimisation algorithm. In 2015 31st Thermal Measurement, Modeling & Management Symposium (SEMI-THERM) (pp. 303-308). IEEE.

Bruna-Rosso, C., Demir, A. G., & Previtali, B. (2018). Selective laser melting finite element modeling: Validation with high-speed imaging and lack of fusion defects prediction. Materials & Design, 156, 143-153.

Calta, N. P., Martin, A. A., Hammons, J. A., Nielsen, M. H., Roehling, T. T., Fezzaa, K., ... & Lee, J. R. (2020). Pressure dependence of the laser-metal interaction under laser powder bed fusion conditions probed by in situ X-ray imaging. Additive Manufacturing, 32, 101084.

Calta, N. P., Wang, J., Kiss, A. M., Martin, A. A., Depond, P. J., Guss, G. M., ... & Tassone, C. J. (2018). An instrument for in situ time-resolved X-ray imaging and diffraction of laser powder bed fusion additive manufacturing processes. Review of Scientific Instruments, 89(5), 055101.

Caltanissetta, F., Grasso, M., Petro, S., & Colosimo, B. M. (2018). Characterization of in-situ measurements based on layerwise imaging in laser powder bed fusion. Additive Manufacturing, 24, 183-199.

Chandrasekar, S., Coble, J. B., Yoder, S., Nandwana, P., Dehoff, R. R., Paquit, V. C., & Babu, S. S. (2020). Investigating the effect of metal powder recycling in Electron beam Powder Bed Fusion using process log data. Additive Manufacturing, 32, 100994.

Chen, L., Yao, X., Xu, P., Moon, S. K., & Bi, G. (2020, April). Surface Monitoring for Additive Manufacturing with in-situ Point Cloud Processing. In 2020 6th International Conference on Control, Automation and Robotics (ICCAR) (pp. 196-201). IEEE.

Chen, Z., Zong, X., Shi, J., & Zhang, X. (2018). Online monitoring based on temperature field features and prediction model for selective laser sintering process. Applied Sciences, 8(12), 2383.

Chivel, Y. (2013). Optical in-process temperature monitoring of selective laser melting. Physics Procedia, 41, 904-910.

Colosimo, B. M., Grasso, M. (2020), Chapter 13: On-machine measurement, monitoring and control, in Precision Metal Additive Manufacturing. CRC Press

Colosimo, B. M., & Grasso, M. (2018). Spatially weighted PCA for monitoring video image data with application to additive manufacturing. Journal of Quality Technology, 50(4), 391-417.

Colosimo, B. M., Cavalli, S., & Grasso, M. (2020). A cost model for the economic evaluation of in-situ monitoring tools in metal additive manufacturing. International Journal of Production Economics, 223, 107532.

Colosimo, B. M., Grossi, E., Caltanissetta, F., & Grasso, M. (2020). Penelope: A Novel Prototype for In Situ Defect Removal in LPBF. JOM, 1-8.

Colosimo, B. M. (2018). Modeling and monitoring methods for spatial and image data. Quality Engineering, 30(1), 94-111.

Colosimo, B. M., Huang, Q., Dasgupta, T., & Tsung, F. (2018). Opportunities and challenges of quality engineering for additive manufacturing. Journal of Quality Technology, 50(3), 233-252.

Colosimo, B. M. (2020). Quality Monitoring and Control in Additive Manufacturing. Wiley StatsRef: Statistics Reference Online, 1-7

Cordero, P. M., Mireles, J., Ridwan, S., & Wicker, R. B. (2017). Evaluation of monitoring methods for electron beam melting powder bed fusion additive manufacturing technology. Progress in Additive Manufacturing, 2(1-2), 1-10.

Craeghs, T., Bechmann, F., Berumen, S., & Kruth, J. P. (2010). Feedback control of Layerwise Laser Melting using optical sensors. Physics Procedia, 5, 505-514.

Craeghs, T., Clijsters, S., Kruth, J. P., Bechmann, F., & Ebert, M. C. (2012). Detection of process failures in layerwise laser melting with optical process monitoring. Physics Procedia, 39, 753-759.

Craeghs, T., Clijsters, S., Yasa, E., Bechmann, F., Berumen, S., & Kruth, J. P. (2011). Determination of geometrical factors in Layerwise Laser Melting using optical process monitoring. Optics and Lasers in Engineering, 49(12), 1440-1446.

Dehoff, R. R., Kirka, M. M., Ellis, E., Paquit, V. C., Nandwana, P., & Plotkowski, A. J. (2019). Electron Beam Melting Technology Improvements (No. ORNL/TM-2019/1092). Oak Ridge National Lab.(ORNL), Oak Ridge, TN (United States).

Dehoff, R. R., Kirka, M. M., Sames, W. J., Bilheux, H., Tremsin, A. S., Lowe, L. E., & Babu, S. S. (2015). Site specific control of crystallographic grain orientation through electron beam additive manufacturing. Materials Science and Technology, 31(8), 931-938.

Demir, A. G., Mazzoleni, L., Caprio, L., Pacher, M., & Previtali, B. (2019). Complementary use of pulsed and continuous wave emission modes to stabilize melt pool geometry in laser powder bed fusion. Optics & Laser Technology, 113, 15-26.

Demir, A.G., De Giorgi, C., & Previtali, B. (2018). Design and implementation of a multisensor coaxial monitoring system with correction strategies for selective laser melting of a maraging steel. Journal of Manufacturing Science and Engineering, 140(4).

Demir, A. G., & Previtali, B. (2017). Investigation of remelting and preheating in SLM of 18Ni300 maraging steel as corrective and preventive measures for porosity reduction. The International Journal of Advanced Manufacturing Technology, 93(5-8), 2697-2709.

DePond, P. J., Guss, G., Ly, S., Calta, N. P., Deane, D., Khairallah, S., & Matthews, M. J. (2018). In situ measurements of layer roughness during laser powder bed fusion additive manufacturing using low coherence scanning interferometry. Materials & Design, 154, 347-359.

Dickins, A., Widjanarko, T., Sims-Waterhouse, D., Thompson, A., Lawes, S., & LEACH, R. Multi-view fringe projection system for surface topography measurement during metal powder bed fusion.

Doubenskaia, M., Pavlov, M., Grigoriev, S., Tikhonova, E., & Smurov, I. (2012). Comprehensive optical monitoring of selective laser melting. Journal of Laser Micro Nanoengineering, 7(3), 236-243.

Doubenskaia, M. A., Zhirnov, I. V., Teleshevskiy, V. I., Bertrand, P., & Smurov, I. Y. (2015). Determination of true temperature in selective laser melting of metal powder using infrared camera. In Materials science forum (Vol. 834, pp. 93-102). Trans Tech Publications Ltd.

Dowling, L., Kennedy, J., O'Shaughnessy, S., & Trimble, D. (2020). A review of critical repeatability and reproducibility issues in powder bed fusion. Materials & Design, 186, 108346.

Druzgalski, C. L., Ashby, A., Guss, G., King, W. E., Roehling, T. T., & Matthews, M. J. (2020). Process optimization of complex geometries using feed forward control for laser powder bed fusion additive manufacturing. Additive Manufacturing, 101169.

Dryburgh, P., Patel, R., Pieris, D. M., Hirsch, M., Li, W., Sharples, S. D., ... & Clark, M. (2019, May). Spatially resolved acoustic spectroscopy for texture imaging in powder bed fusion nickel superalloys. In AIP Conference Proceedings (Vol. 2102, No. 1, p. 020004). AIP Publishing LLC.

Dunbar, A. J., & Nassar, A. R. (2018). Assessment of optical emission analysis for in-process monitoring of powder bed fusion additive manufacturing. Virtual and Physical Prototyping, 13(1), 14-19.

Dunbar, A. J., Denlinger, E. R., Heigel, J., Michaleris, P., Guerrier, P., Martukanitz, R., & Simpson, T. W. (2016). Development of experimental method for in situ distortion and temperature measurements during the laser powder bed fusion additive manufacturing process. Additive Manufacturing, 12, 25-30.

Elwarfalli, H., Papazoglou, D., Erdahl, D., Doll, A., & Speltz, J. (2019, July). In Situ Process Monitoring for Laser-Powder Bed Fusion using Convolutional Neural Networks and Infrared Tomography. In 2019 IEEE National Aerospace and Electronics Conference (NAECON) (pp. 323-327). IEEE.

Erler, M., Streek, A., Schulze, C., Exner, H. (2014). Novel machine and measurement concept for micro machining by Selective Laser Sintering, Solid Freeform Fabrication Symposium, 2014

Eschner, E., Staudt, T., & Schmidt, M. (2019). 3D particle tracking velocimetry for the determination of temporally resolved particle trajectories within laser powder bed fusion of metals. International Journal of Extreme Manufacturing, 1(3), 035002.

Eschner, E., Staudt, T., & Schmidt, M. (2020a). Behavior and process zone formation in powder bed fusion of metals. CIRP Annals.

Eschner, N., Weiser, L., Häfner, B., & Lanza, G. (2020b). Classification of Specimen Density in Laser Powder Bed Fusion (L-PBF) Using In-process Structure-borne Acoustic Process Emissions. Additive Manufacturing, 101324.

Evans, R., Walker, J., Middendorf, J., & Gockel, J. (2020), Modeling and Monitoring of the Effect of Scan Strategy on Microstructure in Additive Manufacturing, The Minerals, Metals & Materials Society and ASM International 2020

Everton, S. K., Hirsch, M., Stravroulakis, P., Leach, R. K., & Clare, A. T. (2016). Review of in-situ process monitoring and in-situ metrology for metal additive manufacturing. Materials & Design, 95, 431-445.

Fisher, B. A., Lane, B., Yeung, H., & Beuth, J. (2018). Toward determining melt pool quality metrics via coaxial monitoring in laser powder bed fusion. Manufacturing letters, 15, 119-121.

Fleming, T. G., Nestor, S. G., Allen, T. R., Boukhaled, M. A., Smith, N. J., & Fraser, J. M. (2020). Tracking and controlling the morphology evolution of 3D powder-bed fusion in situ using inline coherent imaging. Additive Manufacturing, 32, 100978.

Forien, J. B., Calta, N. P., DePond, P. J., Guss, G. M., Roehling, T. T., & Matthews, M. J. (2020). Detecting keyhole pore defects and monitoring process signatures during laser powder bed fusion: a correlation between in situ pyrometry and ex situ X-ray radiography. Additive Manufacturing, 101336.

Foster, B. K., Reutzel, E. W., Nassar, A. R., Hall, B. T., Brown, S. W., & Dickman, C. J. (2015) Optical, layerwise monitoring of powder bed fusion. In Solid Free. Fabr. Symp. Proc, 295-307.

Foster, S. J., Carver, K., Dinwiddie, R. B., List, F., Unocic, K. A., Chaudhary, A., & Babu, S. S. (2018). Process-defect-structure-property correlations during laser powder bed fusion of alloy 718: role of in situ and ex situ characterizations. Metallurgical and Materials Transactions A, 49(11), 5775-5798.

Fox, J. C., Lane, B. M., & Yeung, H. (2017, May). Measurement of process dynamics through coaxially aligned high speed near-infrared imaging in laser powder bed fusion additive manufacturing. In Thermosense: Thermal Infrared Applications XXXIX (Vol. 10214, p. 1021407). International Society for Optics and Photonics.

Gaikwad, A., Imani, F., Rao, P., Yang, H., & Reutzel, E. (2019, June). Design Rules and In-Situ Quality Monitoring of Thin-Wall Features Made Using Laser Powder Bed Fusion. In International Manufacturing Science and Engineering Conference (Vol. 58745, p. V001T01A039). American Society of Mechanical Engineers.

Gaikwad, A., Yavari, R., Montazeri, M., Cole, K., Bian, L., & Rao, P. (2020). Toward the digital twin of additive manufacturing: Integrating thermal simulations, sensing, and analytics to detect process faults. IISE Transactions, 1-14.

Gibson, I., Rosen, D., Stucker, B., & Khorasani, M. (2014). Additive manufacturing technologies (Vol. 17, p. 195). New York: Springer.

Gobert, C., Reutzel, E. W., Petrich, J., Nassar, A. R., & Phoha, S. (2018). Application of supervised machine learning for defect detection during metallic powder bed fusion additive manufacturing using high resolution imaging. Additive Manufacturing, 21, 517-528.

Goh, G. D., Sing, S. L., & Yeong, W. Y. (2021). A review on machine learning in 3D printing: Applications, potential, and challenges. Artificial Intelligence Review, 54(1), 63-94.

Gold, S. A., Spears, T. G. (2018). Acoustic monitoring method for additive manufacturing processes." U.S. Patent No. 9,989,495

Gong, X., Cheng, B., Price, S., & Chou, K. (2013, November). Powder-bed electron-beam-melting additive manufacturing: powder characterization, process simulation and metrology. In Early Career Technical Conference, Birmingham, AL (pp. 55-66).

Grantham, S., Lane, B., Neira, J., Mekhontsev, S., Vlasea, M., & Hanssen, L. (2016, May). Optical design and initial results from NIST's AMMT/TEMPS facility. In Laser 3D Manufacturing III (Vol. 9738, p. 97380S). International Society for Optics and Photonics.

Grasso, M., & Colosimo, B. M. (2017). Process defects and in situ monitoring methods in metal powder bed fusion: a review. Measurement Science and Technology, 28(4), 044005.

Grasso, M., Demir, A. G., Previtali, B., & Colosimo, B. M. (2018a). In situ monitoring of selective laser melting of zinc powder via infrared imaging of the process plume. Robotics and Computer-Integrated Manufacturing, 49, 229-239.

Grasso, M., Gallina, F., & Colosimo, B. M. (2018b). Data fusion methods for statistical process monitoring and quality characterization in metal additive manufacturing. Procedia CIRP, 75, 103-107.

Grasso, M., Colosimo, B.M. (2019), A Statistical Learning Method for Image-based Monitoring of the Plume Signature in Laser Powder Bed Fusion, Robotics and Computer-Integrated Manufacturing, 57, 103-115

Grasso, M., Valsecchi, G., & Colosimo, B. M. (2020). Powder bed irregularity and hot-spot detection in Electron Beam Melting by means of in-situ video imaging. Manufacturing Letters. 24, 47-51.

Guo, Q., Zhao, C., Escano, L. I., Young, Z., Xiong, L., Fezzaa, K., ... & Chen, L. (2018). Transient dynamics of powder spattering in laser powder bed fusion additive manufacturing process revealed by in-situ high-speed high-energy X-ray imaging. Acta Materialia, 151, 169-180.

Guo, Q., Zhao, C., Qu, M., Xiong, L., Escano, L. I., Hojjatzadeh, S. M. H., ... & Chen, L. (2019). In-situ characterization and quantification of melt pool variation under constant input energy density in laser powder bed fusion additive manufacturing process. Additive Manufacturing, 28, 600-609.

Guo, Q., Zhao, C., Qu, M., Xiong, L., Hojjatzadeh, S. M. H., Escano, L. I., ... & Chen, L. (2020). In-situ full-field mapping of melt flow dynamics in laser metal additive manufacturing. Additive Manufacturing, 31, 100939.

Haines, M. P., Peter, N. J., Babu, S. S., & Jägle, E. A. (2020). In-situ synthesis of oxides by reactive process atmospheres during L-PBF of stainless steel. Additive Manufacturing, 33, 101178.

Hanssen, L. M., Mekhontsev, S. N., & Khromchenko, V. B. (2004, April). Infrared spectral emissivity characterization facility at NIST. In Thermosense XXVI (Vol. 5405, pp. 1-12). International Society for Optics and Photonics.

He, P., Zhong, K., Liu, X., Zhou, G., Wang, C., Wei, Q., ... & Li, Z. (2019, October). A phase-guided method for extracting the contour of the fusion area in laser powder bed fusion. In Seventh International Conference on Optical and Photonic Engineering (icOPEN 2019) (Vol. 11205, p. 112051H). International Society for Optics and Photonics.

Heeling, T., & Wegener, K. (2018). The effect of multi-beam strategies on selective laser melting of stainless steel 316L. Additive Manufacturing, 22, 334-342.

Hehr, A., Norfolk, M., Kominsky, D., Boulanger, A., Davis, M., & Boulware, P. (2020). Smart Build-Plate for Metal Additive Manufacturing Processes. Sensors, 20(2), 360.

Heigel, J. C., Lane, B. M., & Levine, L. E. (2020). In situ measurements of melt-pool length and cooling rate during 3D builds of the metal AM-Bench artifacts. Integrating Materials and Manufacturing Innovation, 9(1), 31-53.

Heigel, J. C., Lane, B., Levine, L., Phan, T., & Whiting, J. (2020). In Situ Thermography of the Metal Bridge Structures Fabricated for the 2018 Additive Manufacturing Benchmark Test Series (AM-Bench 2018). Journal Of Research Of The National Institute Of Standards And Technology, 125.

Hendriks, A., Ramokolo, R., Ngobeni, C., Moroko, M., & Naidoo, D. (2019, March). Layer-wise powder deposition defect detection in additive manufacturing. In Laser 3D Manufacturing VI (Vol. 10909, p. 109090O). International Society for Optics and Photonics.

Hirsch, M., Catchpole-Smith, S., Patel, R., Marrow, P., Li, W., Tuck, C., ... & Clare, A. T. (2017). Meso-scale defect evaluation of selective laser melting using spatially resolved acoustic spectroscopy. Proceedings of the Royal Society A: Mathematical, Physical and Engineering Sciences, 473(2205), 20170194.

Hirsch, M., Patel, R., Li, W., Guan, G., Leach, R. K., Sharples, S. D., & Clare, A. T. (2017). Assessing the capability of in-situ nondestructive analysis during layer based additive manufacture. Additive Manufacturing, 13, 135-142.

Hooper, P. A. (2018). Melt pool temperature and cooling rates in laser powder bed fusion. Additive Manufacturing, 22, 548-559.

Hossain, M. S., Mireles, J., Morton, P., Lin, Y., Terrazas, C. A., & Wicker, R. B. (2018). Part re-registration during process interruption of electron beam melting additive manufacturing. The International Journal of Advanced Manufacturing Technology, 96(1-4), 337-344.

Huang, Y., Leu, M. C., Mazumder, J., & Donmez, A. (2015). Additive manufacturing: current state, future potential, gaps and needs, and recommendations. Journal of Manufacturing Science and Engineering, 137(1).

Ian Gibson, I. G. (2015). Additive Manufacturing Technologies 3D Printing, Rapid Prototyping, and Direct Digital Manufacturing.

Imani, F., Chen, R., Diewald, E., Reutzel, E., & Yang, H. (2019). Deep learning of variant geometry in layerwise imaging profiles for additive manufacturing quality control. Journal of Manufacturing Science and Engineering, 141(11).

Imani, F., Chen, R., Diewald, E., Reutzel, E., & Yang, H. (2019, June). Image-Guided Variant Geometry Analysis of Layerwise Build Quality in Additive Manufacturing. In International Manufacturing Science and Engineering Conference (Vol. 58745, p. V001T02A041). American Society of Mechanical Engineers.

Jalalahmadi, B., Liu, J., Rios, J., Slotwinski, J., Peitsch, C., Goldberg, A., & Montalbano, T. (2019). In-process defect monitoring and correction in additive manufacturing of aluminum alloys.

Jayasinghe, S., Paoletti, P., Sutcliffe, C., Dardis, J., Jones, N., & Green, P. (2020). Automatic quality assessments of laser powder bed fusion builds from photodiode sensor measurements.

Kalms, M., Narita, R., Thomy, C., Vollertsen, F., & Bergmann, R. B. (2019). New approach to evaluate 3D laser printed parts in powder bed fusion-based additive manufacturing in-line within closed space. Additive Manufacturing, 26, 161-165.

Kanko, J. A., Sibley, A. P., & Fraser, J. M. (201)6. In situ morphology-based defect detection of selective laser melting through inline coherent imaging. Journal of Materials Processing Technology, 231, 488-500.

Khanzadeh, M., Chowdhury, S., Marufuzzaman, M., Tschopp, M. A., & Bian, L. (2018). Porosity prediction: Supervised-learning of thermal history for direct laser deposition. Journal of manufacturing systems, 47, 69-82.

Kim, H., Lin, Y., & Tseng, T. L. B. (2018). A review on quality control in additive manufacturing. Rapid Prototyping Journal. 24 (3), 645–669, 2018, doi: 10.1108/RPJ-03-2017-0048.

King, W. E., Anderson, A. T., Ferencz, R. M., Hodge, N. E., Kamath, C., Khairallah, S. A., & Rubenchik, A. M. (2015). Laser powder bed fusion additive manufacturing of metals; physics, computational, and materials challenges. Applied Physics Reviews, 2(4), 041304.

Kleszczynski, S., zur Jacobsmühlen, J., Reinarz, B., Sehrt, J. T., Witt, G., & Merhof, D. (2014). Improving process stability of laser beam melting systems. In Proceedings of the Frauenhofer Direct Digital Manufacturing Conference.

Kleszczynski, S., zur Jacobsmühlen, J., Sehrt, J. T., & Witt, G. (2012). Error detection in laser beam melting systems by high resolution imaging. In Proceedings of the Solid Freeform Fabrication Symposium.

Koester, L. W., Taheri, H., Bond, L. J., & Faierson, E. J. (2019, May). Acoustic monitoring of additive manufacturing for damage and process condition determination. In AIP Conference Proceedings (Vol. 2102, No. 1, p. 020005). AIP Publishing LLC.

Kolb, T., Elahi, R., Seeger, J., Soris, M., Scheitler, C., Hentschel, O., ... & Schmidt, M. (2020). Camera signal dependencies within coaxial melt pool monitoring in laser powder bed fusion. Rapid Prototyping Journal.

Körner, C. (2016). Additive manufacturing of metallic components by selective electron beam melting—a review. International Materials Reviews, 61(5), 361-377.

Kouprianoff, D., Luwes, N., Yadroitsava, I., Yadroitsev, I., (2018), Acoustic emission technique for online detection of dusione defects for single tracks during metal laser powder bed fusion, Solid Freeform Fabrication 2018

Krauss, H., Eschey, C., & Zaeh, M. (2012, August). Thermography for monitoring the selective laser melting process. In Proceedings of the solid freeform fabrication symposium (pp. 999-1014).

Krauss, H., Zeugner, T., & Zaeh, M. F. (2014). Layerwise monitoring of the selective laser melting process by thermography. Physics Procedia, 56, 64-71.

Kruth, J. P., Mercelis, P., Van Vaerenbergh, J., & Craeghs, T. (2007). Feedback control of selective laser melting. In Proceedings of the 3rd international conference on advanced research in virtual and rapid prototyping (pp. 521-527).

Kwon, O., Kim, H. G., Ham, M. J., Kim, W., Kim, G. H., Cho, J. H., ... & Kim, K. (2020). A deep neural network for classification of melt-pool images in metal additive manufacturing. Journal of Intelligent Manufacturing, 31(2), 375-386.

Land II, W. S., Zhang, B., Ziegert, J., & Davies, A. (2015). In-situ metrology system for laser powder bed fusion additive process. Procedia Manufacturing, 1, 393-403.

Lane, B., & Yeung, H. (2019). Process Monitoring Dataset from the Additive Manufacturing Metrology Testbed (AMMT):" Three-Dimensional Scan Strategies". Journal of Research of the National Institute of Standards and Technology, 124, 1-14.

Lane, B., Grantham, S., Yeung, H., Zarobila, C., & Fox, J. (2017, August). Performance characterization of process monitoring sensors on the NIST Additive Manufacturing Metrology Testbed. In Solid Free Fabr Symp.

Lane, B., Heigel, J., Ricker, R., Zhirnov, I., Khromschenko, V., Weaver, J., ... & Levine, L. (2020). Measurements of melt pool geometry and cooling rates of individual laser traces on IN625 bare plates. Integrating Materials and Manufacturing Innovation, 1-15.

Lane, B., Mekhontsev, S., Grantham, S., Vlasea, M., Whiting, J., Yeung, H., ... & Hanssen, L. (2016a). Design, developments, and results from the NIST additive manufacturing metrology testbed (AMMT). In Solid freeform fabrication symposium, Austin, TX (pp. 1145-1160).

Lane, B., Moylan, S., Whitenton, E. P., & Ma, L. (2016b). Thermographic measurements of the commercial laser powder bed fusion process at NIST. Rapid prototyping journal.

Lane, B., Whitenton, E., Madhavan, V., & Donmez, A. (2013). Uncertainty of temperature measurements by infrared thermography for metal cutting applications. Metrologia, 50(6), 637.

Leach, R.K. (2020), Integrated metrology -10-year roadmap for advanced manufacturing, HVM Catapult, https://bit.ly/3b8dT84

Leach, R.K., & Carmignato, S. (Eds.). (2020). Precision Metal Additive Manufacturing. CRC Press.

Lee, Y. S., Kirka, M. M., Dinwiddie, R. B., Raghavan, N., Turner, J., Dehoff, R. R., & Babu, S. S. (2018). Role of scan strategies on thermal gradient and solidification rate in electron beam powder bed fusion. Additive Manufacturing, 22, 516-527.

Leung, C. L. A., Marussi, S., Atwood, R. C., Towrie, M., Withers, P. J., & Lee, P. D. (2018). In situ X-ray imaging of defect and molten pool dynamics in laser additive manufacturing. Nature communications, 9(1), 1-9.

Leung, C. L. A., Marussi, S., Towrie, M., Atwood, R. C., Withers, P. J., & Lee, P. D. (2019). The effect of powder oxidation on defect formation in laser additive manufacturing. Acta Materialia, 166, 294-305.

Lhuissier, P., Bataillon, X., Maestre, C., Sijobert, J., Cabrol, E., Bertrand, P., ... & Martin, G. (2020). In situ 3D X-ray microtomography of laser-based powder-bed fusion (L-PBF)-A feasibility study. Additive Manufacturing, 101271.

Liu, Y., Yang, Y., Mai, S., Wang, D., & Song, C. (2015). Investigation into spatter behavior during selective laser melting of AISI 316L stainless steel powder. Materials & Design, 87, 797-806.

Liu, Y., Zhang, Z., Blunt, L., Saunby, G., Dawes, J., Blackham, B., ... & Jiang, X. (2019). In-situ inspection system for additive manufacturing based on phase measurement profilometry. In 19th International Conference of the European Society for Precision Engineering and Nanotechnology (pp. 324-327)

Liu, Y., Blunt, L., Zhang, Z., Rahman, H. A., Gao, F., & Jiang, X. (2020a). In-situ areal inspection of powder bed for electron beam fusion system based on fringe projection profilometry. Additive Manufacturing, 31, 100940.

Liu, C., Le Roux, L., Ji, Z., Kerfriden, P., Lacan, F., & Bigot, S. (2020b). Machine Learning-enabled feedback loops for metal powder bed fusion additive manufacturing. Procedia Computer Science, 176, 2586-2595.

Liu, Z., Li, T., Kim, H., Cong, W., Jiang, Q., & Zhang, H. C. (2020c). Recent Advances and Current Developments of Molten Pool Temperature Measurement for Laser Additive Manufacturing Processes. Recent Patents on Mechanical Engineering, 13(1), 13-23.

Lough, C. S., Wang, X., Landers, R. G., Bristow, D. A., Drallmeier, J. A., & Kinzel, E. C. (2019). In-situ Local Part Qualification of SLM 304L Stainless Steel through Voxel Based Processing of SWIR Imaging Data. measurements, 12, 14.

Lough, C. S., Escano, L. I., Qu, M., Smith, C. C., Landers, R. G., Bristow, D. A., ... & Kinzel, E. C. (2020a). In-situ optical emission spectroscopy of selective laser melting. Journal of Manufacturing Processes, 53, 336-341.

Lough, C. S., Wang, X., Smith, C. C., Landers, R. G., Bristow, D. A., Drallmeier, J. A., ... & Kinzel, E. C. (2020b). Correlation of SWIR imaging with LPBF 304 L stainless steel part properties. Additive Manufacturing, 101359.

Lu, Q. Y., Nguyen, N. V., Hum, A. J. W., Tran, T., & Wong, C. H. (2019). Optical in-situ monitoring and correlation of density and mechanical properties of stainless steel parts produced by selective laser melting process based on varied energy density. Journal of Materials Processing Technology, 271, 520-531.

Lu, Q. Y., Nguyen, N. V., Hum, A. J. W., Tran, T., & Wong, C. H. (2020). Identification and evaluation of defects in selective laser melted 316L stainless steel parts via in-situ monitoring and micro computed tomography. Additive Manufacturing, 35, 101287.

Ludwig, S. (2020). Instrumented Build Plate for in-situ Stress Monitoring and Crack Detection during the Laser Powder Bed Fusion Additive Manufacturing Process (Doctoral dissertation, The University of North Carolina at Charlotte).

Ly, S., Rubenchik, A. M., Khairallah, S. A., Guss, G., & Matthews, M. J. (2017). Metal vapor micro-jet controls material redistribution in laser powder bed fusion additive manufacturing. Scientific reports, 7(1), 1-12.

Mani, M., Feng, S., Lane, B., Donmez, A., Moylan, S., & Fesperman, R. (2015). Measurement science needs for real-time control of additive manufacturing powder bed fusion processes.

Northeast, M. D., Mansell, J., Jones, N. (2018), Acoustic emission sensing in powder bed Additive Manufacturing, European Patent Application, EP 3 590 631 A1

Mahmoudi, M., Ezzat, A. A., & Elwany, A. (2019). Layerwise anomaly detection in laser powder-bed fusion metal additive manufacturing. Journal of Manufacturing Science and Engineering, 141(3).

Martin, A. A., Calta, N. P., Hammons, J. A., Khairallah, S. A., Nielsen, M. H., Shuttlesworth, R. M., ... & Lee, J. R. (2019). Ultrafast dynamics of laser-metal interactions in additive manufacturing alloys captured by in situ X-ray imaging. Materials Today Advances, 1, 100002.

Meng, L. (2020). Machine Learning And Probabilistic Design Framework For Laser Powder Bed Fusion Process (Doctoral dissertation, Purdue University Graduate School).

Meng, L., McWilliams, B., Jarosinski, W., Park, H. Y., Jung, Y. G., Lee, J., & Zhang, J. (2020). Machine Learning in Additive Manufacturing: A Review. JOM, 1-15.

Mireles, J., Terrazas, C., Gaytan, S. M., Roberson, D. A., & Wicker, R. B. (2015). Closed-loop automatic feedback control in electron beam melting. The International Journal of Advanced Manufacturing Technology, 78(5-8), 1193-1199.

Mitchell, J. A., Ivanoff, T. A., Dagel, D., Madison, J. D., & Jared, B. (2020). Linking pyrometry to porosity in additively manufactured metals. Additive Manufacturing, 31, 100946.

Miyagi, M., & Wang, J. (2020). Keyhole dynamics and morphology visualized by in-situ X-ray imaging in laser melting of austenitic stainless steel. Journal of Materials Processing Technology, 116673.

Mohr, G., Altenburg, S. J., Ulbricht, A., Heinrich, P., Baum, D., Maierhofer, C., & Hilgenberg, K. (2020). In-Situ Defect Detection in Laser Powder Bed Fusion by Using Thermography and Optical Tomography—Comparison to Computed Tomography. Metals, 10(1), 103.

Montazeri, M., & Rao, P. (2018). Sensor-based build condition monitoring in laser powder bed fusion additive manufacturing process using a spectral graph theoretic approach. Journal of Manufacturing Science and Engineering, 140(9).

Montazeri, M., Nassar, A. R., Dunbar, A. J., & Rao, P. (2020). In-process monitoring of porosity in additive manufacturing using optical emission spectroscopy. IISE Transactions, 52(5), 500-515.

Morgan, J. P., Morgan Jr, J. P., Natale, D. J., Smith, R. W., Mitchell, W. F., Dunbar, A. J., & Reutzel, E. W. (2017). Selection and Installation of High Resolution Imaging to Monitor the PBFAM Process, and Synchronization to Post-Build 3D Computed Tomography. In Proceedings of the 28th Annual International Solid Freeform Fabrication Symposium–An Additive Manufacturing Conference (pp. 1382-1399).

Moylan, S., Whitenton, E., Lane, B., & Slotwinski, J. (2014, February). Infrared thermography for laser-based powder bed fusion additive manufacturing processes. In AIP Conference Proceedings (Vol. 1581, No. 1, pp. 1191-1196). American Institute of Physics.

Nadipalli, V. K., Andersen, S. A., Nielsen, J. S., & Pedersen, D. B. (2019). Considerations for interpreting in-situ photodiode sensor data in pulsed mode laser powder bed fusion. In Joint Special Interest Group meeting between euspen and ASPE Advancing Precision in Additive Manufacturing (pp. 66-69). The European Society for Precision Engineering and Nanotechnology.

Nandwana, P., Kirka, M. M., Paquit, V. C., Yoder, S., & Dehoff, R. R. (2018). Correlations between powder feedstock quality, in situ porosity detection, and fatigue behavior of Ti-6Al-4V fabricated by powder bed electron beam melting: a step towards qualification. Jom, 70(9), 1686-1691.

Nassar, A. R., Gundermann, M. A., Reutzel, E. W., Guerrier, P., Krane, M. H., & Weldon, M. J. (2019). Formation processes for large ejecta and interactions with melt pool formation in powder bed fusion additive manufacturing. Scientific reports, 9(1), 1-11.

Neef, A., Seyda, V., Herzog, D., Emmelmann, C., Schönleber, M., & Kogel-Hollacher, M. (2014). Low coherence interferometry in selective laser melting. Physics Procedia, 56, 82-89.

Okaro, I. A., Jayasinghe, S., Sutcliffe, C., Black, K., Paoletti, P., & Green, P. L. (2019). Automatic fault detection for laser powder-bed fusion using semi-supervised machine learning. Additive Manufacturing, 27, 42-53.

Özel, T., Shaurya, A., Altay, A., & Yang, L. (2018). Process monitoring of meltpool and spatter for temporal-spatial modeling of laser powder bed fusion process. Procedia CIRP, 74, 102-106.

Pagani, L., Grasso, M., Scott, P. J., & Colosimo, B. M. (2020). Automated Layerwise Detection of Geometrical Distortions in Laser Powder Bed Fusion. Additive Manufacturing, 101435.

Paulson, N. H., Gould, B., Wolff, S. J., Stan, M., & Greco, A. (2020). Correlations between thermal history and keyhole porosity in laser powder bed fusion. Additive Manufacturing, 101213.

Peng, X., Kong, L., Chen, Y., Shan, Z., & Qi, L. (2020). Design of a Multi-sensor Monitoring System for Additive Manufacturing Process. Nanomanufacturing and Metrology, 1-9.

Peng, X., Kong, L., Chen, Y., Wang, J., & Xu, M. (2019, February). A preliminary study of in-situ defects measurement for additive manufacturing based on multi-spectrum. In 9th international symposium on advanced optical manufacturing and testing technologies: subdiffraction-limited plasmonic lithography and innovative manufacturing technology (Vol. 10842, p. 1084217). International Society for Optics and Photonics.

Plotnikov, Y., Henkel, D., Burdick, J., French, A., Sions, J., & Bourne, K. (2019, May). Infrared-assisted acoustic emission process monitoring for additive manufacturing. In AIP Conference Proceedings (Vol. 2102, No. 1, p. 020006). AIP Publishing LLC.

Pobel, C. R., Arnold, C., Osmanlic, F., Fu, Z., & Körner, C. (2019). Immediate development of processing windows for selective electron beam melting using layerwise monitoring via backscattered electron detection. Materials Letters, 249, 70-72.

Popov, V. V., Grilli, M. L., Koptyug, A., Jaworska, L., Katz-Demyanetz, A., Klobčar, D., ... & Goel, S. (2021). Powder Bed Fusion Additive Manufacturing Using Critical Raw Materials: A Review. Materials, 14(4), 909.

Price, S., Cooper, K., & Chou, K. (2012, August). Evaluations of temperature measurements by near-infrared thermography in powder-based electron-beam additive manufacturing. In Proceedings of the Solid Freeform Fabrication Symposium (pp. 761-773). University of Texas, Austin, TX.

Price, S., Lydon, J., Cooper, K., & Chou, K. (2014, November). Temperature measurements in powder-bed electron beam additive manufacturing. In ASME International Mechanical Engineering Congress and Exposition (Vol. 46438, p. V02AT02A002). American Society of Mechanical Engineers.

Qi, X., Chen, G., Li, Y., Cheng, X., & Li, C. (2019). Applying neural-network-based machine learning to additive manufacturing: current applications, challenges, and future perspectives. Engineering, 5(4), 721-729.

Raitanen, N., & Ylander, P. (2020). A Data-driven Approach Based on Statistical Learning Modeling for Process Monitoring and Quality Assurance of Metal Powder Additive Manufacturing. EOS, 1000, 290.

Raplee, J., Plotkowski, A., Kirka, M. M., Dinwiddie, R., Okello, A., Dehoff, R. R., & Babu, S. S. (2017). Thermographic microstructure monitoring in electron beam additive manufacturing. Scientific reports, 7, 43554.

Renishaw Plc., 'Metal additive manufacturing 1', pp. 1–24.

Renken, V., von Freyberg, A., Schünemann, K., Pastors, F., & Fischer, A. (2019). In-process closed-loop control for stabilising the melt pool temperature in selective laser melting. Progress in Additive Manufacturing, 4(4), 411-421.

Repossini, G., Laguzza, V., Grasso, M., & Colosimo, B. M. (2017). On the use of spatter signature for in-situ monitoring of Laser Powder Bed Fusion. Additive Manufacturing, 16, 35-48.

Ridwan, S., Mireles, J., Gaytan, S. M., Espalin, D., & Wicker, R. B. (2014). Automatic layerwise acquisition of thermal and geometric data of the electron beam melting process using infrared thermography. In Proc. Int. Symp. Solid Freeform Fabrication (Vol. 343).

Rieder, H., Dillhöfer, A., Spies, M., Bamberg, J., & Hess, T. (2014, October). Online monitoring of additive manufacturing processes using ultrasound. In Proceedings of the 11th European Conference on Non-Destructive Testing, October (pp. 6-10).

Rieder, H., Spies, M., Bamberg, J., & Henkel, B. (2016, June). On-and offline ultrasonic inspection of additively manufactured components. In 19th World Conference on Non-Destructive Testing (WCNDT), Munich, Germany, June (pp. 13-17).

Rodriguez, E., Medina, F., Espalin, D., Terrazas, C., Muse, D., Henry, C., ... & Wicker, R. B. (2012, August). Integration of a thermal imaging feedback control system in electron beam melting. In Proceedings of the Solid Freeform Fabrication Symposium.

Rodriguez, E., Mireles, J., Terrazas, C. A., Espalin, D., Perez, M. A., & Wicker, R. B. 2015. Approximation of absolute surface temperature measurements of powder bed fusion additive manufacturing technology using in situ infrared thermography. Additive Manufacturing, 5, 31-39

Samei, J., Amirmaleki, M., Dastgiri, M. S., Marinelli, C., & Green, D. E. (2019). In-situ X-ray tomography analysis of the evolution of pores during deformation of AlSi10Mg fabricated by selective laser melting. Materials Letters, 255, 126512.

Samei, J., Amirmaleki, M., Ventura, A. P., Pawlikowski, G. T., Bayes, M., Misiolek, W. Z., & Wilkinson, D. S. (2020). In-situ X-ray tomography analysis of the evolution of pores during deformation of a Cu-Sn alloy fabricated by selective laser melting. Additive Manufacturing, 34, 101196.

Schilp, J., Seidel, C., Krauss, H., & Weirather, J. (2014). Investigations on temperature fields during laser beam melting by means of process monitoring and multiscale process modelling. Advances in Mechanical Engineering, 6, 217584.

Schmeiser, F., Krohmer, E., Schell, N., Uhlmann, E., & Reimers, W. (2020). Experimental observation of stress formation during selective laser melting using in situ X-ray diffraction. Additive Manufacturing, 32, 101028.

Schwerdtfeger, J., Singer, R. F., & Körner, C. (2012). In situ flaw detection by IR-imaging during electron beam melting. Rapid Prototyping Journal, 18(4), 259-263.

Scime, L., & Beuth, J. (2018a). A multi-scale convolutional neural network for autonomous anomaly detection and classification in a laser powder bed fusion additive manufacturing process. Additive Manufacturing, 24, 273-286.

Scime, L., & Beuth, J. (2018b). Anomaly detection and classification in a laser powder bed additive manufacturing process using a trained computer vision algorithm. Additive Manufacturing, 19, 114-126.

Scime, L., & Beuth, J. (2019). Melt pool geometry and morphology variability for the Inconel 718 alloy in a laser powder bed fusion additive manufacturing process. Additive Manufacturing, 29, 100830.

Scime, L., Siddel, D., Baird, S., & Paquit, V. (2020). Layer-wise anomaly detection and classification for powder bed additive manufacturing processes: A machine-agnostic algorithm for real-time pixel-wise semantic segmentation. Additive Manufacturing, 101453.

Scott, S. P., Sutcliffe, C. (2015) Additive manufacturing apparatus and method. U.S. Patent No. 8,994,592

Shepard, S. M., Hou, Y., Ahmed, T., & Lhota, J. R. (2006). Reference-free interpretation of flash thermography data. Insight-Non-Destructive Testing and Condition Monitoring, 48(5), 298-301.

Shevchik, S. A., Masinelli, G., Kenel, C., Leinenbach, C., & Wasmer, K. (2019). Deep learning for in situ and real-time quality monitoring in additive manufacturing using acoustic emission. IEEE Transactions on Industrial Informatics, 15(9), 5194-5203.

Shrestha, S., & Chou, K. (2018). Single track scanning experiment in laser powder bed fusion process. Procedia Manufacturing, 26, 857-864.

Sing, S. L., An, J., Yeong, W. Y., & Wiria, F. E. (2016). Laser and electron-beam powder-bed additive manufacturing of metallic implants: A review on processes, materials and designs. Journal of Orthopaedic Research, 34(3), 369-385.

Sing, S. L., Huang, S., Goh, G. D., Goh, G. L., Tey, C. F., Tan, J. H. K., & Yeong, W. Y. (2021). Emerging Metallic Systems for Additive Manufacturing: In-situ Alloying and Multi-metal Processing in Laser Powder Bed Fusion. Progress in Materials Science, 100795.

Song, L., Wang, F., Li, S., & Han, X. (2017). Phase congruency melt pool edge extraction for laser additive manufacturing. Journal of Materials Processing Technology, 250, 261-269.

Spears, T. G., & Gold, S. A. (2016). In-process sensing in selective laser melting (SLM) additive manufacturing. Integrating Materials and Manufacturing Innovation, 5(1), 16-40.

Steed, C. A., Halsey, W., Dehoff, R., Yoder, S. L., Paquit, V., & Powers, S. (2017). Falcon: Visual analysis of large, irregularly sampled, and multivariate time series data in additive manufacturing. Computers & Graphics, 63, 50-64.

Syam, W. P., Rybalcenko, K., Gaio, A., Crabtree, J., & Leach, R. K. (2019). Methodology for the development of in-line optical surface measuring instruments with a case study for additive surface finishing. Optics and Lasers in Engineering, 121, 271-288.

Tan, Z., Fang, Q., Li, H., Liu, S., Zhu, W., & Yang, D. (2020). Neural network based image segmentation for spatter extraction during laser-based powder bed fusion processing. Optics & Laser Technology, 130, 106347.

Tan Phuc, L., Seita, M., (2019). A high-resolution and large field-of-view scanner for in-line characterization of powder bed defects during additive manufacturing. Materials & Design, 164, 107562.

Thijs, L., Verhaeghe, F., Craeghs, T., Van Humbeeck, J., & Kruth, J. P. (2010). A study of the microstructural evolution during selective laser melting of Ti–6Al–4V. Acta materialia, 58(9), 3303-3312.

Trapp, J., Rubenchik, A. M., Guss, G., & Matthews, M. J. (2017). In situ absorptivity measurements of metallic powders during laser powder-bed fusion additive manufacturing. Applied Materials Today, 9, 341-349.

Tsung, F., Zhang, K., Cheng, L., & Song, Z. (2018). Statistical transfer learning: A review and some extensions to statistical process control. Quality Engineering, 30(1), 115-128.

Uhlmann, E., Krohmer, E., Hohlstein, F., & Reimers, W. (2017). Development of an experimental test setup for in situ strain evaluation during selective laser melting. In

Proceedings of the 28th Annual International Solid Freeform Fabrication Symposium (pp. 1472-1480).

Vasileska, E., Demir, A. G., Colosimo, B. M., & Previtali, B. (2020). Layer-wise control of selective laser melting by means of inline melt pool area measurements. Journal of Laser Applications, 32(2), 022057.

Vora, H. D., & Sanyal, S. (2020). A comprehensive review: metrology in additive manufacturing and 3D printing technology. Progress in Additive Manufacturing, 1-35.

Wang, X., Lough, C. S., Bristow, D. A., Landers, R. G., & Kinzel, E. C. (2018). Effects of thermal camera resolution on feature extraction in selective laser melting. In Proceedings of Solid Freeform Fabrication Symposium.

Wang, C., Tan, X. P., Tor, S. B., & Lim, C. S. (2020a). Machine learning in additive manufacturing: State-of-the-art and perspectives. Additive Manufacturing, 101538.

Wang, Q., Michaleris, P. P., Nassar, A. R., Irwin, J. E., Ren, Y., & Stutzman, C. B. (2020b). Model-based feedforward control of laser powder bed fusion additive manufacturing. Additive Manufacturing, 31, 100985.

Wasmer, K., Le-Quang, T., Meylan, B., & Shevchik, S. A. (2019). In situ quality monitoring in AM using acoustic emission: A reinforcement learning approach. Journal of Materials Engineering and Performance, 28(2), 666-672.

Williams, R. J., Piglione, A., Rønneberg, T., Jones, C., Pham, M. S., Davies, C. M., & Hooper, P. A. (2019). In situ thermography for laser powder bed fusion: Effects of layer temperature on porosity, microstructure and mechanical properties. Additive Manufacturing, 30, 100880.

Wong, H., Neary, D., Jones, E., Fox, P., & Sutcliffe, C. (2019a). Pilot capability evaluation of a feedback electronic imaging system prototype for in-process monitoring in electron beam additive manufacturing. The International Journal of Advanced Manufacturing Technology, 100(1-4), 707-720.

Wong, H., Neary, D., Jones, E., Fox, P., & Sutcliffe, C. (2019b). Benchmarking spatial resolution in electronic imaging for potential in-situ Electron Beam Melting monitoring. Additive Manufacturing, 29, 100829.

Wong, H., Garrard, R., Black, K., Fox, P., & Sutcliffe, C. (2020). Material characterisation using electronic imaging for Electron Beam Melting process monitoring. Manufacturing Letters, 23, 44-48.

Wong, H. (2020). Bitmap generation from computer-aided design for potential layer-quality evaluation in electron beam additive manufacturing. Rapid Prototyping Journal.

Yadav, P., Rigo, O., Arvieu, C., Le Guen, E., & Lacoste, E. (2020). In Situ Monitoring Systems of The SLM Process: On the Need to Develop Machine Learning Models for Data Processing. Crystals, 10(6), 524.

Yadroitsev, I., Krakhmalev, P., & Yadroitsava, I. (2014). Selective laser melting of Ti6Al4V alloy for biomedical applications: Temperature monitoring and microstructural evolution. Journal of Alloys and Compounds, 583, 404-409.

Yan, H., Grasso, M., Paynabar, K., & Colosimo, B. M. (2020). Real-time Detection of Clustered Events in Video-imaging data with Applications to Additive Manufacturing. arXiv preprint arXiv:2004.10977.

Yang, Z., Lu, Y., Yeung, H., & Krishnamurty, S. (2019, August). Investigation of Deep Learning for Real-Time Melt Pool Classification in Additive Manufacturing. In 2019 IEEE 15th International Conference on Automation Science and Engineering (CASE) (pp. 640-647). IEEE.

Yang, D., Li, H., Liu, S., Song, C., Yang, Y., Shen, S., ... & Zhu, Y. (2020a). In situ capture of spatter signature of SLM process using maximum entropy double threshold image processing method based on genetic algorithm. Optics & Laser Technology, 131, 106371.

Yang, L., Lo, L., Ding, S., & Özel, T. (2020b). Monitoring and detection of meltpool and spatter regions in laser powder bed fusion of super alloy Inconel 625. Progress in Additive Manufacturing, 1-12.

Yasa, E., Kruth, J. P. and Deckers, J. (2011) Manufacturing by combining selective laser melting and selective laser erosion/laser re-melting CIRP Ann. Manuf. Technol. 60 263–6

Ye, D., Fuh, J. Y. H., Zhang, Y., Hong, G. S., & Zhu, K. (2018a). In situ monitoring of selective laser melting using plume and spatter signatures by deep belief networks. ISA transactions, 81, 96-104.

Ye, D., Hong, G. S., Zhang, Y., Zhu, K., & Fuh, J. Y. H. (2018b). Defect detection in selective laser melting technology by acoustic signals with deep belief networks. The International Journal of Advanced Manufacturing Technology, 96(5-8), 2791-2801.

Yeung, H., Lane, B. M., Donmez, M. A., & Moylan, S. (2020). In-situ calibration of laser/galvo scanning system using dimensional reference artefacts. CIRP Annals.

Yeung, H., & Lane, B. (2020). A residual heat compensation based scan strategy for powder bed fusion additive manufacturing. Manufacturing Letters, 25, 56-59.

Yim, S., & Rosen, D. (2012, August). Build time and cost models for additive manufacturing process selection. In International Design Engineering Technical Conferences and Computers and Information in Engineering Conference (Vol. 45011, pp. 375-382). American Society of Mechanical Engineers.

Yin, J., Wang, D., Yang, L., Wei, H., Dong, P., Ke, L., ... & Zeng, X. (2020). Correlation between forming quality and spatter dynamics in laser powder bed fusion. Additive Manufacturing, 31, 100958.

Yoder, S., Morgan, S., Kinzy, C., Barnes, E., Kirka, M., Paquit, V., ... & Babu, S. S. (2018). Characterization of topology optimized Ti-6Al-4V components using electron beam powder bed fusion. Additive Manufacturing, 19, 184-196.

Yoder, S., Nandwana, P., Paquit, V., Kirka, M., Scopel, A., Dehoff, R. R., & Babu, S. S. (2019). Approach to qualification using E-PBF in-situ process monitoring in Ti-6Al-4V. Additive Manufacturing, 28, 98-106.

Young, Z. A., Guo, Q., Parab, N. D., Zhao, C., Qu, M., Escano, L. I., ... & Chen, L. (2020). Types of spatter and their features and formation mechanisms in laser powder bed fusion additive manufacturing process. Additive Manufacturing, 101438.

Yuan, B., Giera, B., Guss, G., Matthews, I., & Mcmains, S. (2019, January). Semi-supervised convolutional neural networks for in-situ video monitoring of selective laser melting. In 2019 IEEE Winter Conference on Applications of Computer Vision (WACV) (pp. 744-753). IEEE.

Yuan, B., Guss, G. M., Wilson, A. C., Hau-Riege, S. P., DePond, P. J., McMains, S., ... & Giera, B. (2018).

Machine-learning-based monitoring of laser powder bed fusion. Advanced Materials Technologies, 3(12), 1800136.

Zhang, B., II, W. S. L., Ziegert, J., & Davies, A. (2015). In Situ Monitoring of Laser Powder Bed Fusion Additive Manufacturing Using Digital Fringe Projection Technique. In Proceedings: ASPE 2015 Spring Topical Meeting (pp. 47-52).

Zhang, B., Ziegert, C. J., Davies, A. (2016a), 'In situ surface metrology of laser powder bed fusion usig fringe projection', presented at the 2016 Summer Topical Meeting Dimensional Accuracy and Surface Finish in Additive Manufacturing, Raleigh, NC, USA, 2016.

Zhang, B., Ziegert, J., Farahi, F., & Davies, A. (2016b). In situ surface topography of laser powder bed fusion using fringe projection. Additive Manufacturing, 12, 100-107.

Zhang, Y., Hong, G. S., Ye, D., Zhu, K., & Fuh, J. Y. (2018). Extraction and evaluation of melt pool, plume and spatter information for powder-bed fusion AM process monitoring. Materials & Design, 156, 458-469.

Zhang, Y., Soon, H. G., Ye, D., Fuh, J. Y. H., & Zhu, K. (2019a). Powder-Bed Fusion Process Monitoring by Machine Vision With Hybrid Convolutional Neural Networks. IEEE Transactions on Industrial Informatics, 16(9), 5769-5779.

Zhang, Y., Fuh, J. Y., Ye, D., & Hong, G. S. (2019b). In-situ monitoring of laser-based PBF via off-axis vision and image processing approaches. Additive Manufacturing, 25, 263-274.

Zhao, C., Fezzaa, K., Cunningham, R. W., Wen, H., De Carlo, F., Chen, L., ... & Sun, T. (2017). Real-time monitoring of laser powder bed fusion process using high-speed X-ray imaging and diffraction. Scientific reports, 7(1), 1-11.

Zheng, H., Li, H., Lang, L., Gong, S., & Ge, Y. (2018). Effects of scan speed on vapor plume behavior and spatter generation in laser powder bed fusion additive manufacturing. Journal of Manufacturing Processes, 36, 60-67.

Zhirnov, I., Mekhontsev, S., Lane, B., Grantham, S., & Bura, N. (2020). Accurate determination of laser spot position during laser powder bed fusion process thermography. Manufacturing Letters, 23, 49-52.

zur Jacobsmühlen, J., Achterhold, J., Kleszczynski, S., Witt, G., & Merhof, D. (2019). In situ measurement of part geometries in layer images from laser beam melting processes. Progress in Additive Manufacturing, 4(2), 155-165.

zur Jacobsmühlen, J., Kleszczynski, S., Witt, G., & Merhof, D. (2015). Elevated region area measurement for quantitative analysis of laser beam melting process stability. In 26th International Solid Freeform Fabrication Symposium; Austin, TX (pp. 549-559).

Appendix – Literature collection procedure

This section describes the procedure applied to collect the literature reviewed in this study. The literature analysis covered the period 2007 to September 2020. The following methods have been applied:

1. Search by keyword: Google Scholar and Scopus databases where searched using several different combinations of salient keywords including the following: "L-PBF", "SLM", "EBM", "EB-PBF", "powder bed fusion", "in-situ", "in-process", "in-line" "online", "on-machine", "layerwise", "monitoring", "measurement", "sensing", "sensor", "metrology", "defect detection", "fault detection", "error detection", "anomaly detection", "machine learning", "artificial intelligence", "data mining", "statistical process control", "statistical process monitoring", "thermography", "imaging", "video-imaging", "machine vision", "camera", "photodiode", "pyrometer", "spectrometry", "fringe projection", "powder bed", "melt pool", "porosity", "distortion", "geometric error", "surface pattern", "superelevated edge", "residual stress", "warping", "crack", "delamination", "balling", "process signature", "topography", "by-product", "spatter", "off-axis", "in-axis", "co-axial".
2. Search by author and research group: starting from i) previously published reviews, ii) the results of our search by keywords, and iii) the authors' knowledge of the research area, any additional or more recent

papers from individual authors and the research groups they belong to were searched through faculties' web-pages, Google Scholar personal pages, research groups and institutes' websites.

3. Search by references: for each paper selected through the former two methods, a further search was performed by going through all papers cited by the selected ones and identifying the relevant ones.
4. Search by citation: for each paper selected through the three former methods, a further search was performed by going through all citations (using the Google Scholar "cited by" tool) and identifying the relevant ones.
5. Iteration of steps 1 to 4: once new papers and new authors were identified, the list of keywords was refined, more recent papers were searched, and all citations were explored to identify additionally relevant studies.
6. Final screening phase: all papers selected through steps 1 to 5 were read by the authors and screened out based on their relevance to the topics included in this review (e.g., we filtered out studies presenting methods that were not applicable in-situ/in-process, studies not appliable to powder bed fusion processes, etc.).

Final classification phase: all finally selected papers went through a more in-depth analysis, they were classified according to the several classification criteria adopted in our study, including the sensing method, the in-situ monitoring level, the type of detected anomaly, etc.